Hybrid Atomistic-Continuum Formulations and the Moving Contact Line Problem

by

Nicolas Hadjiconstantinou

B.A., Engineering, Cambridge University, U.K. (1993)
S.M., Mechanical Engineering, Massachusetts Institute of Technology (1995)
M.A., Engineering, Cambridge University, U.K. (1997)
S.M., Physics, Massachusetts Institute of Technology (1998)

Submitted to the Department of Mechanical Engineering
in partial fulfillment of the requirements for the degree of

Doctor of Philosophy in Mechanical Engineering

at the

MASSACHUSETTS INSTITUTE OF TECHNOLOGY

September 1998

Author .....
Department of Mechanical Engineering
August 1, 1998

Certified by .....
Anthony T. Patera
Professor
Thesis Supervisor

Accepted by .....
Ain A. Sonin
Chairman, Department Graduate Committee

Hybrid Atomistic-Continuum Formulations and the Moving Contact Line Problem

by

Nicolas Hadjiconstantinou

Submitted to the Department of Mechanical Engineering
on August 1, 1998, in partial fulfillment of the
requirements for the degree of
Doctor of Philosophy in Mechanical Engineering

Abstract

We present a formulation and numerical solution procedure for hybrid atomistic–continuum representations of fluid flows. Hybrid representations are of great importance because they allow the solution of problems that require modelling on the microscale without the associated cost of a fully molecular solution. This is achieved by limiting the molecular treatment to the regions where it is needed while using the inexpensive continuum description in the remainder of the computational domain.

The ingredients are, from the atomistic side, non-equilibrium molecular dynamics, and from the continuum side, spectral/finite element solutions. Molecular dynamics has been chosen for its ability to capture all the underlying physics without the need for modelling assumptions. The continuum solution techniques chosen represent the best compromise between the minimum computational cost, simplicity, and applicability to a wide variety of problems of interest. The matching is provided by a classical procedure, the Schwarz alternating method with overlapping subdomains. This matching technique exhibits favorable convergence properties and has been preferred because of its ability to bypass the problem of matching fluxes in molecular dynamics which has not been satisfactorily treated to date.

Flow of a dense fluid (supercritical Argon) in a complex two-dimensional channel serves as a test problem for the validation of the technique developed above. Reasonable agreement is found between the hybrid solution and the fully continuum solution which is taken to be exact. The hybrid technique is subsequently applied to the moving contact line problem.

The motion of contact lines (the locus of intersection of a two-fluid interface with a bounding solid) has, due to the multitude of length scales involved, been one of the few problems that has defied theoretical analysis over the years. It has long been concluded that continuum hydrodynamics is not adequate for the description of the physics involved in the vicinity of the contact angle, which is predominantly molecular kinetic, thus making this problem a good candidate for our solution technique.

The basic ingredients for the hybrid treatment of the contact line problem are the continuum solution technique, the molecular solution technique, and a modified

Schwarz method required due to the existence of two fluids and a two-fluid interface. The continuum solution is provided by a variationally consistent finite element simulation technique we have developed for the above reason. An already developed molecular simulation technique is adapted to provide the molecular solution. Our hybrid solution is compared with the fully molecular solution which serves as an exact solution for comparison purposes. Good agreement is found between the two solutions.

Thesis Supervisor: Anthony T. Patera
Title: Professor

Acknowledgments

First, I would like to thank my advisor Professor Anthony T. Patera. I was privileged to work with him and benefit from his tremendous experience and insight that provided me with an extremely interesting and rewarding project to work on. His support and expert advice was invaluable and contributed to a learning experience that has been immensely enjoyable.

I would like to extend my gratitude to the other members of my thesis committee, Professors Ain Sonin, and Sidney Yip. Their guidance and assistance is deeply appreciated.

I am grateful to the other members of my research group, Marius Paraschiviou, Miltos Kambourides, Jeremy Teichman, Serhat Yesilyurt, John Otto, and Luc Machiels. They have provided me with technical advice, intellectual stimuli but also invaluable friendship.

I would also like to thank all the students of the Fluid Mechanics Laboratory for providing an ideal working environment. Their friendship and help will always be remembered.

My friends at MIT have made these five years not only possible but also enjoyable. I will always cherish their love, understanding, and encouragement. Special thanks to my "family in Boston" Dr. Wolf Bauer, Antonis Eleftheriou, Maria Kartalou, Karolos Livadas, Panayiota Pyla, Andreas Savvides, and Chris Hadjicostis.

Special thanks to my parents Athena and George, and my sister Stavroulla for their love and encourangement.

This work was supported by DARPA and the ONR under Grant N00014-91-J-1889. We are indebted to Dr. Keith Refson for the development of the molecular dynamics simulation code MOLDY. We thank Nektonics, Inc., for providing and supporting the simulation code NEKTON.

Στους γονείς μου

Αθηνά και Γιώργο,

και στην αδελφή μου

Σταυρούλλα

Contents

List of Figures

List of Tables

Chapter 1

Introduction

Many important problems in materials processing involve a range of scales from the atomistic to the continuum. Purely atomistic representations are clearly computationally intractable because of the number of particles required to represent macroscale phenomena [26]; conversely, purely continuum approaches often neglect certain critical microscale phenomena that do not now, and many never, admit adequate macroscale constitutive characterization. New integrative frameworks are therefore required, not only of the well–established atomistic *then* continuum variety, but also of the atomistic *with* continuum variety.

Our interest is in the latter, in particular, in gas–*liquid*–solid systems subject to the full range of mechanical, thermal, and, ultimately, chemical interactions. Such a framework will allow us to treat a variety of problems of practical importance. The need for a better understanding of wall fluid interactions, two-phase flow, contact line motion, and material behavior under highly non-equilibrium situations, are a few of the envisioned applications of a hybrid solution framework, driven primarily by today's rapidly expanding needs for materials processing techniques.

The isothermal moving contact line problem, which is fully described in a following section, will be used as an example problem in this thesis. This problem lends itself nicely to the new integrative framework presented here, because its satisfactory solution requires molecular input that is localized to small (and hence tractable by molecular techniques) regions, namely the vicinity of the contact point.

1.1 Previous Work

Hybrid atomistic–continuum representations have been developed for problems in both solid mechanics and fluid mechanics. In fluid mechanics, several domain decomposition approaches have been proposed and implemented [13]. Most methods developed to date are, however, restricted to gas flows, in that both the particle treatment (e.g., Direct Simulation Monte Carlo techniques, discretizations of the Boltzmann equation) and the interface treatment (e.g., variations of the Marshak condition) are directly applicable only to dilute systems [7, 44, 16]. Although these concepts can perhaps be extended to dense fluids, we have chosen a slightly different strategy that does not require explicit calculation of fluxes. Our approach is, in fact, more closely related to hybrid representations of solid mechanics problems [25, 21], such as the study by Kohlhoff et al. [25], and to a recently published fluid mechanical study by O'Connell and Thompson [31].

In the work of O'Connell and Thompson [31] the matching between the atomistic and continuum region is achieved through the introduction of an "Eulerian" overlap region in which both descriptions are presumed valid. The idea of an overlap region is also employed in the work of Kohlhoff et al. [25] albeit in a "Lagrangian" formulation which was favored by the nature of the solid mechanics problems treated by their approach. In fact, the "Lagrangian" identification of the lattice sites with finite element nodes simplifies the matching problem considerably, but can only be achieved for problems which do not exhibit bulk material motion such as solid mechanics problems.

The matching technique used in our own work is known as the Schwarz alternating method [28] and it, again, introduces a overlap region through which information exchange between the two (or more) subdomains takes place. The technique requires a number ($O(10)$) of iterations until the solutions from all domains agree in the overlap region. The solution agreement in the overlap region ensures that fluxes are also matched even though they are not explicitly prescribed. The imposition of fluxes has been one of the main obstacles in obtaining hybrid atomistic-continuum repre-

sentations because of their non-local nature. The Schwarz technique still requires the imposition of boundary conditions on molecular dynamics simulations but those are now Dirichlet instead of Neumann. The imposition of Dirichlet boundary conditions in a molecular dynamics simulation is treated in chapter 4. Our technique successfully decouples the molecular and continuum time-scales and can also treat problems in more than one space dimension. The above attributes are particularly important because they represent the limitations of the technique by O'Connell and Thompson. In particular, the O'Connell technique was excessively slow because the matching was done in a timestep-by-timestep basis, and hence, the continuum subdomain was integrated at the molecular timestep. This is further discussed in chapter 3.

The applicability of the technique presented in this thesis is limited to problems in which the molecular information, or the region which needs to be treated by molecular methods, is very small and localized. This does not reflect a limitation in the coupling procedure used, but rather an inherent characteristic of molecular dynamics, namely that very small regions can be treated even with appreciably powerful computers. Problems that do not fulfill the above requirements require the development of alternative molecular techniques that are more computationally efficient. The key to this problem lies in the realization that between the molecular and continuum levels lie a big number of intermediate descriptions that correspond to varying degrees of coarse graining of the molecular description as we move towards the continuum one. As we move away from the molecular level, information is lost but the computational cost per unit of simulated volume decreases. Stochastic molecular dynamics [3] and Lattice Boltzmann gases [11] are two promising techniques (in increasing order of coarse graining) that provide interesting compromises between significant speedups at the expense of molecular details at the molecular level: if the molecular level of detail is not necessary but rather the aggregate molecular behavior is the reason for using molecular techniques, the above methods can increase the size of the molecular region by a significant amount for the same computational cost. Although we explicitly deal with the use of molecular dynamics, the adoption of one of the above techniques does not require any major modifications to the framework developed in this thesis.

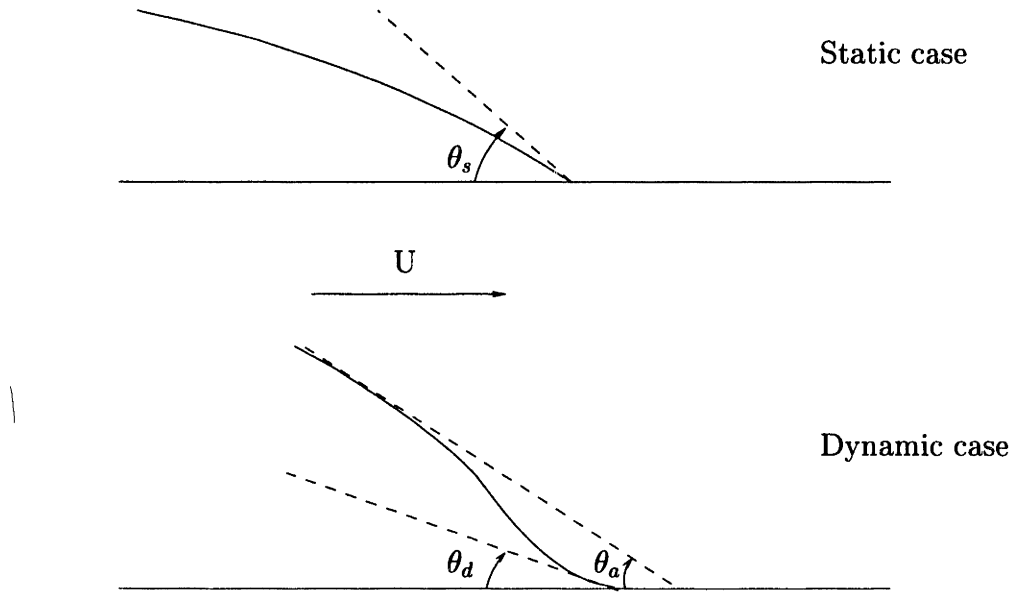

Figure 1-1: Static (θ_s), dynamic (θ_d), and apparent (θ_a) contact angles at the tip of a stationary droplet (Static case), and a spreading droplet (Dynamic case).

1.2 The Contact Line Problem

The motion of contact lines (locus of points where the interface between two immiscible fluids meets a bounding solid in Fig. 1-1) has been one of the few problems that has defied theoretical analysis over the years. Contact lines are present and important in various situations such as coating flows, or processes where one fluid is used to displace another, such as water displacing oil from a pipe.

The static properties of contact lines are fairly well known; it is widely accepted that the static contact angle, θ_s, (the angle between the two-fluid interface and the solid at their intersection point), is given by Young's equation [40] which is a microscopic force balance equation at the point where the three materials meet. In the dynamic case, however, matters become more complicated: the contact line moves

with an unknown velocity and the contact angle assumes, in general, a different value (θ_d). Young's equation is no longer valid, since the contact line is not in equilibrium. The dynamic contact angle is expected to be different than the static value, and will be expected to be a function of the capillary number, $Ca = \mu U/\gamma$, which is a measure of the relative strength of the capillary and shear forces [40]. Here, μ is the viscosity of one of the two fluids, U is a characteristic velocity, and γ is the surface tension coefficient of the two fluids. The capillary number is also expected to govern the shape of the two fluid interface close to the contact line since the latter deflects so as to balance capillary and shear stresses.

One of the reasons that no satisfactory theory exists for the above problem is that the experimental data, usually responsible for guiding theoreticians, are unable to aid in the development of the theory; in fact interpreting the experimental data is a major challenge in itself. Experimental probing techniques (usually visual) are limited by resolution to the micrometer scale [41]. The governing phenomena in this problem, however, are of the order of and confined to within nanometers from the contact line. Hence, experimental results for the contact angle report in reality an apparent contact angle (θ_a)–a coarse grained (with respect to the desired resolution) measurement of the angle the tangent to the two-fluid interface appears to make with the solid at the micrometer scale. This apparent angle can, in general, be very different from the true dynamic contact angle because of the large curvature of the two-fluid interface due to the diverging viscous and capillary forces in the region close to the contact line which is inaccessible to observation.

Despite these problems, experimental data have accumulated over the years and have led to a better understanding of the problem [6]. Some empirical correlations [6] have also been obtained from the data, the simplest of which is Hoffman's law [20] which is fairly widely used. As noted before, a theoretical justification of such correlations has proven almost impossible, since the variables involved (such as apparent contact angle) are not directly related to the variables in which the governing dynamical equations are expressed, but rather form coarse grained mixtures of the latter. Progress has been made recently [38] but further work is required.

From the theoretical side, it has long been recognized [43] that usual hydrodynamics cannot be used to analyze the problem. The usual no slip boundary condition at the contact line leads to divergences in the energy dissipation rate and the shear stress at that point. We would physically expect that the singularities do not really exist but are a result of the mathematical model used which, obviously, needs to be modified. Both analytical [8] and numerical [29] results exist in which the stress singularities are relieved by ad hoc methods, such as slip models. Analytical approaches are usually based on the method of matched asymptotic expansions, and utilize the fact that the far field solution is very insensitive to the exact details of the inner region solution. This has also been demonstrated in numerical approaches [5], where agreement with experimental results can be obtained with a variety of slip models with adjustable slip constants or other singularity relieving methods. This is encouraging from a results oriented point of view but not so encouraging from the theoretical point of view, since comparison with experiments cannot give feedback for the development of a "universal" theory that not only matches experiments but is also capable of prediction.

1.3 Thesis Overview

The proposed thesis primarily focuses on numerical methods. Recent studies [27] which demonstrated that molecular dynamics (MD) can be used to study nanoscale fluid mechanical phenomena have prompted us to choose MD as one of our main tools. The objective of this work is to contribute to the better understanding and solution of problems such as the moving contact line problem by: 1) methodologies that allow the use of MD to develop more physically correct models for use in numerical simulations, and 2) the development a hybrid solution framework for completely treating such problems, i.e. numerical solutions that incorporate both continuum and molecular subdomains with the molecular domain (by far the most computationally expensive) limited to the regions that require molecular input.

In chapter 2 a basic introduction to molecular dynamics and the numerical tech-

niques required for simulation of materials at the atomistic level is given. In the following chapter the other major ingredient required for a general hybrid description is presented, namely the Schwarz alternating method. A direct consequence of the use of the Schwarz alternating method is the need to impose arbitrary velocity and temperature boundary conditions on molecular dynamics simulations. This is addressed in chapter 4 where a simple problem, flow in an obstructed microchannel at low Reynolds number, is formulated to serve as a validation test for the boundary condition imposition technique developed in chapter 4. The test problem is revisited in chapter 5 where a hybrid solution of the flow in the obstructed channel is sought as a validation of the hybrid technique developed in chapters 3 and 4.

In chapter 6 the moving contact line problem is discussed and a variationally consistent finite element technique is developed for the fully continuum treatment of a simplified contact line problem treated in this thesis: the flow of two immiscible fluids in a two-dimensional channel. This finite element technique will also be used to treat the continuum part of our hybrid solution to the contact line problem that is presented in chapter 8. In chapter 7 we present fully molecular and fully continuum solutions of the contact line test problem. We show that the fully molecular results can be approximated to a good level by fully continuum techniques that use molecular input in the form of boundary conditions. This molecular input comes from the fully molecular solutions of the same problem; we describe these simulations as of the molecular *then* continuum variety.

Chapter 2

Molecular Dynamics

Despite the molecular nature of matter, for most hydrodynamic applications of interest, the continuum description of nature successfully captures all the essential physics while resulting in a significantly more tractable formulation. There exist, however, situations where the continuum description is inadequate; such situations are described in the following chapters. In this case we need to resort to the molecular description and use the classical tools of statistical mechanics. Unfortunately statistical mechanics has traditionally been limited by the intractability and complexity of the governing equations describing the systems of interest. For fluids, the BBGKY hierarchy of equations [17] has been tackled for very few special cases, dilute gases being the most notable. The advent of fast and powerful computers has brought a revolution to the molecular modeling of nature; numerical solutions of the BBGKY equations can be obtained for more complicated cases, but more importantly, systems can be *animated* at the molecular level through molecular dynamics (MD).

In the molecular dynamics presented in this thesis, systems are modeled as collections of molecules that obey a set of equations of motion (classical Newtonian) and interact between themselves through intermolecular interaction potentials. MD is a very powerful technique because, as long as the interaction potentials are specified for the systems under investigation, no approximations or further modeling is required; all the exact physics is present and accounted for. The major disadvantage is the high computational cost associated with these computations which limits the use of

this technique to very small systems and very short time-scales (of the order of 10000 molecules and $1ns$ in time for a high-end workstation).

2.1 Preliminaries

Although in the most general formulation of statistical mechanics particles interact through quantum mechanical equations of motion, it is often the case that many systems can be simulated to sufficient approximation level via the use of the classical Newtonian equations of motion

$$\ddot{\vec{r}}_i = -\frac{1}{m_i}\sum_{j\neq i}\frac{1}{r_{ij}}\frac{dV(\vec{r}_{ij})}{dr_{ij}}\vec{r}_{ij}, \tag{2.1}$$

where m_i is the mass of the particle, $\vec{r}_i$ is the position vector of the particle with respect to the coordinate origin, $\vec{r}_{ij} = \vec{r}_i - \vec{r}_j$, $V(\vec{r}_{ij})$ is the potential energy of particle i due to particle j, and the sum is implied to be over all particles (N). This simplification, which results in significantly less computationally intensive calculations compared to quantum mechanical calculations, will in general be valid when all quantum mechanical effects (both temporal and spatial) are negligible, or can be reliably lumped in an effective interaction potential $V(\vec{r}_{ij})$ and the effects of zero point motion can be ignored. This is always the case for the hydrodynamic applications presented in this thesis, and as a result we will limit ourselves to the exclusive use of the classical equations of motion.

The interaction potential used in this study is the well known [4] Lennard-Jones potential

$$V(\vec{r}_{ij}) = 4\varepsilon[(\sigma/r_{ij})^{12} - (\sigma/r_{ij})^6]. \tag{2.2}$$

This simple model was chosen for its ability to minimize the computational cost of calculations while retaining all the essential physics under investigation. The Lennard-Jones potential has been shown [4] to accurately reproduce the properties of noble gases with appropriate choice of the two parameters ε and σ. The Lennard-Jones potential can also be used in studies of water [14] (in conjunction with an electrostatic

potential), and light hydrocarbons. It provides a reasonable compromise between numerical efficiency and accuracy for hydrodynamic applications where a "hard sphere" approximation often suffices. Structural or thermodynamic properties of materials other than noble gases are not reproduced accurately. The great computational efficiency enjoyed form the use of this potential is a result of two effects: first, the potential has a short range and effectively decays to zero for $r > 10\sigma$ thus leading naturally to the definition of an interaction sphere that contains all the particles contributing to the force acting on a specific particle, and second, it is a pairwise additive potential and hence the force acting on a simulated particle can be simply calculated by adding the forces exerted to it by the other particles that are within its interaction sphere. Because the number of molecules within a sphere of radius r increases as $n \propto r^3$, researchers have attempted to use interaction spheres (defined by the interaction cut-off r_c) smaller than 10σ. It has been shown [41] that the error resulting form the use of cut-offs as small as 2.2σ is negligible. Throughout this study we have used a conservative value of $r_c = 3\sigma$.

The equations of motion are numerically integrated using Beeman's modified equations of motion [35], which is a fourth order accurate in space and third order accurate in time predictor corrector method. It is included here for completeness: if x is any dynamic variable (in our case $\vec{r}_{ij}$), $\dot{x}^{(p)}, \dot{x}^{(c)}$ the predicted and corrected corresponding velocities, and Δt is the numerical integration timestep, the scheme is as follows:

1. $x(t+\Delta t) = x(t) + \Delta t \dot{x}(t) + \frac{\Delta t^2}{6}[4\ddot{x}(t) - \ddot{x}(t-\Delta t)]$
2. $\dot{x}^{(p)}(t+\Delta t) = \dot{x} + \frac{\Delta t}{2}[3\ddot{x}(t) - \ddot{x}(t-\Delta t)]$
3. $\ddot{x}(t+\Delta t) = F(x_i(t+\Delta t), \dot{x}_i^{(p)}(t+\Delta t), i = 1...N)/m$
4. $\dot{x}^{(c)}(t+\Delta t) = \dot{x} + \frac{\Delta t}{6}[2\ddot{x}(t+\Delta t) + 5\ddot{x}(t) - \ddot{x}(t-\Delta t)]$
5. Replace $\dot{x}^{(p)}$ with $\dot{x}^{(c)}$ and goto 3. Iterate to convergence.

Here F is the total force acting on a particle and N is the total number of particles in the simulation. The simulations were performed using modified (by the author) versions of the third-party molecular dynamics simulation code MOLDY.

The simulation procedure described above produces realizations of the micro-canonical ensemble, which in many cases are not good approximations to the system under investigation. In particular, it is sometimes useful to let the volume of the system vary and constrain the pressure of the system at an imposed pressure P thus realizing a constant pressure ensemble. In what follows we review the reformulation of the equations of motion pioneered by Parinello and Rahman [32] which allows the simulation of a system under constant pressure situations.

2.2 Constant Pressure Simulations

In the formulation of Parinello and Rahman [32, 35] the molecular dynamics simulation cell is allowed to change in size in response to the imbalance between the imposed pressure and the internal simulation pressure. The new equations of motion are written in the center of mass co-ordinates ($\vec{s}_i$)

$$m_i \ddot{\vec{s}}_i = \mathbf{h}^{-1} \nabla \sum_{j \neq i} V(\vec{r}_{ij}) - m_i \mathbf{G}^{-1} \dot{\mathbf{G}} \dot{\vec{s}}_i. \tag{2.3}$$

Here $\vec{s}_i = \mathbf{h}^{-1} \vec{r}_i$, $\mathbf{h}$ is the 3×3 matrix whose columns are the molecular dynamics cell vectors, and $\mathbf{G} = \mathbf{h}^T \mathbf{h}$. Additionally the cell vectors obey the following dynamical equation

$$W \ddot{\mathbf{h}} = (\mathbf{\Pi} - \mathbf{p}) \mathbf{k} \tag{2.4}$$

where W is the fictitious mass parameter of the pressure reservoir in equilibrium with the system, $\mathbf{k} = V \mathbf{h}^{T^{-1}}$, V is the volume of the system, $\mathbf{p}$ is the external stress (tensor) applied to the system, and $\mathbf{\Pi}$ is the molecular contribution to the stress tensor defined by

$$\mathbf{\Pi} = \frac{1}{V} \left(\sum_i^N m_i \dot{\vec{r}}_i \dot{\vec{r}}_i - \sum_i^N \sum_{j>i}^N \frac{1}{r_{ij}} \frac{dV(\vec{r}_{ij})}{dr_{ij}} \vec{r}_{ij} \vec{r}_{ij} \right). \tag{2.5}$$

Note that the above definition (eq. (2.5)) assumes that the system has a uniform pressure throughout and hence it is in pressure equilibrium. The definition and evaluation

of thermodynamic properties as a function of space in non-equilibrium situations is obtained via the use of the assumption of local thermodynamic equilibrium discussed in section 2.4.

2.3 Simulation Reduced Units

It is also customary to define reduced units based on the molecular model of the material simulated [4]. In both series of simulations reported in this work the principal material used was fluid Argon and hence unless otherwise stated, all quantities will be expressed in reduced units using $\sigma = 3.4$ Å for length, $m = 40$ amu for mass, $\varepsilon/k_b = 119.8^o K$ for temperature, and $\tau = (m\sigma^2/48\varepsilon)^{1/2} = 3.112 \times 10^{-13} s$ for time. Here σ and ε are the parameters of the Lennard-Jones (LJ) potential for Argon [4], m is the mass of the Argon atom, and τ is the characteristic time for Argon. The integration timestep was $\Delta t = 0.032\tau$.

2.4 Definition of Macroscopic Properties

From a statistical mechanical point of view molecular dynamics numerically simulates the motion of the system under consideration in a $6N-$dimensional phase space [4]. As a result, MD simulation results are in the form of position coordinates and velocities of the N system molecules for a large number of timesteps (duration of the simulation). In order to convert those to the usual macroscopic thermo-hydrodynamic parameters we need to establish a "macroscopic connection". In statistical mechanics this is done through the use of ensembles: observables (parameters that are macroscopically perceived, such as energy, temperature, pressure, and density) are defined as functions of the molecular phase space variables and evaluated at every timestep. Due to the huge number of degrees of freedom of the molecular system, it is conceivable that a huge number of molecular configurations will lead to the same values of observables leading to what is usually called "loss of information". On the other hand these macroscopic observables will fluctuate as the particles continuously change

positions and momenta. The "macroscopic connection" is made through the use of an ensemble of identical systems such that the macroscopic quantity or parameter is defined as the average of the observable over all the ensemble members [4]. In the following section we describe the extension of the equilibrium ideas to the local thermodynamic equilibrium formulation that allows the treatment of non-equilibrium situations.

2.4.1 Local Thermodynamic Equilibrium

The concept of local thermodynamic equilibrium allows the extension of thermodynamic equilibrium techniques to spatially non-equilibrium systems. It is the equivalent of the quasistatic assumption for time-varying systems, and essentially assumes that although the system is not in equilibrium it can, to a good approximation level, be assumed to be in equilibrium locally in space (versus time for the quasistatic case). This assumption can be reasonable if the gradients in the system are sufficiently small. In particular, we require that the change across a region (spatial case) or in time (temporal case), due to the non-equilibrium gradients present, be smaller than the statistical fluctuations in this region because of its small size. This essentially implies that the larger the gradients, and hence the larger the deviation from equilibrium, the smaller these regions need to be. Trozzi et al. [42] have verified that this concept can be used to define *local* macroscopic properties in MD simulations. For the gradients present in their work, they found that regions of characteristic size σ can, to a good approximation level, be assumed to be in local thermodynamic equilibrium. We will be using the same criterion since the gradients present in our work are very similar to the work of Trozzi et al.

In fact, we can show that in order to simulate the smallest gradients possible (in an attempt to make the simulation as realistic as possible) we need to increase the number of molecules by adding the extra molecules in the direction of the gradient. The fluctuations $\Delta\chi_F$ of a property χ in a region of space Ω containing N molecules scale as $\Delta\chi_F \propto 1/\sqrt{N}$. The variation of the same property $\Delta\chi_g$ along the direction of the gradient g is given by $\Delta\chi_g = gL$ where L is the linear dimension of Ω in the

direction of g. We require that $\Delta\chi_g \sim \Delta\chi_F$ and hence,

$$gN^d \propto N^{-1/2}. \tag{2.6}$$

We have substituted L with N^d where d takes different values depending on the "mode" of addition of molecules. If molecules are added equally in all dimensions $d = 1/3$; if the molecules are added in the direction of the gradient g, $d = 1$; finally, if the molecules is added in the remaining directions only, $d = 0$. It follows that the optimum scaling (least number of molecules for a given gradient) obtains for the case of molecule addition in the direction of the gradient for which

$$N \propto g^{-2/3}. \tag{2.7}$$

As an example, consider the case of a fluid in a two-dimensional channel with the two bounding walls at different temperatures. For a given number of molecules and fixed wall temperatures (or temperature difference), the minimum gradient that can be simulated is obtained by maximizing the number of molecules in the transverse channel direction, the direction normal to the two walls.

We would like to note that the smaller the local equilibrium regions the smaller the number of particles that reside in it. Hence, although in theory an arbitrarily small region can always be found that can be assumed to be in local equilibrium, this is not practical for regions much smaller than the ones used in this study for the following reason; the statistics obtained from these very small domains will be unreliable due to the small number of molecules present in them, since as discussed above the directions transverse to the gradient do not typically contain an appreciable number of molecules. Additionally, regions smaller than the characteristic size σ are not admissible on physical grounds since this length scale sets the lower limit for the spatial region over which the concept of a fluid exists.

2.4.2 Statistical Mechanical Properties

In this section we present the definitions of macroscopic observables such as temperature and pressure in terms of the individual molecule microscopic phase space variables. These definitions are the first step in the macroscopic connection required to recover a spatially varying thermo-hydrodynamic field over the MD simulation domain from the molecular data. The above definitions can be obtained through statistical mechanical analysis [23]; in particular the macroscopic conservation laws are obtained through an ensemble averaging of the corresponding microscopic conservation laws. The identification of single particle contributions to the macroscopic observables follows from the direct comparison of the microscopic ensemble averaged equation and its continuum counterpart. For the derivation of these relations the reader is referred to the original work of Kirkwood and Buff [23].

Let V be the volume in which we want to define the macroscopic observable A_V. Following [39, 42] we define

$$A_V = \frac{1}{V}\int_V d\vec{r}\sum_{i=1}^{N} A_i \delta(\vec{r} - \vec{r}_i) \tag{2.8}$$

where N is the number of molecules, and $A_i = A_i(\{\vec{r}_j, \vec{p}_j\}_{j=1,N})$ is the individual particle (i) contribution to the macroscopic property A_V. Again following [42], we define for the density (ρ_V)

$$A_i = 1, \tag{2.9}$$

for the temperature (T_V)

$$A_i = \frac{m_i \dot{r}_i^2}{3k_B \rho_V} \tag{2.10}$$

where k_B is Boltzmann's constant, for the internal energy (E_V)

$$A_i = \frac{\sum_{j \neq i} V(\vec{r}_{ij})}{2\rho_V}, \tag{2.11}$$

for the flow velocity ($\vec{v}_V$)

$$A_i = \dot{\vec{r}}_i, \tag{2.12}$$

and for the stress tensor (Π_V)

$$A_i = m_i(\dot{\vec{r}}_i - \vec{v}_V)(\dot{\vec{r}}_i - \vec{v}_V) - \frac{1}{2}\sum_{j \neq i} \vec{r}_{ij} \frac{1}{r_{ij}} \frac{dV(\vec{r}_{ij})}{dr_{ij}} \vec{r}_{ij}, \tag{2.13}$$

from which the pressure can be evaluated as the trace $P_V = \frac{1}{3}Tr(\Pi_V)$. Using the definitions given in the previous section, macroscopic observables can be evaluated over small regions at one instant in time for every member of the ensemble under consideration. Any thermodynamic parameter is then obtained from the ensemble average of this observable over all the members of the ensemble.

2.4.3 Error Estimation

Due to the small number of particles that are available in each local equilibrium domain (bin) the statistical uncertainty associated with the property estimates is large. Under the assumption of Gaussian statistics the statistical error scales inversely proportional to the square root of the number of samples taken. In our macroscopic world, local equilibrium regions contain more than 10^{20} molecules and as a result the fluctuations within them are imperceptible. In molecular simulations, however, the size of a local thermodynamic equilibrium region, dictated by the the balance of the fluctuations and the magnitude of the gradients in the simulation (eq. (2.6)), is of the order of a few σ. The fluctuations in the value of a quantity ($\delta\chi_F$) in such a domain are often of the order of the value of the quantity itself (χ), and hence the gradients that can actually be resolved involve variations of $O(\chi)$ over distances of a few σ. Large gradients, however, require smaller local equilibrium regions which contain less molecules and, hence, exhibit larger fluctuations. Simulation accuracy and resolution of physically realistic gradients are thus coupled.

Steady simulations, or simulations that are unsteady on a macroscopic time-scale which is long enough such that the problem appears to be steady at the microscale, benefit in terms of accuracy from the use of the ergodic theorem [4] that allows the exchange of time with ensemble realizations. More precisely, an ergodic system in a steady state left to evolve in time, produces realizations that are equivalent to

those obtained by different members of the ensemble used in the formal definition of a statistical mechanical system. Hence the ensemble averaging procedure is replaced by averaging in time which is very convenient for a molecular dynamics simulation which is inherently an integration procedure in time. The system under investigation is thus simulated for an equilibration time that allows for initial condition effects to decay and hydrodynamic transient effects to disappear, and its subsequent configurations are sampled in regular time intervals (of the order of a few integration timesteps).

The expected error in the estimation of a thermodynamic parameter depends on the number of independent samples taken. We could maximize the number of samples taken by sampling every integration timestep. Unfortunately, as discussed above, for reasons of numerical accuracy the integration timestep is a very small fraction (0.032) of the characteristic time-scale for the fluid (τ), and hence samples that are temporally less than τ apart are statistically correlated: even if they are used in the sampling procedure they do not contribute any new information and do not reduce the statistical error. Based on physical grounds, we would expect that an appropriate decorrelation time-scale would be τ. Numerical experiments that will be described later, show that different observables have different decorrelation time-scales, but this physical reasoning is approximately correct. In particular, velocity which is a first moment of molecular velocities, requires $2\tau - 3\tau$, whereas heat flux which is a higher moment but also involves the interatomic forces requires less than τ.

2.4.4 Statistical Inefficiency

In this section we introduce the statistical inefficiency s which can be viewed as the number of samples that have to be discarded in a series of data such that each new data point contributes independent information. It is formally defined [4] as the limiting ratio of the observed variance of the sample average ($\langle \mathcal{A} \rangle_b$) of observable $\mathcal{A}$ over subblocks of length τ_b, to the expected variance under the assumption of

Gaussian uncorrelated statistics ($\sigma^2(\mathcal{A})$):

$$s = lim_{\tau_b \to \infty} \frac{\tau_b \sigma^2(\langle \mathcal{A} \rangle_b)}{\sigma^2(\mathcal{A})}. \tag{2.14}$$

In other words, by dividing our series of data (of length τ_t) into n_b small blocks of length τ_b, such that $\tau_t = \tau_b n_b$, we can calculate the mean of the simulation

$$\langle \mathcal{A} \rangle = \frac{1}{\tau_t} \sum_{t=1}^{\tau_t} \mathcal{A}(t) \tag{2.15}$$

and also the mean of every block b

$$\langle \mathcal{A} \rangle_b = \frac{1}{\tau_b} \sum_{t=1}^{\tau_b} \mathcal{A}(t). \tag{2.16}$$

We can calculate the variance of this mean

$$\sigma^2(\langle \mathcal{A} \rangle_b) = \frac{1}{n_b} \sum_{n=1}^{n_b} (\langle \mathcal{A} \rangle_b - \langle \mathcal{A} \rangle)^2 \tag{2.17}$$

which, if the blocks are large enough to be uncorrelated, is required by the central limit theorem follow

$$\sigma^2(\langle \mathcal{A} \rangle_b) = \frac{\sigma^2(\mathcal{A})}{\tau_b}, \tag{2.18}$$

where

$$\sigma^2(\mathcal{A}) = \frac{1}{\tau_t} \sum_{t=1}^{\tau_t} (\mathcal{A} - \langle \mathcal{A} \rangle)^2. \tag{2.19}$$

Thus, if the the data are statistically independent, we expect that

$$lim_{\tau_b \to \infty} \frac{\tau_b \sigma^2(\langle \mathcal{A} \rangle_b)}{\sigma^2(\mathcal{A})} = 1, \tag{2.20}$$

whereas, if there is some correlation persistence

$$lim_{\tau_b \to \infty} \frac{\tau_b \sigma^2(\langle \mathcal{A} \rangle_b)}{\sigma^2(\mathcal{A})} = s, \tag{2.21}$$

which allows us to estimate the reduction in effective sample points available.

We can thus estimate the expected error associated with the finite number of samples as

$$\sigma^2(\langle \mathcal{A} \rangle_{b=t}) = \frac{\sigma^2(\mathcal{A})}{t/s} \equiv \frac{A^2}{N}, \tag{2.22}$$

where we have lumped the population variance and the statistical inefficiency in the constant A which depends on the statistic, and shown the explicit form of the dependence on the number of samples taken N. This form will be very useful in the following chapter; the calculation of statistical inefficiencies will be illustrated in chapter 4.

Chapter 3

Coupling Approach

In this section we introduce the other major ingredient of the hybrid atomistic continuum simulation technique presented in this thesis. Although mathematical solutions (numerical/analytical) of various problems often consist of matched solutions in more than one subdomain, the particular problem of coupling a continuum solution to a molecular solution is particularly challenging. The major obstacle lies in the requirement of exchange of information between the various subdomains treated by what appear to be dissimilar descriptions. Fully continuum coupling methods (where all subdomains are described by continuum models) have been particularly successful due to the simplicity and large extent of understanding of the treatment of boundary conditions in continuum formulations through which the various subdomains interact.

In molecular dynamics, however, the imposition of macroscopic thermo-hydrodynamic boundary conditions is far from trivial. The integration of the equation of motion of the molecules requires boundary conditions at the atomistic level. As explained in section 1.3, a huge loss of information takes place when connecting to the macroscopic level, at which individual molecule state properties enter as statistics. Thermo-hydrodynamic parameters can be viewed as moments of the molecular phase space distribution [17]; this distribution can be viewed as the number of ensemble members found in an infinitesimal region of phase space divided by the total number of members, or by using the ergodic theorem, as the probability that the simulated system will reside in that volume of phase space at the given instant in time. Therefore

there is an infinite number of realizations of molecular state properties that can lead to the same value of a given observable. There is, of course, only one physically correct distribution function which is, however, unknown. This is the reason we initially set out to solve the problem numerically!

Despite the difficulties just cited, some attempts using approximate distribution functions, or other methods that artificially constrain the molecular distribution function such that their moments exhibit the required behavior [15, 31], have been reasonably effective. These methods will be discussed in chapter 4. Dense fluid hybrid techniques have concentrated on the imposition of Dirichlet boundary conditions which in terms of a molecular simulation require only single particle distribution functions. Neumann, or equivalently flux, boundary conditions, such as stress and heat flux are non-local: the stress or heat flux contribution of a molecule depends on the location of the other molecules in its immediate vicinity. Subsequently prescribing a non-local quantity for N interacting molecules requires not N but $N!$ "executive (ad hoc) decisions".

3.1 Previous Work

In the formulation proposed by Kohlhoff et al., the physical domain is decomposed into two overlapping regions, or equivalently, three regions: an atomistic domain treated by molecular dynamics (MD), a continuum domain treated by finite elements, and an atomistic–continuum overlap region. Displacement boundary conditions in the overlap region provide globally consistent stress fields — presuming that the atomistic description is consistent with the continuum constitutive model of the finite element analysis. For this effectively zero–temperature structural problem, in which the atoms are bound to lattice sites, displacements can be matched on an individual atom–to–finite element node basis; in contrast, for fluid systems, or fluid–solid systems, thermal considerations and material motion preclude such a Lagrangian identification, and an appropriate Eulerian generalization is required.

The recent work of O'Connell and Thompson [31] addresses the problem of mate-

rial motion by introducing an "Eulerian" overlap region. An important conclusion of [31] is that stress continuity can be achieved *without* explicitly matching (or imposing) fluxes. Our method also exploits this result, and also employs an overlap region; however, there are several important differences between the two approaches. The technique of O'Connell and Thompson, as demonstrated in [31], is one–dimensional. Many new issues arise in higher space dimensions, in particular when there is mean (continuum) flow across the atomistic–continuum boundary; we treat these issues by the introduction of a particle reservoir.

Most importantly, as reported in [31], the algorithm of O'Connell and Thompson matches the atomistic and continuum representations on a timestep-by-timestep basis, with the timestep imposed by the molecular dynamics representation. This necessitates many continuum evaluations that, in higher dimensions, and in particular for flows that evolve over continuum time-scales, will result in prohibitive computational costs. In some sense, the O'Connell and Thompson technique decouples length-scales, but not time-scales; our approach does decouple time-scales, requiring only $O(1)$ (in practice, $O(10)$) continuum solutions in order to achieve a steady state. At present our technique is only appropriate for steady problems, although we believe unsteady problems evolving over continuum time-scales can also be treated.

Finally, we remark that, although the O'Connell and Thompson technique permits analysis of detailed atomistic–scale temporal evolution, adequate statistics require averages over sufficiently long time-scales, and thus accuracy and resolution are coupled. Specifically, the results of [31] suggest that only time-scales which correspond to quasi-static evolution on the atomistic scale can be accurately resolved. This is consistent with linear response theory [12], according to which a system "makes use" of fluctuations about a quasi-equilibrium state to alter this state in response to a forcing input.

3.2 Schwarz Coupling Approach

The matching method is described here for the case of a one-dimensional problem; extension to higher dimensions directly follows. Given a problem to be solved by continuum techniques for $0 < x < b$ and molecular techniques for $b < x < L$, we define the continuum subdomain as $0 < x < b$ and the molecular subdomain as $a < x < L$, where $a < b$; $a \leq x \leq b$ is the overlap region where both models are presumed valid. Given boundary conditions at $x = 0$ and $x = L$, a solution is first assumed in one of the subdomains, (say) the molecular. This solution at $x = b$ ($\in [a, L]$) serves as a boundary condition on the continuum subdomain, permitting calculation of the "first continuum iterate." This first continuum iterate, in turn, provides a boundary condition at $x = a$ for the molecular dynamics (MD) simulation. Finally, the resulting "first MD iterate" yields a new boundary condition at $x = b$ for the continuum subdomain. This alternating procedure is then repeated until convergence.

Figs. 3-1 to 3-3 demonstrate the application of the Schwarz method to a very simple problem: Poiseuille flow in a two dimensional channel with zero velocity at both walls ($x = 0, L$). The iteration starts with the assumption of a guess solution in one of the two subdomains, say zero velocity in the molecular region (domain 2). Fig. 3-1 shows the first continuum iterate based on the boundary condition of zero velocity at the wall ($x = 0$) and the boundary condition imposed by domain 2 at $x = b$. The molecular iterate, that completes the first iteration cycle, is shown in Fig. 3-2; it is a molecular solution based on the zero velocity boundary condition at $x = L$ and the boundary condition imposed by domain 1 at $x = a$. The next iteration cycle (Fig. 3-3) proceeds with a continuum iterate based on the updated now boundary condition at $x = b$ and the "external" boundary condition at $x = 0$. The iteration proceeds until the solutions in the two domains are the same and hence no "driving force" exists for a change since the solution will be continuous at the two "internal boundary condition points" $x = a, b$. For purely continuum simulations (both subdomains being continuum) the error exhibits a power law decay, which is further discussed in the convergence section. For mixed atomistic-continuum descriptions the statistical

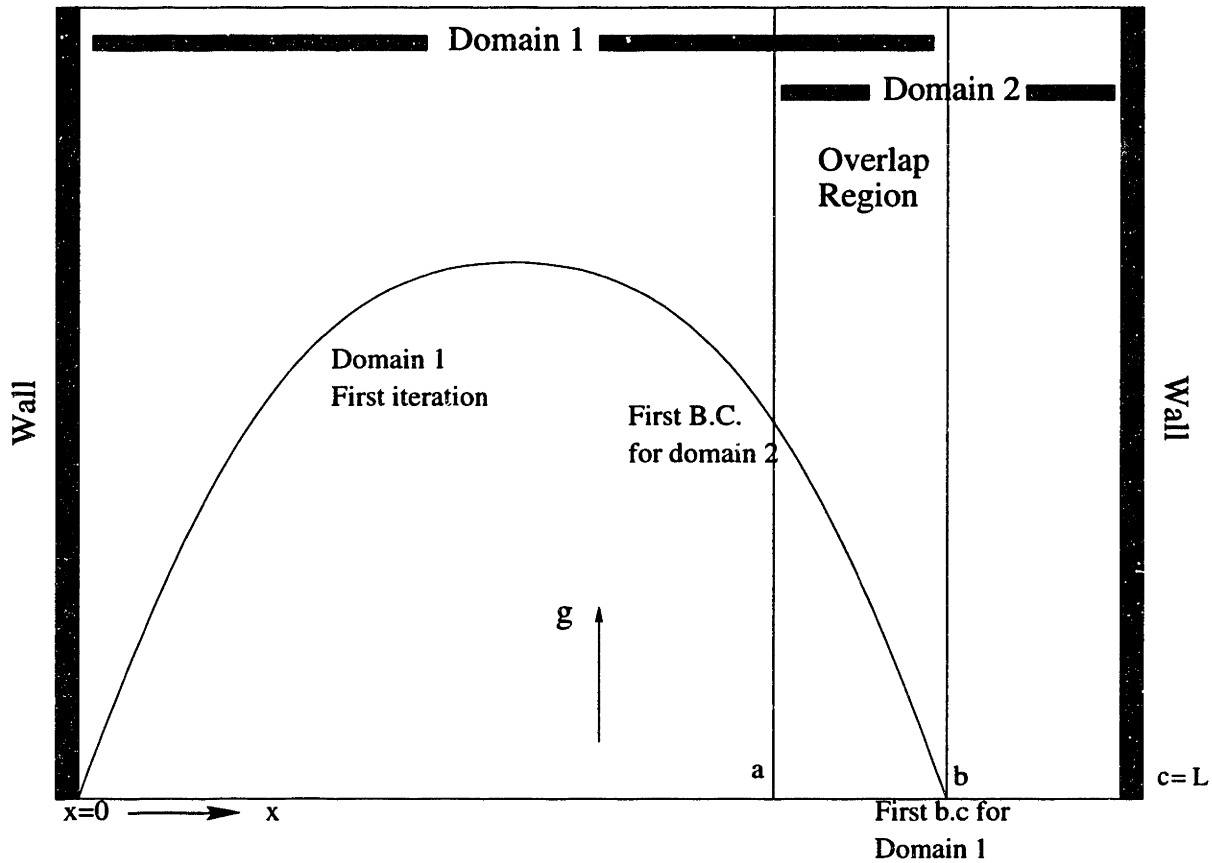

Figure 3-1: First iteration for the Schwarz alternating method. The first continuum solution, based on a boundary condition of $v(x = b) = 0$ given by the original guess solution in the MD region, is shown.

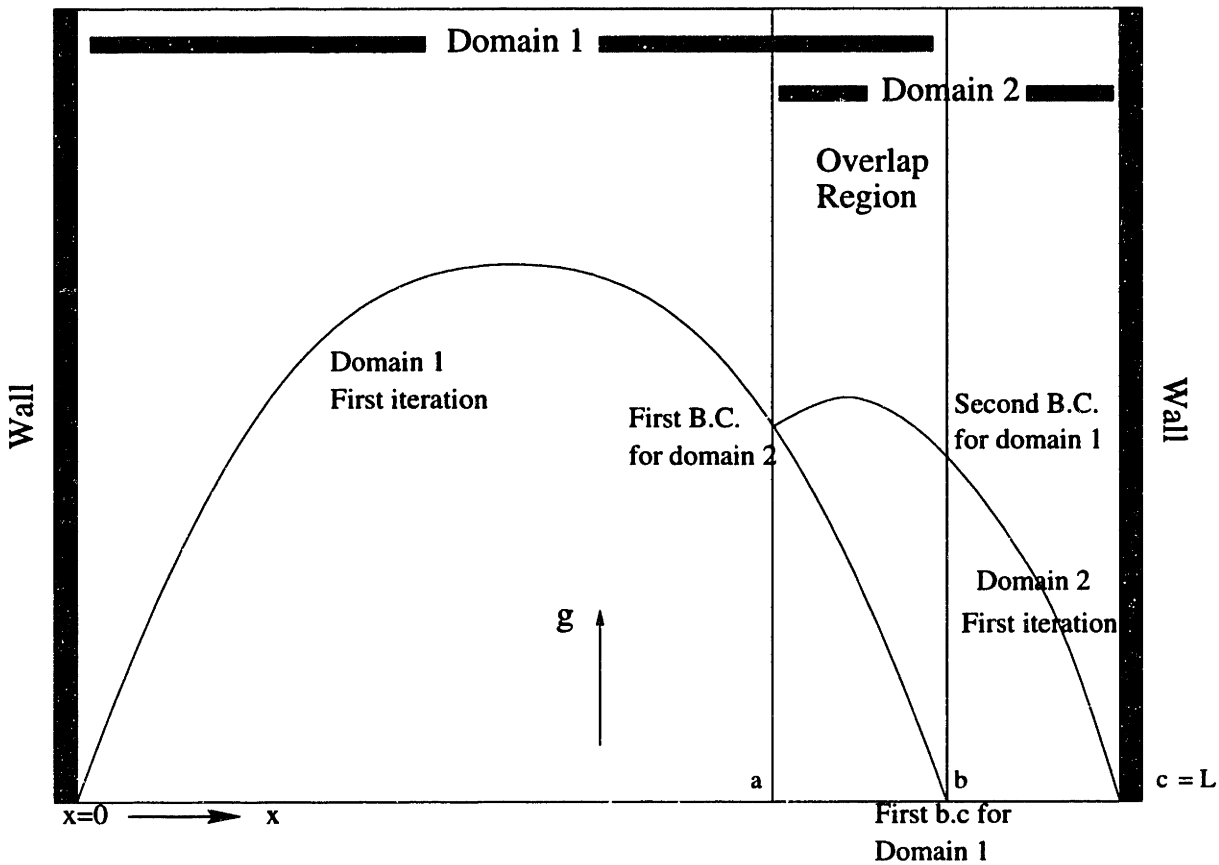

Figure 3-2: First iteration for the Schwarz alternating method. The first molecular solution, based on a boundary condition at $x = a$ given by the continuum solution, has been added.

error contribution of molecular dynamics has to be taken into account.

This overlapping Schwarz method is chosen because it avoids the use, and hence imposition, of fluxes in the matching of solutions on different subdomains. Assuming that the transport coefficients are correctly matched, flux (e.g., stress) continuity is automatically ensured by the agreement in the overlap region of the converged continuum and atomistic representations. The method is also advantageous because it is "implicit," and thus decouples not only length-scales, but also *time-scales*: only steady-state MD simulations are required. Extension of the method to treat time-varying problems on the continuum time-scale is thus possible, in which at *each time* t^n the (say, implicitly) integrated continuum iterate is matched to the previous MD

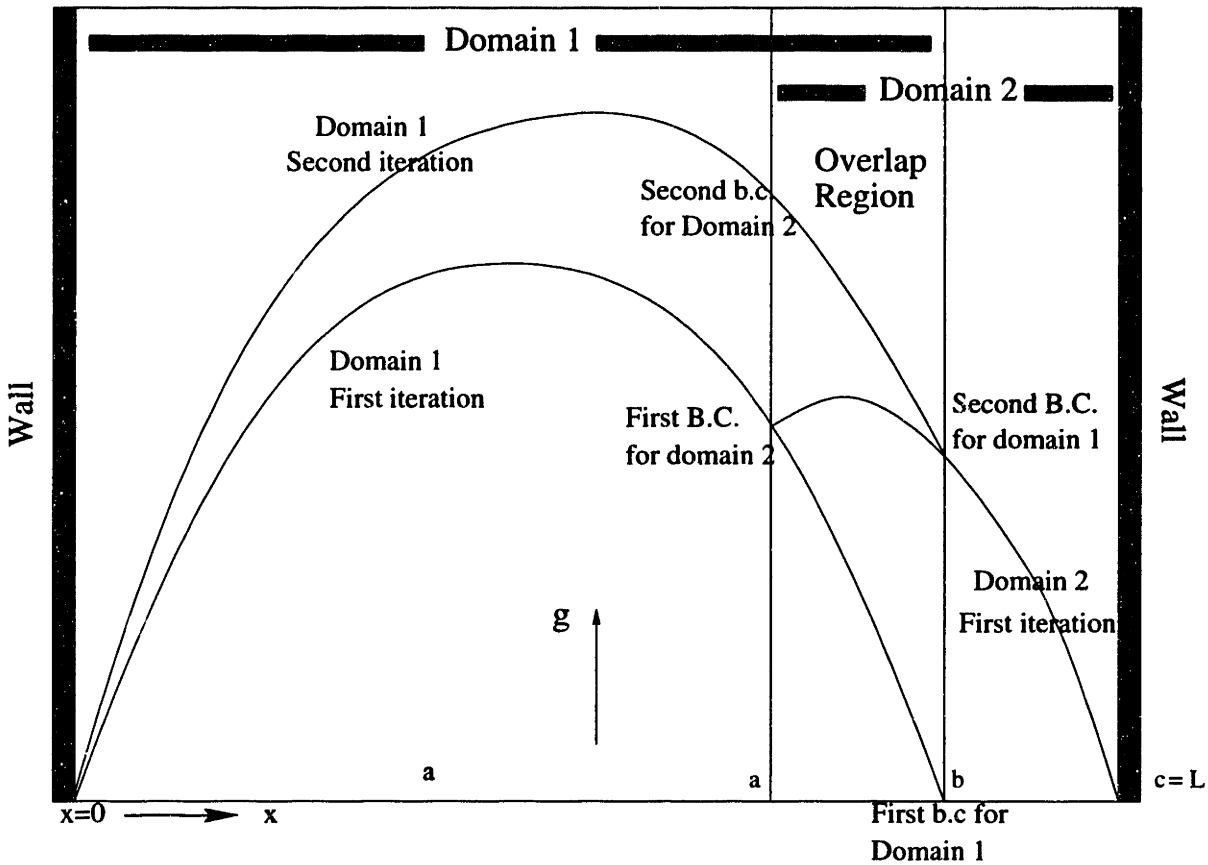

Figure 3-3: Second iteration for the Schwarz alternating method. The new continuum solution, based on a boundary condition at $x = b$ given by the molecular solution of the previous iteration, has been added.

iterate at t^n; given the macroscale timesteps and nanoscale MD domain, the MD calculations may be treated as quasi-static, thus avoiding expensive *coupled* time integration at the molecular time-scales.

3.3 Convergence

Convergence can be proven for a large class of problems when both subdomains are treated by continuum methods [28]. In particular, elliptic problems, such as the ones treated in this thesis, are amenable to analysis which yields useful results: convergence

exhibits a power law behavior of the form

$$\varepsilon^{n+1} = K\varepsilon^n \tag{3.1}$$

where K is a positive constant ($0 < K < 1$) which governs the convergence rate and ε is the error in the appropriate norm [28]. The constant K depends on the particular problem at hand through the operator eigenvalues [28], but also on the size of the overlap region: the larger the overlap region, the smaller K is, and hence the faster the convergence. In the next subsection we illustrate these points with the analysis of the simple Poiseuille problem introduced above.

Convergence should also obtain for a hybrid description if the continuum and molecular models are equivalent in the overlap region. However, additional "steady-state" errors will arise in the hybrid case due to first, discrepancies in the transport coefficients in the two subdomains, second, noise introduced by MD statistical fluctuations, and third, smoothing of the MD data prior to imposition of the boundary conditions on the continuum iterate. The convergence *rate* may also be affected by these new sources of error. These effect of these sources of error is investigated in the following subsection for an one-dimensional case.

3.3.1 Convergence in 1D

Consider the Poiseuille problem defined in section 3.2. We will assume that both domains are treated by continuum techniques. The domain is infinite in the streamwise direction (y) as well as the direction into the plane of the figure (z), the inertial terms are zero and thus, this test problem is a good one-dimensional example of low Reynolds number (Stokes flow)–elliptic problem. Let V_a^n be the velocity at $x = a$ at the n^{th} iteration in domain 1; note that V_a^n will be used as the boundary condition for domain 2 during the n^{th} iteration. The domain 2 iterate will give V_b^n at $x = b$ which is subsequently used as a boundary condition for domain 1 for iteration $n + 1$. The fluid has density ρ, viscosity μ and the acceleration due to gravity in the streamwise

direction is g. Defining $\alpha \equiv a, \beta \equiv (b-a), \gamma \equiv (L-b) = (L-\alpha-\beta)$, we have

$$V_a^{n+1} = \frac{V_b^n \alpha}{\alpha+\beta} - \left(\frac{\rho g}{2\mu}\right)_1 \alpha\beta + \epsilon^n \tag{3.2}$$

$$V_b^n = \frac{V_a^n \gamma}{\beta+\gamma} - \left(\frac{\rho g}{2\mu}\right)_2 \beta\gamma. \tag{3.3}$$

Note that we have allowed for a discrepancy between the transport coefficients in the two domains by allowing for a difference between the values of $\frac{\rho g}{2\mu}$ in the two domains. Here ϵ^n denotes some forcing error other than the discrepancy in transport coefficients that may be present. We now investigate various cases.

Steady state solution with no error

If there is no error in matching transport coefficients $(\frac{\rho g}{2\mu})_1 = (\frac{\rho g}{2\mu})_2 = (\frac{\rho g}{2\mu})$ and $\epsilon^n = 0$, using equations (3.2) and (3.3) we obtain

$$V_a^{n+1} = \frac{\alpha\gamma}{(\alpha+\beta)(\beta+\gamma)} V_a^n - \frac{\rho g}{2\mu}\alpha\beta - \frac{\rho g}{2\mu}\frac{\alpha\beta\gamma}{(\alpha+\beta)}. \tag{3.4}$$

We can find the converged value of V_a, denoted here by V_a^∞, by requiring $V_a^{n+1} = V_a^n = V_a^\infty$ in equation (3.4). This value

$$V_a^\infty = -\frac{\rho g}{2\mu}\alpha(\beta+\gamma) \tag{3.5}$$

is, of course, the value of the velocity at $x = a$ for a Poiseuille profile. The convergence rate is obtained by seeking the error equation: we define the error at iteration n as $\varepsilon^n = V_a^n - V_a^\infty$. Substituting in equation (3.4) we obtain

$$\varepsilon^{n+1} = \frac{\alpha\gamma}{(\alpha+\beta)(\beta+\gamma)}\varepsilon^n. \tag{3.6}$$

We thus conclude that for the Poiseuille problem $K = \frac{\alpha\gamma}{(\alpha+\beta)(\beta+\gamma)}$, which is always less than 1 for non zero overlap. In fact, we can see that the overlap need only be appreciable with respect to one of the subdomains for fast convergence (error decay).

The number of molecules in the system scales with the volume of the overlap region, and hence it is very convenient that the overlap needs to be appreciable with respect to the molecular region and therefore the size of the overlap region does not need to be of macroscopic dimensions for macroscopic problems. In fact, this requirement is crucial for the success of any hybrid technique. The Schwarz method thus ensures that reasonable convergence rates are achieved with the minimum of computational cost, while avoiding the imposition of fluxes that was one of our original requirements.

Steady state solution with error source

In this section we investigate how an error, in the transport coefficient matching say, propagates into the converged solution. Let us assume that $(\frac{\rho g}{2\mu})_2 = (\frac{\rho g}{2\mu})_1 + \nu, \epsilon^n = 0$; the case for which $\epsilon^n \neq 0$ is similar. Equations (3.2) and (3.3) become

$$\tilde{V}_a^{n+1} = \frac{\alpha\gamma}{(\alpha+\beta)(\beta+\gamma)}\tilde{V}_a^n - \left(\frac{\rho g}{2\mu}\right)_1 \alpha\beta - \left(\frac{\rho g}{2\mu}\right)_1 \frac{\alpha\beta\gamma}{(\alpha+\beta)} - \nu\frac{\alpha\beta\gamma}{(\alpha+\beta)}, \tag{3.7}$$

and

$$\tilde{\varepsilon}^{n+1} = \frac{\alpha\gamma}{(\alpha+\beta)(\beta+\gamma)}\tilde{\varepsilon}^n - \nu\frac{\alpha\beta\gamma}{(\alpha+\beta)} \tag{3.8}$$

respectively. The tilde is used to differentiate the exact solution of the previous section from the solution that includes an error source. The steady state error is best expressed as a fraction of the correct solution

$$\frac{\tilde{V}_a^\infty}{V_a^\infty} = 1 + \frac{\tilde{\varepsilon}^\infty}{V_a^\infty} = 1 + \frac{\nu}{(\frac{\rho g}{2\mu})_1}\frac{\gamma}{\alpha+\beta+\gamma}. \tag{3.9}$$

We conclude that the Schwarz method suppresses initial errors ν by $\frac{\gamma}{\alpha+\beta+\gamma} < 1$.

Statistical source of error

We now assume that there is a forcing error ϵ^n that varies with the iteration number n. We expect that a good model for the error contribution of the molecular dynamics simulation which is inherently statistical, is an error forcing term that is stochastic

with the following characteristics:

$$\bar{\epsilon} = \lim_{N\to\infty} \frac{1}{N} \sum_{n=1}^{N} \epsilon^n = 0, \tag{3.10}$$

and

$$Var(\epsilon) = \lim_{N\to\infty} \frac{1}{N} \sum_{n=1}^{N} (\epsilon^n)^2 = \sigma^2. \tag{3.11}$$

Equations (3.2) and (3.3) with $\epsilon^n \neq 0$ lead to

$$\varepsilon^{n+1} = \frac{\alpha\gamma}{(\alpha+\beta)(\beta+\gamma)}\varepsilon^n - \frac{\alpha}{\alpha+\beta}\epsilon^n. \tag{3.12}$$

It can be easily shown (see next section) that

$$\bar{\varepsilon} = \lim_{N\to\infty} \frac{1}{N} \sum_{n=1}^{N} \varepsilon^n = 0, \tag{3.13}$$

and

$$Var(\varepsilon) = \lim_{N\to\infty} \frac{1}{N} \sum_{n=1}^{N} (\varepsilon^n)^2 = \frac{\frac{\alpha^2}{(\alpha+\beta)^2}}{[1 - (\frac{\alpha\gamma}{(\alpha+\beta)(\beta+\gamma)})^2]}\sigma^2. \tag{3.14}$$

We can therefore conclude that when a stochastic source of error is present the mean value of the error goes to zero (as in the unforced case), but there is an expected error that is related to the variance of the forcing term and the convergence characteristics of the iteration.

Although the exact form of the difference equation governing the convergence process was derived here for a one-dimensional case, the form of the equation does not change in higher dimensions [28]. We will use this fact in the next section where we use a general "decay constant" K to examine the possibility of minimizing the computational work in a hybrid technique. This analysis will be valid for any number of dimensions under the assumption that K is known.

3.3.2 Numerical Efficiency Considerations

The computational work associated with a full hybrid solution can, to a very good approximation, be attributed to the molecular part; for each iteration the continuum iterate typically takes two orders of magnitude less computational time than the molecular iterate. In what follows we will neglect the computational cost of the continuum solutions in order to simplify our investigation that aims in minimizing the computational cost of the complete hybrid solution.

If we neglect the continuum cost of the solution we can easily express the total cost (or work W) of the hybrid solution as

$$W = \text{Work per MD timestep} \sum_{i=1}^{n_0} N_i \tag{3.15}$$

where n_0 is the total number of iterations and N_i is the number of molecular dynamics timesteps run at iteration i. Reducing N_i reduces the cost of the hybrid solution but increases the final expected error (see equation (3.14)) through an increased variance σ^2 which scales (equation (2.22)) inversely to the number of samples taken. We would like to know how the error in the initial stages of the iteration propagates or affects the final error present at convergence; if the effect of the error decays sufficiently fast we can design a "schedule" for the number of MD timesteps as a function of the iteration number such that initial MD simulations are run to low accuracy, thus reducing the computational cost.

The exact solution of the error governing equation (3.12) with $K = \frac{\alpha\gamma}{(\alpha+\beta)(\beta+\gamma)}$ is given by

$$\varepsilon^n = \sum_{j=0}^{n-1} K^{n-1-j}\epsilon^j + K^n\varepsilon^0. \tag{3.16}$$

We will now look for the error behavior as a function of the iteration number. The averaged equations (3.13) and (3.14) were obtained by taking the limit of $n \to \infty$ for which the initial condition term goes to zero. Additionally we have assumed that all cross correlation terms ($\lim_{N\to\infty} \frac{1}{N}\sum_{n=1}^{N} \epsilon^n\epsilon^{n+k}, k \neq 0$) go to zero. The limit is, of course, not valid if n is small and therefore for the present analysis we introduce

statistics in an ensemble sense, that is

$$\overline{\varepsilon^n} = \lim_{M\to\infty} \frac{1}{M} \sum_{k=1}^{M} \varepsilon_k^n, \tag{3.17}$$

and

$$Var(\varepsilon^n) = \lim_{M\to\infty} \frac{1}{M} \sum_{k=1}^{M} (\varepsilon_k^n - \overline{\varepsilon^n})^2, \tag{3.18}$$

where $k = 1, ..., M \to \infty$ are the different realizations of similar systems characterized by equation (3.12). Using

$$\overline{\epsilon^n} = \lim_{M\to\infty} \frac{1}{M} \sum_{k=1}^{M} \epsilon_k^n = 0 \ \ \forall n, \tag{3.19}$$

$$Var(\epsilon^n) = \lim_{M\to\infty} \frac{1}{M} \sum_{k=1}^{M} (\epsilon_k^n)^2 = \frac{A^2}{N_n}, \tag{3.20}$$

and

$$Var(\varepsilon^0) = 0, \tag{3.21}$$

it can easily be shown that

$$Var(\varepsilon^{n_0}) = \sum_{j=0}^{n_0-1} K^{2(n-1-j)} Var(\epsilon^j) = \sum_{j=0}^{n_0-1} K^{2(n-1-j)} \frac{A^2}{N_j}. \tag{3.22}$$

Also note that we have again assumed that the cross correlation terms in the ensemble sense ($\lim_{M\to\infty} \frac{1}{M} \sum_{k=1}^{M} \epsilon_k^n \epsilon_{k+j}^n, j \neq 0$) go to zero.

The above equation (3.22) also shows how the results of equation (3.14) were obtained. If $Var(\epsilon^j) = \sigma^2 = const.$ then

$$Var(\varepsilon^{n_0}) = \sigma^2 \sum_{j=0}^{n_0-1} K^{2(n-1-j)} = \sigma^2 \frac{1}{1-K^2} \text{ for } K < 1 \text{ and } n_0 \to \infty. \tag{3.23}$$

We have verified the validity of the above equations with numerical simulations. An ensemble of 1000 members all obeying the difference equation (3.12) was simulated using a random sequence of numbers to model the stochastic term. The results (see Fig. 3-4) verify the correctness of the equations derived above: the mean value of the

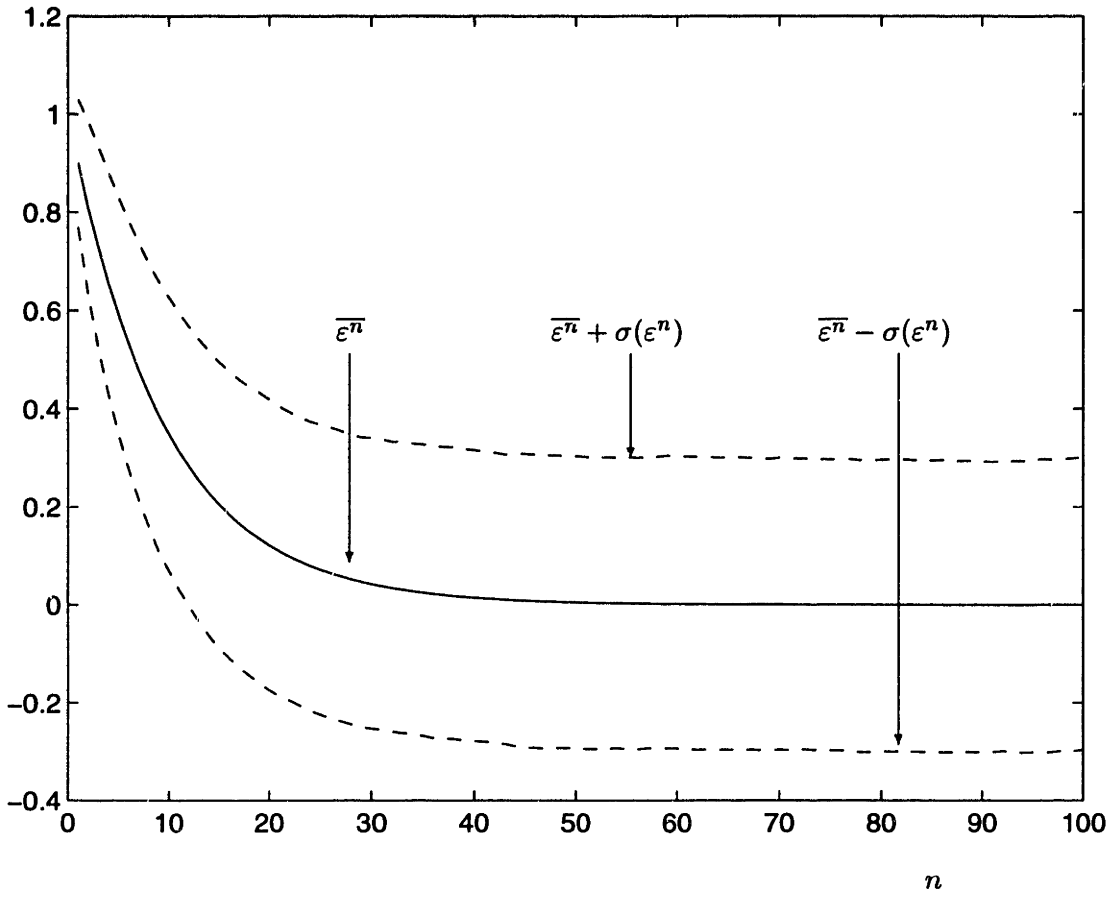

Figure 3-4: Numerical simulation of equation (3.12). n is the iteration number. As explained in the text the results are ensemble (1000 members) averaged. The solid line shows that $\overline{\varepsilon^n}$ decays like the unforced case, whereas the dashed lines show $\overline{\varepsilon^n} \pm \sigma(\varepsilon^n)$.

error decays as in the unforced case, and the expected error (associated with one standard deviation) is given by equation (3.22).

We therefore seek the optimal scheduling of the number of molecular dynamics timesteps as a function of the iteration number by also allowing the number of iterations to vary, subject to the constraint of a desired simulation accuracy. We can pose the constraint as

$$K^{n_0}\varepsilon^0 + \sigma(\varepsilon^{n_0}) = B, \tag{3.24}$$

where in doing so, we have associated one standard deviation of the stochastic part of ε^{n_0} to the expected error and added that to the error at the n_0 iteration due to the deterministic part ($K^{n_0}\varepsilon^0$), and required that it equals B.

We form the Lagrangian

$$\mathcal{L} = \sum_{j=1}^{n_0} N_j + \lambda \left(K^{n_0}\varepsilon^0 + \sqrt{\sum_{j=0}^{n_0-1} K^{2(n-1-j)} \frac{A^2}{N_j}} - B \right) \tag{3.25}$$

which can be differentiated for the extrema

$$\frac{\partial \mathcal{L}}{\partial N_j} = 1 - \frac{\lambda \frac{A^2}{N_j^2} K^{2(n_0-1-j)}}{2\sqrt{\sum_{j=0}^{n_0-1} K^{2(n-1-j)} \frac{A^2}{N_j}}} = 0, \tag{3.26}$$

and

$$\frac{\partial \mathcal{L}}{\partial \lambda} = K^{n_0}\varepsilon^0 + \sqrt{\sum_{j=0}^{n_0-1} K^{2(n-1-j)} \frac{A^2}{N_j}} - B = 0. \tag{3.27}$$

Solving the above equations for N_j we obtain,

$$N_j = \frac{A^2}{(B - K^{n_0}\varepsilon^0)^2} \frac{K^{-1} - K^{n_0-1}}{K^{-1} - 1} K^{n_0-1-j}, \tag{3.28}$$

that is, for a given n_0 the optimum work is achieved for $N_j \propto K^{n_0-1-j}$, with

$$\sigma(\epsilon^j) = \sqrt{\frac{A^2}{N_j}} = \frac{(B - K^{n_0}\varepsilon^0)}{K^{\frac{n_0-1}{2} - \frac{1}{2}}} \sqrt{\frac{K^{-1} - 1}{K^{-1} - K^{n_0-1}}}. \tag{3.29}$$

We will now seek the optimum n_0 by substituting the expression we have found for N_j into equation (3.15) for the cost and finding for which n_0 a minimum obtains. The expression for the cost is

$$W = \frac{A^2}{(B - K^{n_0}\varepsilon^0)^2} \left(\frac{K^{-1} - K^{n_0-1}}{K^{-1} - 1} \right)^2. \tag{3.30}$$

Note that this expression is singular for $B = K^{n_0}\varepsilon^0$ because an infinite number of timesteps is required for the stochastic term to go to zero such that B is balanced only by the initial condition decay term. We can look for minima for $n_0 > lnB/lnK$ ($\varepsilon^0 = 1$) because the branch $n_0 < lnB/lnK$ corresponds to the negative value of the square root in equation (3.30) and represents the case for which $(B - K^{n_0}\varepsilon^0) < 0$. For $n_0 > lnB/lnK$ equation (3.30) is monotonically decreasing and this indicates that

the optimum obtains for $n_0 \to \infty$.

Since an infinite number of iterations is impossible, we show here that this infinity can be replaced by a suitably large number with a very small effect on the work savings. We illustrate this with a numerical example: using $B = 0.3, \varepsilon^0 = 1, K = 0.1, A = 1$ we need $n_0 = 25$ for $\sigma = const. = 0.1$. This translates to a total work of $W = 2500$ (in arbitrary units). Using the scheme derived above, that is

$$N_j = \frac{A^2}{(B - K^{n_0}\varepsilon^0)^2} \frac{K^{-1} - K^{n_0-1}}{K^{-1} - 1} K^{n_0-1-j}, \tag{3.31}$$

with $n_0 = 81$ we find that the error decays to the target value of 0.3, but the work is now $W = 1112.1$. Additionally we can use equation (3.30) to find $W(n_0 \to \infty) = 1111.1$ which shows that less than 0.1% is lost by taking $n_0 = 81$, but also that a factor of 2.5 in savings is obtained through the use of the optimal scheduling technique. Fig. 3-5 shows numerical results obtained by a stochastic simulation; the results verify the theoretical predictions of equation (3.30). The work was also evaluated directly form the stochastic simulation and found to equal the theoretical value of $W = 1112.1$. Further numerical experiments indicate that as $B \to 0$ this scheduling technique becomes more profitable since the gains exceed the value of 3.

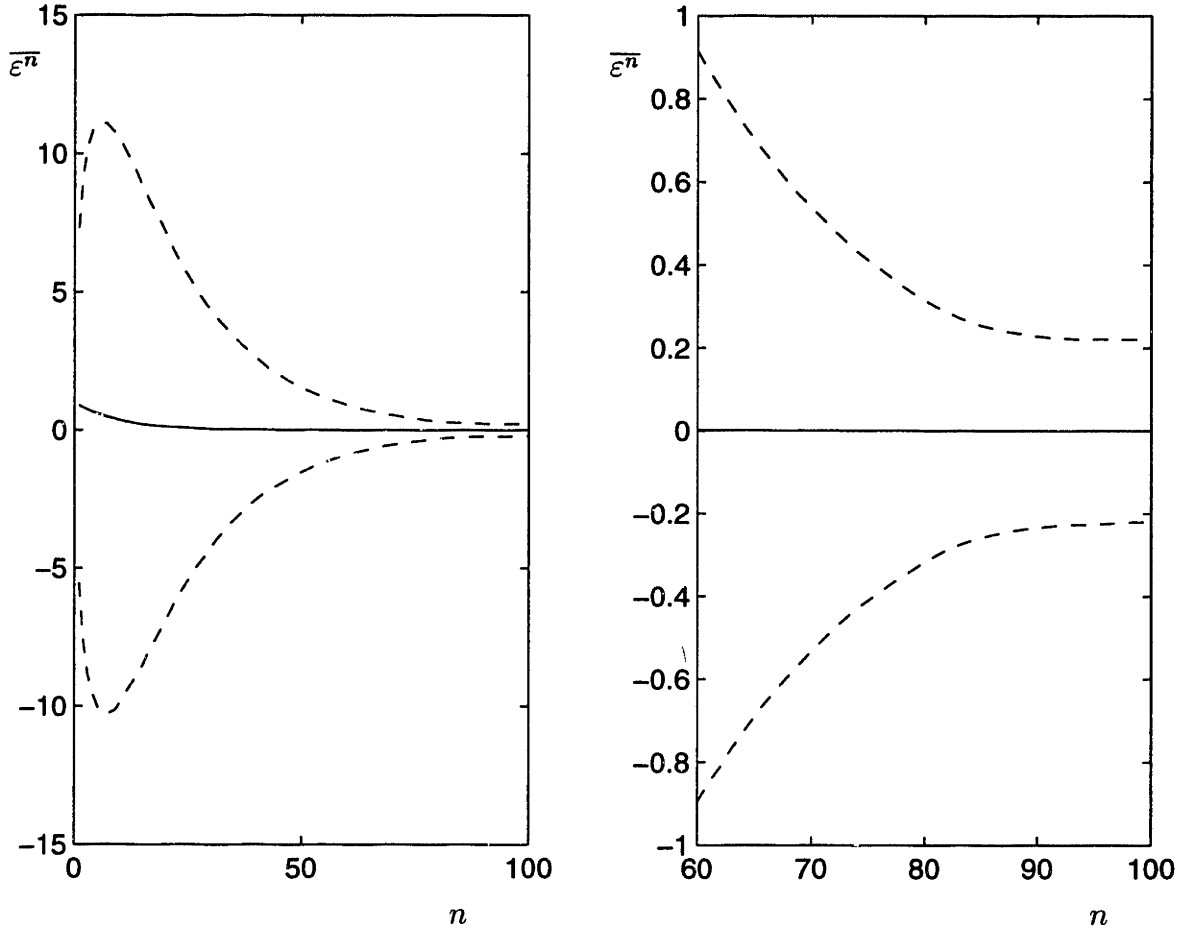

Figure 3-5: Numerical simulation of equation (3.12) for $B = 0.3, \varepsilon^0 = 1, K = 0.1, A = 1$ with $n_0 = 81$. As explained in the text the results are ensemble (1000 members) averaged. n is the iteration number. The solid line shows that $\overline{\varepsilon^n}$ decays like the unforced case, whereas the dashed lines show $\overline{\varepsilon^n} \pm \sigma(\varepsilon^n)$. (a) shows the full results, and (b) shows the crossover ($B = K^{n_0}\varepsilon^0 + \sigma(\varepsilon^{n_0})$) at $n = n_0 = 81$.

Chapter 4

Molecular Dynamics Boundary Condition Imposition

In this chapter we present the technique developed for imposing boundary conditions on molecular dynamics simulations. This is an important requirement of the Schwarz alternating method as explained in the previous chapter. We consider Dirichlet boundary conditions only because the Schwarz formulation avoids the explicit imposition of Neumann boundary conditions that are significantly more difficult to handle as explained in chapter 3. The technique is developed for general three dimensional problems. It is also validated using a two dimensional test problem: flow in an obstructed channel at a Reynolds number of 3.7.

4.1 Boundary Condition Imposition Method

We consider here the problem of imposing arbitrary velocity and temperature boundary conditions on an MD simulation in a *general* geometry $\mathcal{D}$ with associated closed boundary $\partial\mathcal{D}$, denoted by the dashed line in Fig. 4-1. We shall, initially, consider MD regions in the *interior* of the flow, and thus all boundary conditions on the MD domain are of the artificial variety, that is, required solely for purposes of hybrid representation. We thus avoid the issue of molecular walls [26] which, although important, is a purely atomistic issue, and thus separate from the primary "matching"

concerns of the current thesis. Molecular dynamics domains with walls are visited in chapter 8 where the contact line problem is analyzed; the existence of walls does not require any modification of the technique presented here. We assume that the velocity and temperature, as well as the gradient of the velocity and temperature, are known on $\partial\mathcal{D}$, and that we desire the steady-state MD solution everywhere inside $\mathcal{D}$.

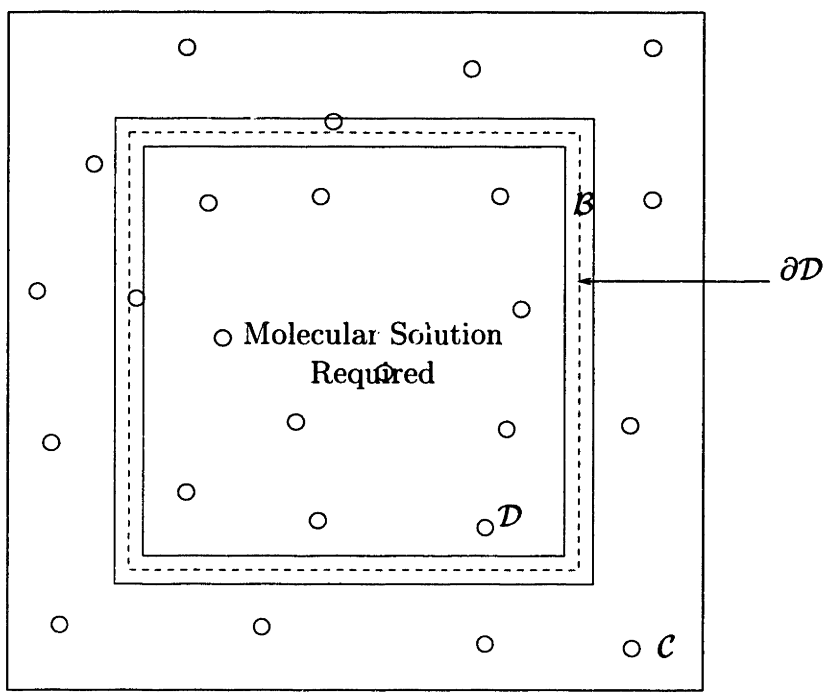

Figure 4-1: Velocity and temperature boundary condition imposition technique.

The boundary conditions are imposed through the artifice of "reservoirs" of fluid that encompass the domain $\mathcal{D}$. In particular, we first introduce a region, or sheath, $\mathcal{B}$, of small but finite thickness δ, that surrounds $\partial\mathcal{D}$. By converting $\partial\mathcal{D}$ from a surface to a volume, we have a finite probability of finding a molecule residing in the vicinity of $\partial\mathcal{D}$ where the boundary condition is expected to apply. While in residence in $\mathcal{B}$, particles are given, at each timestep, a velocity drawn from a Maxwellian distribution

$$P(\vec{v}) = \left(\frac{m}{2\pi k_b T_{bc}}\right)^{3/2} exp^{\frac{-m(\vec{v}-\vec{v}_{bc})^2}{2k_b T_{bc}}} \tag{4.1}$$

where the mean and variance of the distribution, $\vec{v}_{bc}$ and T_{bc} respectively, are given by the desired velocity and temperature of the fluid, in a local equilibrium sense [17]. The desired velocity and temperature of the fluid are constructed from a first-order Taylor series expansion based on the known values of the velocity, temperature and velocity and temperature (normal) gradients on $\partial\mathcal{D}$. (We prefer the Taylor series approach over pointwise matching everywhere in $\mathcal{B}$ because the former is much less cumbersome and storage-intensive. For our Taylor series approach to be valid, δ must be small compared to the length-scale over which the continuum solution varies appreciably.)

Finally, we provide a continuous supply of molecules to and from $\mathcal{D}$ by enclosing $\mathcal{D} \bigcup \mathcal{B}$ in a larger, periodic domain $\mathcal{C}$; $\mathcal{C} \setminus (\mathcal{D} \bigcup \mathcal{B})$ acts as particle reservoir that, for incompressible problems, ensures that there is no *net* mass flow into $\mathcal{D}$. (Note $\mathcal{C} \setminus (\mathcal{D} \bigcup \mathcal{B})$ refers to $\mathcal{C}$ with $\mathcal{D} \bigcup \mathcal{B}$ removed.) In order to see why the particle reservoir correctly accounts for the correct feed of molecules across $\partial\mathcal{D}$ in incompressible systems we make two observations; first, the net mass flux through any closed surface is zero if the Mach (M) number is sufficiently small, and second, $\partial\mathcal{D}$ also "encloses" the outside particle reservoir because the latter is periodic. Therefore, an incompressible set of boundary conditions ($\int_{\partial\mathcal{D}} \vec{v}_{bc} \cdot \hat{n} = 0$, where $\hat{n}$ is the unit normal vector on $\partial\mathcal{D}$) not only produces the required solution inside $\mathcal{D}$, but also produces the solution to the problem in $\mathcal{C} \setminus (\mathcal{D} \bigcup \mathcal{B})$ which is the one of the correct feed of molecules on $\partial\mathcal{D}$. Extension to substantially compressible systems has not yet been considered.

The errors introduced by this method of imposing boundary conditions originate in the not strictly correct dynamical state of the particles in $\mathcal{C} \setminus \mathcal{D}$, in particular $\mathcal{C} \setminus (\mathcal{D} \bigcup \mathcal{B})$, with which particles in $\mathcal{D}$ interact. It has been shown that the adoption of local Maxwellian distributions results in slip for hard sphere systems [22]; although these results have not been extended to molecular dynamics simulations we expect them to be qualitatively valid as [42] verifies. The incorporation of information about the *gradient* of the required boundary conditions in $\mathcal{B}$ – not just the function values, as one might anticipate from the continuum case – addresses, and largely alleviates, this problem. If necessary, the width of $\mathcal{B}$, δ, can be chosen such that

$\delta > r_c$, thus at least shielding particles in $\mathcal{D}$ from the reservoir $\mathcal{C} \setminus (\mathcal{B} \bigcup \mathcal{D})$; here r_c is the Lennard-Jones interaction-potential cut-off. The Maxwellian equilibrium distributions assumed in $\mathcal{B}$ constitute another source of error; this error will be small if the time-scale, or equivalently length-scale, over which the particle distribution functions relax to the correct non-equilibrium forms is small compared to the size of $\mathcal{D}$. Non-equilibrium simulations performed by the author have confirmed earlier findings [42] that bulk equilibrium *and* non-equilibrium properties are, indeed, unaffected by Maxwellian distribution–based boundary conditions, the effects of which (including slip) remain localized near the simulation boundary. Although distribution functions for dense fluids in non-equilibrium flows could be used [17], the latter are not too well characterized, and thus empirical constructions would be required.

Several alternatives to the above "Maxwell Demon" (in fact a "two–sided" fair demon) method are possible. For example, we have also considered a method by which $\mathcal{B}$ is subdivided into smaller regions along $\partial\mathcal{D}$ in which the particles are continuously "rescaled" to the desired local mean velocity and temperature. In the latter rescaling process, all particles receive a velocity increment such that their mean velocity matches the desired value, and all velocity fluctuations about this mean are scaled such that the temperature of the subregion matches the requisite boundary condition. This strategy is very similar to the constrained Lagrangian dynamics technique of [31]. In their work O'Connell et al. impose boundary conditions as constraints on the equations of motion of the particles. For example a velocity boundary condition of $\vec{v}_{bc}$ at a point A would be formulated as a constraint on the average velocity of the molecules in a small region Π surrounding A, in a direct analogy to the definition of macroscopic properties form microscopic data. Hence

$$\sum_{i}^{N} \vec{p}_i = M\vec{v}_{bc} \tag{4.2}$$

constrains the N molecules in region Π, which have a total mass M, to have a mean velocity $\vec{v}_{bc}$. This constraint can be incorporated in the equation of motion of these

molecules through a Lagrange multiplier ξ to give [31]

$$\dot{\vec{r}}_i = \frac{\vec{p}_i}{m} + \xi[\frac{M}{m_i N}\vec{v}_{bc} - \frac{1}{N}\sum_k^N \frac{\vec{p}_k}{m_k}] \tag{4.3}$$

and

$$\dot{\vec{p}}_i = -\vec{\nabla}V. \tag{4.4}$$

Note that these equations are valid only in Π. In the neighboring region $\vec{v}_{bc}$ changes. Our rescaling technique corresponds to the limit of $\xi \to \infty$. The main disadvantage of this method is the discrete nature of this imposition as opposed to the continuum nature of the "Maxwellian Demon" used in this work. We find that the "Maxwell Demon" approach, though less sophisticated, typically performs better than these more subtle constraints on the particle motion. To our knowledge, neither method is proven to reproduce the correct physical dynamics [10], and hence both will no doubt introduce local errors in the non-equilibrium distribution functions.

4.2 Validation

4.2.1 Model Problem Statement

In this section we describe the model problem with which we validate our techniques for imposing MD boundary conditions and for matching the continuum and molecular representations (chapter 5). The problem chosen had to satisfy two requirements. First, the problem had to be fairly complex and hence a good test for the applicability of our technique, and second, the fully continuum solution of the problem could be taken as exact. The problem chosen is flow in the "obstructed" channel domain Ω, a sketch of which is shown in Fig. 4-2, with parabolic inflow velocity profile, no stress ("outflow") boundary conditions downstream, and no-slip velocity conditions at all solid walls. The channel length has $L = 300$Å and height $H = 150$Å. The flow is "obstructed" by a square block with side $l_b = 30$Å residing in the middle of the channel.

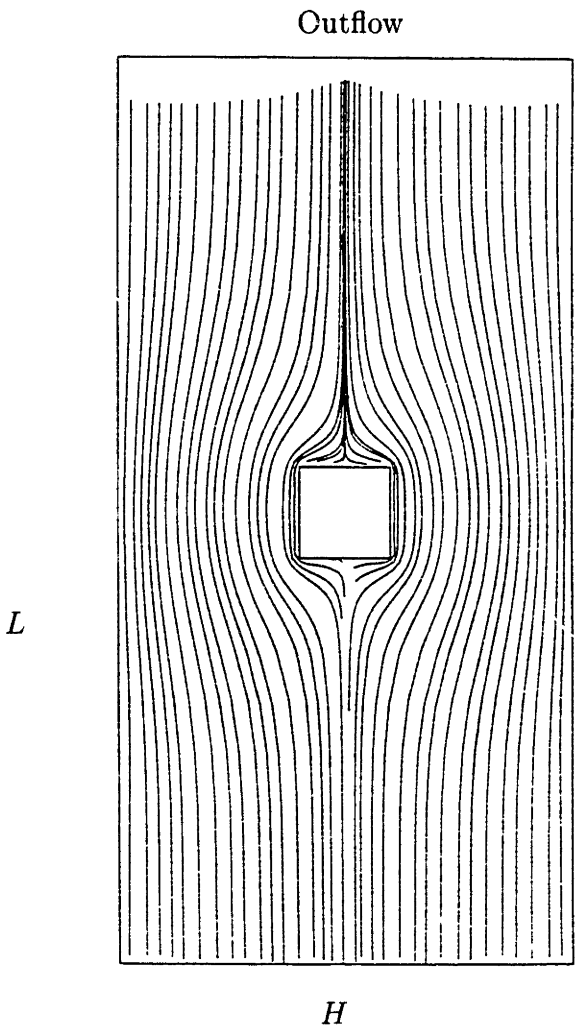

Figure 4-2: Model problem geometry.

A fully continuum spectral element discretization of the incompressible Navier-Stokes equations serves as the reference exact solution. The Reynolds number $R = \rho\overline{U}H/\mu$ is 3.7 based on the channel height and imposed mean flow velocity $\overline{U} = 52.1m/s$. The viscosity $\mu = 3\times10^{-4}Kg/ms$ of Argon at the specified temperature $T = 110^o$ K and density $\rho = 1420\ Kg/m^3$ is known experimentally [1], and independently confirmed by the non-equilibrium MD simulations of the author and others [42]. We assume on the continuum side that the flow is incompressible, isothermal, and constant-property; we can make no such "assumptions" on the molecular side, as described below.

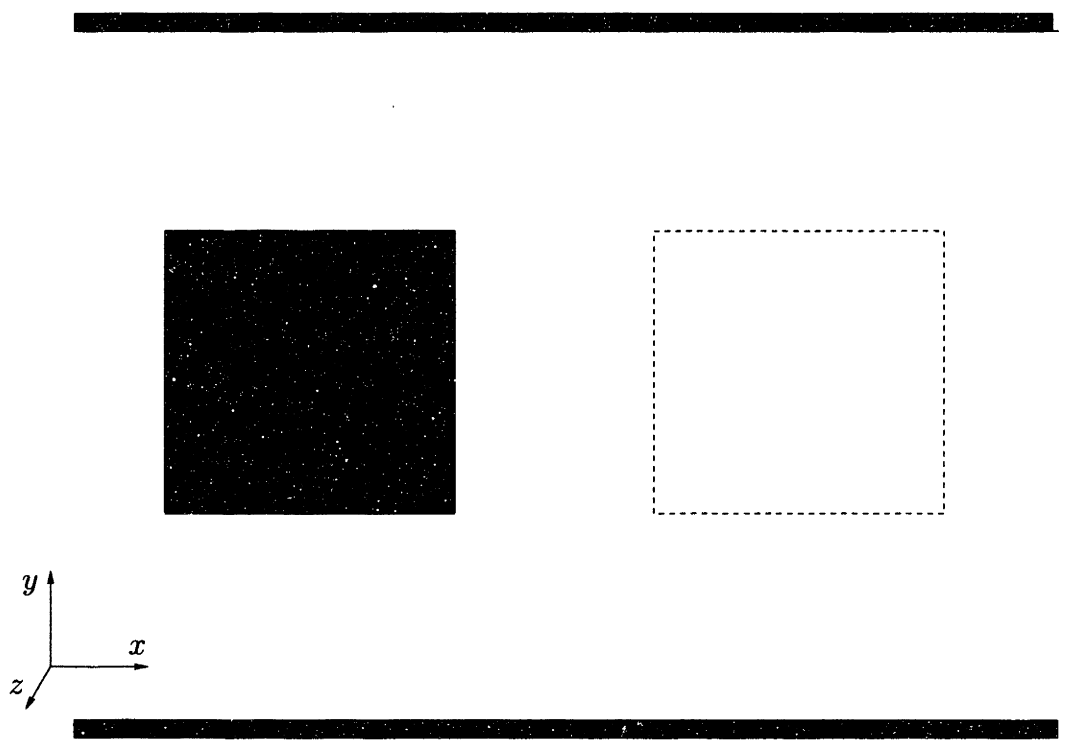

Figure 4-3: Sketch of the obstructed channel problem. The comparison takes place in the region enclosed by the dashed line. The shaded square is the solid block in the middle of the channel (Figure not to scale).

The region of the flow represented by the MD calculation, $\mathcal{D}$ is the wake region

behind the square block in the middle of the channel, as shown in Fig. 4-3; $\mathcal{D}$ measures $(\ell_{\mathcal{D}} \times \ell_{\mathcal{D}} \times 8.82\sigma)$ with $\ell_{\mathcal{D}} = 8.82\sigma = 30\text{Å}$. This MD domain is chosen because the "wake" region behind the block is strongly non-parallel, and thus serves as a good test for the method, yet is far enough from all walls that continuum behavior should obtain. The latter, of course, does not make for an interesting "real" application, but does allow for a controlled study of the approach. In a real application, the MD simulation would be applied in a region $\mathcal{D}$ in the interior of which the continuum description is presumably not adequate.

4.2.2 Molecular Dynamics Simulations

The actual MD calculation is performed on a box $\mathcal{D}'$, *dynamically similar* to $\mathcal{D}$, which measures $\ell'_{\mathcal{D}'} \times \ell'_{\mathcal{D}'} \times 8.82$, with $\ell'_{\mathcal{D}'} = 11.47\sigma = 39\text{Å}$. Denoting the (say maximum streamwise) velocity on $\partial\mathcal{D}$ dictated by the continuum as $u_{\mathcal{D}}$, we impose on $\partial\mathcal{D}'$ the scaled velocity $u'_{\mathcal{D}'} = (\ell_{\mathcal{D}}/\ell'_{\mathcal{D}'})u_{\mathcal{D}}$. Since we specify the same material $(\varepsilon_{Ar}, \sigma_{Ar})$ and thermodynamic state $(T' = T,\ \rho' = \rho)$ in both $\mathcal{D}$ and $\mathcal{D}'$, $\mu' = \mu$, and it then follows that, in the incompressible limit, the flows in $\mathcal{D}$ and $\mathcal{D}'$ are dynamically similar. Note we choose $\ell'_{\mathcal{D}'} > \ell_{\mathcal{D}}$ and hence $u'_{\mathcal{D}'} < u_{\mathcal{D}}$ to reduce compressibility and temperature variation due to viscous heating, as both these effects are absent in our continuum model. However, we can not choose $\ell'_{\mathcal{D}'}$ too large or $u'_{\mathcal{D}'}$ too small as the number of molecules will increase prohibitively, and the signal-to-noise ratio will degrade, respectively. To complete the specification of the MD problem, we choose $\delta' = 0.88\sigma$ for the thickness of $\mathcal{B}'$, and a box of extent $(20.3\sigma \times 20.3\sigma \times 8.82\sigma)$ for $\mathcal{C}'$. The interaction potential cutoff is set to the conservative value $r'_c = 3\sigma$. Note that we shall present quantities in "original" units, that is, we rescale all MD results obtained on $\mathcal{D}'$ back to $\mathcal{D}$ prior to presentation.

4.2.3 Procedure

To validate the method of imposing boundary conditions described in section 4.1, the exact (spectral element) solution on the dashed line in Fig. 4-3 of our model problem

is used on $\partial\mathcal{D}$ as the boundary condition for an MD simulation, and the resulting MD predictions in the interior of $\mathcal{D}$ are then compared to the reference fully continuum solution.

Fig. 4-4 and Fig. 4-5 show good agreement between the reference solution and the MD results, even well away from the region $\mathcal{B}$ in which the MD simulation receives boundary data. The MD simulations are integrated to a statistical accuracy of approximately $\pm 1 m/s$; averaging here, and in the Schwarz iteration of the next chapter, is performed over $(1.15\sigma \times 1.15\sigma \times 8.82\sigma)$ pencils in space, and 4800τ intervals in time, after reaching a stationary state in approximately 1000τ. As shown in the next section the statistical inefficiency was estimated to be $s = 7.5$.

Our simulations were also used to assess the agreement between the various components of the stress tensor in the continuum and molecular solutions at one location– the middle of the molecular (test) region. The computation of the components of the stress tensor is extremely costly and as a result we limited the investigation to one point in the computational domain; the correct stress evaluation requires that all molecules within the cutoff region r_c be taken into account since stress is non-local. Due to this large cost and large memory requirements the number of samples taken was limited and consequently the statistical error is significant.

The continuum (exact) solution stress field in the middle of $\mathcal{D}$ was given by

$$\begin{aligned} \tau_{xx} = 2\mu\frac{\partial v_x}{\partial x} &= -4.5 \times 10^6 Pa \\ \tau_{xy} = \tau_{yx} = \mu(\frac{\partial v_x}{\partial y} + \frac{\partial v_y}{\partial x}) &= -2.7 \times 10^6 Pa \\ \tau_{yy} = -\tau_{xx} = 2\mu\frac{\partial v_y}{\partial y} &= 4.5 \times 10^6 Pa. \end{aligned} \tag{4.5}$$

Note that the solution in the z direction is homogeneous and hence $\tau_{zz} = \tau_{xz} = \tau_{zx} = \tau_{yz} = \tau_{zy} = 0$. Our simulation results for the stress tensor defined in chapter 2 give

$$\Pi_{xx} = 6.7 \times 10^7 Pa \tag{4.6}$$

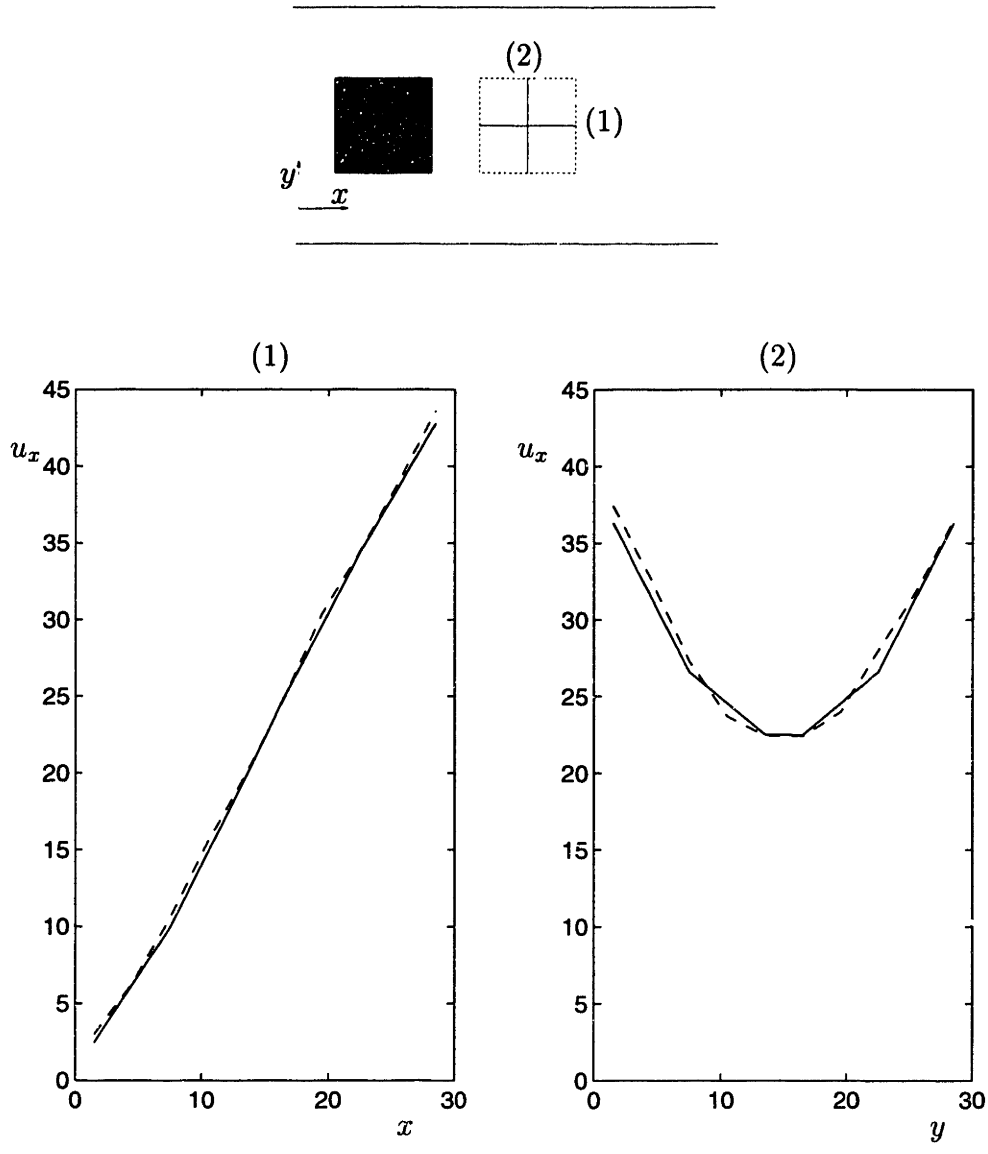

Figure 4-4: Comparison between fully continuum (solid) and MD (dashed) solutions in the interior of $\mathcal{D}$. The velocities are in m/s and the lengths x, y in Å. The graphs correspond to the constant-y (1) and constant-x (2) slices indicated above.

Table 4.1: Stress comparison for the flow in an obstructed channel. Stresses in Pascals.

Component	xx	xy	yy
T	-2×10^6	-2.3×10^6	4.5×10^6
τ	-4.5×10^6	-2.7×10^6	4.5×10^6

$$\Pi_{xy} = -2.3 \times 10^6 Pa$$
$$\Pi_{yy} = 7.32 \times 10^7 Pa$$
$$\Pi_{zz} = -6.6 \times 10^7 Pa.$$

We can subtract the thermodynamic pressure $P = \frac{1}{3}Tr(\Pi) = 6.9 \times 10^7$, to find

$$T_{xx} = -2 \times 10^6 Pa \tag{4.7}$$
$$T_{xy} = -2.3 \times 10^6 Pa$$
$$T_{yy} = 4.5 \times 10^6 Pa.$$

The results are summarized in table 4.1 to facilitate comparison. We see that the agreement is reasonable given a sampling error of the order of $\pm 3 \times 10^6 Pa$.

4.2.4 Estimation of Statistical Inefficiency

In this section we present the estimation of the statistical inefficiency for the flow velocity. In the previous section we have shown the comparison between the molecular and continuum solutions on $\mathcal{D}$; an essential part in assessing the agreement between those two solutions is an accurate estimation of the sampling error originating form the statistical nature of molecular dynamics simulations and the finite number of samples taken. If the difference between the two solutions is within the sampling error estimate then we can conclude that the two solutions agree.

The procedure follows the derivation of expression (2.21) given in section 2.4.4.

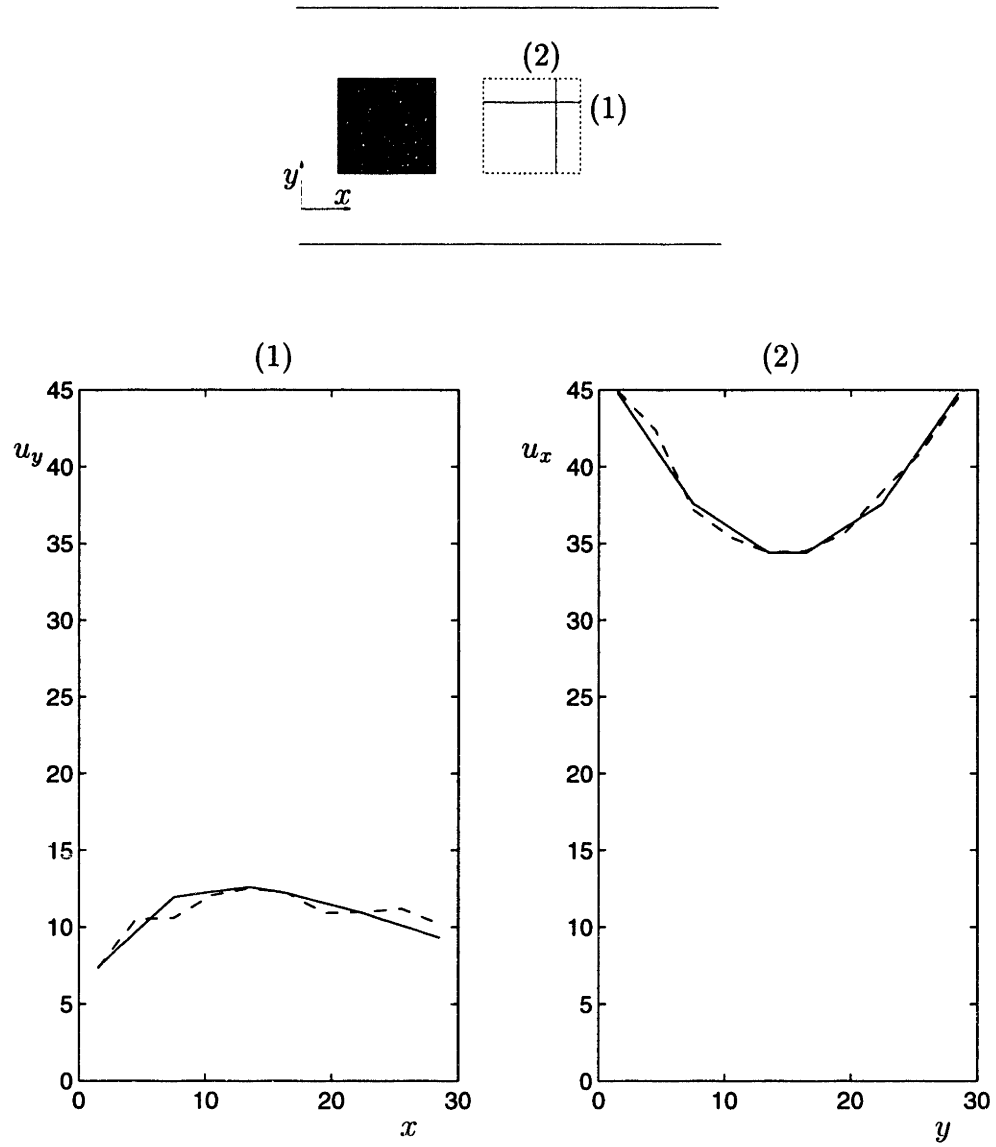

Figure 4-5: Comparison between fully continuum (solid) and MD (dashed) solutions in the interior of $\mathcal{D}$. The velocities are in m/s and the lengths x, y in Å. The graphs correspond to the constant-y (1) and constant-x (2) slices indicated above.

Using the data from the simulations described in section 4.2 we can first calculate $\sigma^2(v)$, which corresponds to the "population variance" of the velocity (in each of the three directions) for every one of the 100 bins in which $\mathcal{D}$ is divided. We expect that $\sigma^2(v)$ is independent of the location (bin coordinates) and velocity component, so that a single average value over all bins and velocity directions is calculated and found to equal $\sigma^2(v) = 2400$. We then divide the simulation data in blocks of length (in time) τ_b and calculate the statistics of these blocks ($\langle v \rangle_b$), $\sigma^2(\langle v \rangle_b)$) as explained in section 2.4.4.

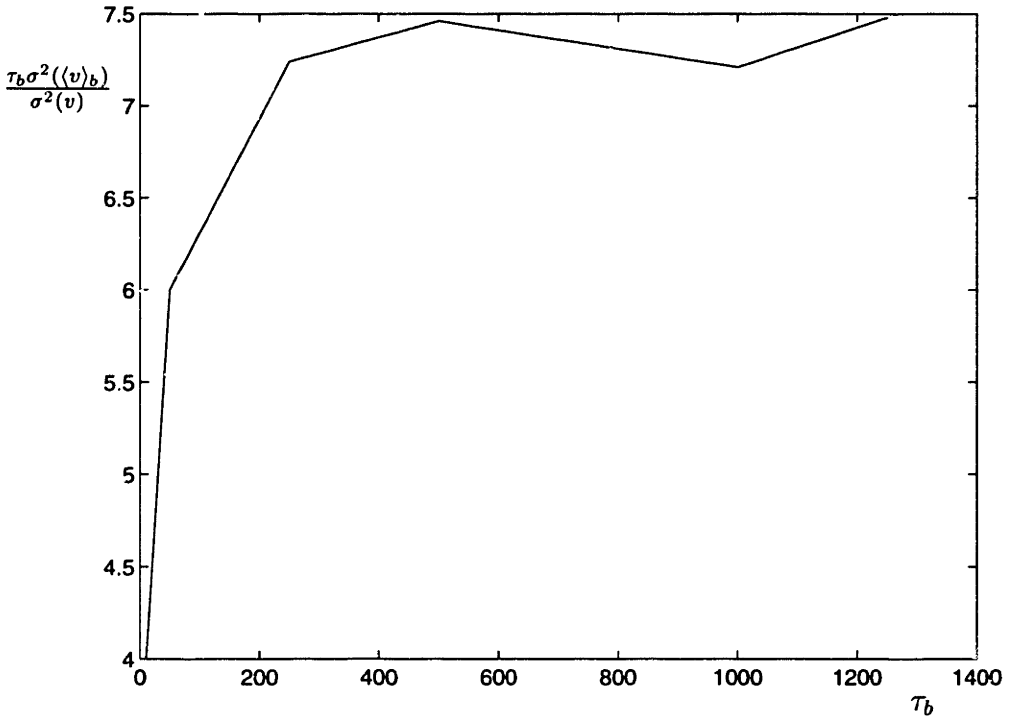

Figure 4-6: Plot of $\frac{\tau_b \sigma^2(\langle v \rangle_b)}{\sigma^2(v)}$ versus τ_b. The statistical inefficiency is the limiting value of $\frac{\tau_b \sigma^2(\langle v \rangle_b)}{\sigma^2(v)} \to 7.5$ as $\tau_b \to \infty$.

Fig. 4-6 shows the variation of $\frac{\tau_b \sigma^2(\langle v \rangle_b)}{\sigma^2(v)}$ versus τ_b; an asymptote of $s = 7.5$ is reached as τ_b increases. We thus conclude that every approximately 7.5 samples, only one contributes new information. The samples were taken every 10 timesteps

and hence it takes 75 timesteps, or approximately 2τ, for two samples to become statistically independent. We can thus estimate the statistical error of our 4800τ runs by treating the whole sequence of data as a single block of length $\tau_b = 4800\tau$; therefore

$$\sigma(\langle v \rangle_b) = \sqrt{\frac{2400}{18000/7.5}} = 1m/s. \tag{4.8}$$

Fig. 4-7 shows the comparison between the results of the simulations presented in Fig. 4-4 and Fig. 4-5 and simulations run at half the number of timesteps (2400τ) with an associated expected error of $\sqrt{2} \times \sigma(\langle v \rangle_b) = 1.4m/s$. We see that the agreement with the continuum results deteriorates with decreasing number of samples. We also conclude that the error estimates are reasonably accurate.

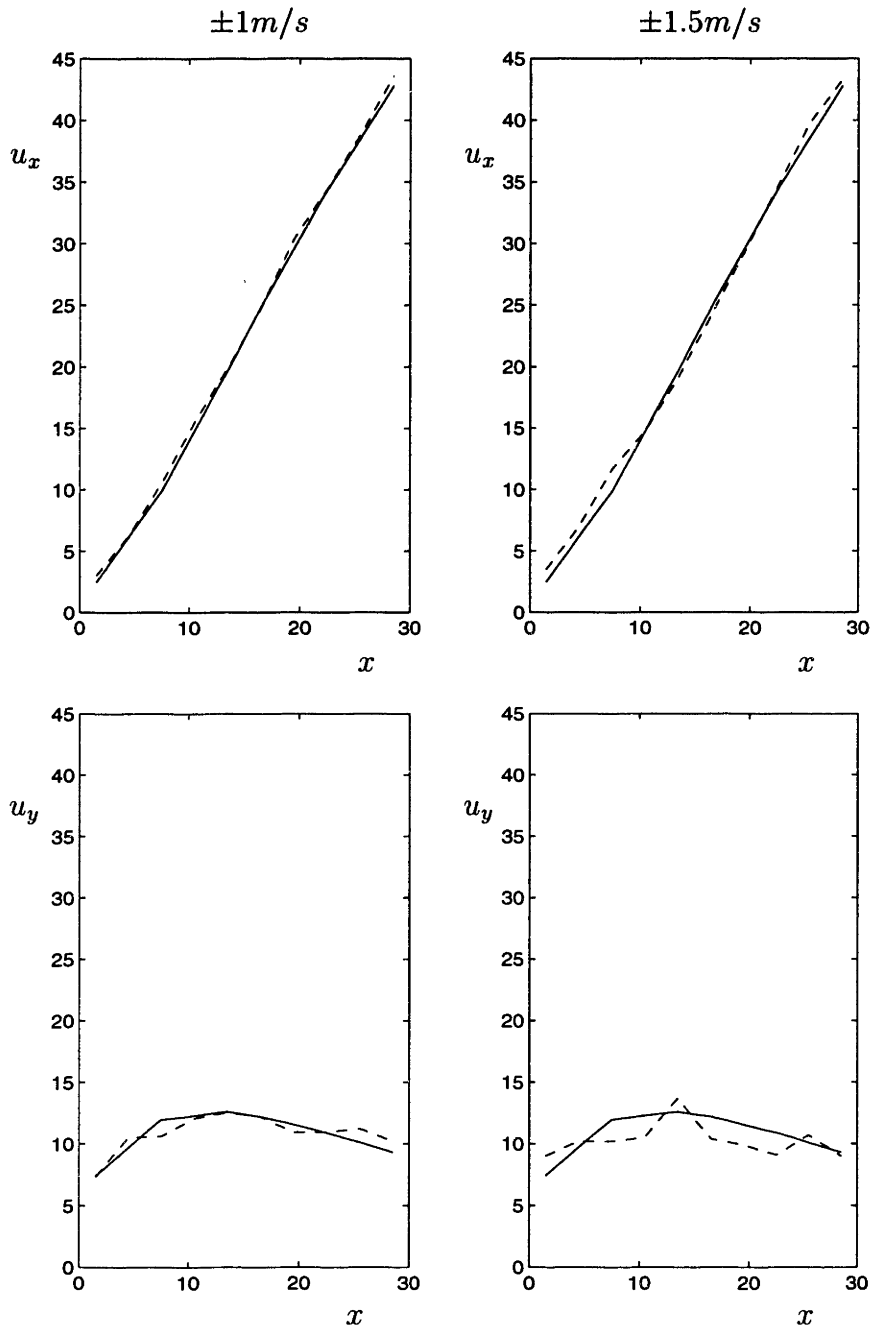

Figure 4-7: Comparison between solutions run to two simulation accuracies to the exact (continuum) solution. The continuum solution is the solid line.

Chapter 5

Hybrid Single-Fluid Formulation

We have shown in chapter 4 that the boundary condition imposition technique proposed in the same chapter can be successfully applied for general and arbitrary boundary conditions. This technique is an essential ingredient of our hybrid method; it is responsible for the correct transfer of information from the continuum to the molecular iterate. The transfer of information from the molecular to the continuum iterate is relatively simple, mainly because the process by which boundary conditions are imposed on continuum numerical solution techniques is well known [33]. The extraction of these boundary conditions from the molecular dynamics simulation follows directly from the methodology of defining and calculating macroscopic fields from molecular data described in section 2.4. We find that the simulation results are much improved if the molecular data are smoothed and corrected for net mass flow before being passed on to the continuum iterate. Both these "corrections" are a direct consequence of the statistical nature of the molecular simulations and are explained in the following section.

In this chapter we present a full hybrid formulation for the test problem of chapter 4. This is the next step in the validation procedure for the hybrid atomistic-continuum technique developed in this thesis. In the following sections we describe the numerical procedure and present the results of the validation test. As pointed out in the previous chapter, this test of the hybrid solution implicitly assumes that a fully continuum treatment of the test problem is adequate and that its spectral element solution can

be taken to be exact. For this to be true the no-slip boundary condition at the solid boundaries has to be valid and therefore the use of molecular dynamics close to the walls was precluded.

5.1 Hybrid Solution Algorithm

We use the test problem introduced in section 4.2 to validate the hybrid solution algorithm developed in chapters 3 and 4. The objective is to reproduce the fully continuum solution (spectral element) shown in Fig. 4-2 through a hybrid MD-continuum numerical solution with a molecular region shown in the sketch of Fig. 5-1. Fig. 5-1 also shows the domain of the continuum part of the calculation, $\mathcal{Q} = \Omega \setminus \mathcal{M}$, which is everything *outside* the "MD-only" hatched region $\mathcal{M}$; the MD region of the calculation, $\mathcal{D}$, and associated reservoirs $\mathcal{B}$ and $\mathcal{C}$; and the overlap region, $\mathcal{Q} \bigcap \mathcal{D}$. Recall that we piece together the solution as continuum in $\Omega \setminus \mathcal{D}$, molecular in $\mathcal{M}$, and continuum *or* molecular in $\mathcal{Q} \bigcap \mathcal{D}$.

5.2 Validation

Fig. 5-2 shows schematically the Schwarz procedure for this two-dimensional problem. The boundary conditions on the continuum spectral element incompressible Navier-Stokes calculation are known on all portions of $\partial\mathcal{Q}$ save $\Gamma = \partial\mathcal{M}$, where the conditions are provided by the MD calculation as part of the Schwarz procedure. The continuum problem is well posed and can be integrated in $\mathcal{Q} = \Omega \setminus \mathcal{M}$. The MD domain obtains boundary conditions for $\partial\mathcal{D}$ from the continuum solution on $\mathcal{B} \subset \mathcal{Q}$, to generate a new set of boundary data on $\Gamma = \partial\mathcal{M}$ to be used by the next continuum iterate. When the boundary data on $\Gamma = \partial\mathcal{M}$ are the same as in the previous iteration the "driving force" for change goes to zero and convergence obtains. Although the equality of the continuum and molecular solutions on $\Gamma = \partial\mathcal{M}$ and/or $\partial\mathcal{D}$ implies that some form of convergence/limit cycle has been reached, this condition is not sufficient for the correctness of the solution. As shown in section 3.3, if a transport

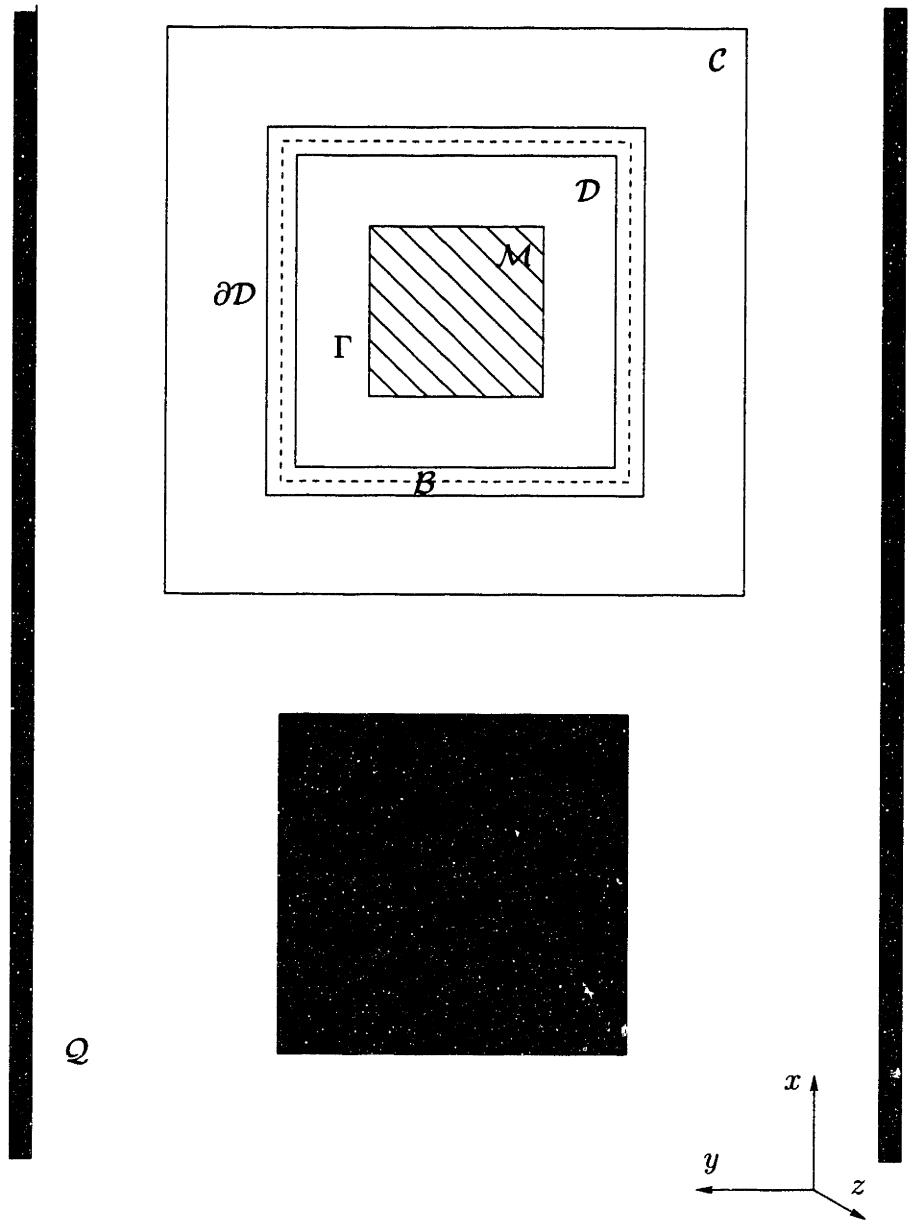

Figure 5-1: Hybrid calculation domain decomposition (not to scale). The actual ratio of the volume of $\mathcal{D}$ to the volume of the entire domain $\mathcal{Q}$ is 1/50, and in practice could be much smaller.

coefficient is incorrectly matched, convergence obtains albeit with a steady state error which is a result of the difference in first or higher order derivatives of the continuum and molecular solution in the overlap region. Convergence thus strictly obtains when the molecular and continuum solutions are identical through the whole extent of the overlap region including the boundaries $\Gamma = \partial\mathcal{M}$ and $\partial\mathcal{D}$.

Although the continuum calculation is two dimensional, the MD simulation is three-dimensional. However we consider Γ to be effectively defined in the (x, y) plane, since only z-averaged information passes between the two representations. Note that the MD-derived field variables on Γ are smoothed – fitted by a low-order (here 3^{rd}-order) polynomial – prior to imposition on the subsequent continuum iterate. The analysis of the effect of the smoothing on the results of the hybrid technique will be the subject of future work; it is introduced here to inhibit the appearance of oscillatory numerical instabilities to which the high order spectral element technique is vulnerable.

To ensure that the continuum boundary data satisfies zero-mass-flux though Γ, the MD smoothed data on Γ is further projected onto a zero mass flux field by subtracting

$$\frac{\oint_\Gamma \vec{u} \cdot \hat{n} dl}{\oint_\Gamma dl} \tag{5.1}$$

from the normal velocity on Γ, where $\vec{u}$ and $\hat{n}$ are the velocity and outward normal on Γ, and dl is a differential line element. We find that the correction required is indeed statistical and small; no systematic error is detected in the net mass-flux though Γ.

5.2.1 Results

The width of the overlap region $\mathcal{Q} \bigcap \mathcal{D}$ in these calculations is 2.94σ. The size of the molecular-only region was chosen such that the total molecular region $\mathcal{D}$ (molecular-only region plus overlap region) is exactly the same as the molecular calculation domain of section 4.2. The thickness of the overlap region significantly affects the convergence rate, and must be some non-negligible fraction of the extent of $\mathcal{D}$ to ensure rapid convergence. In practice, the overlap region should not be taken too

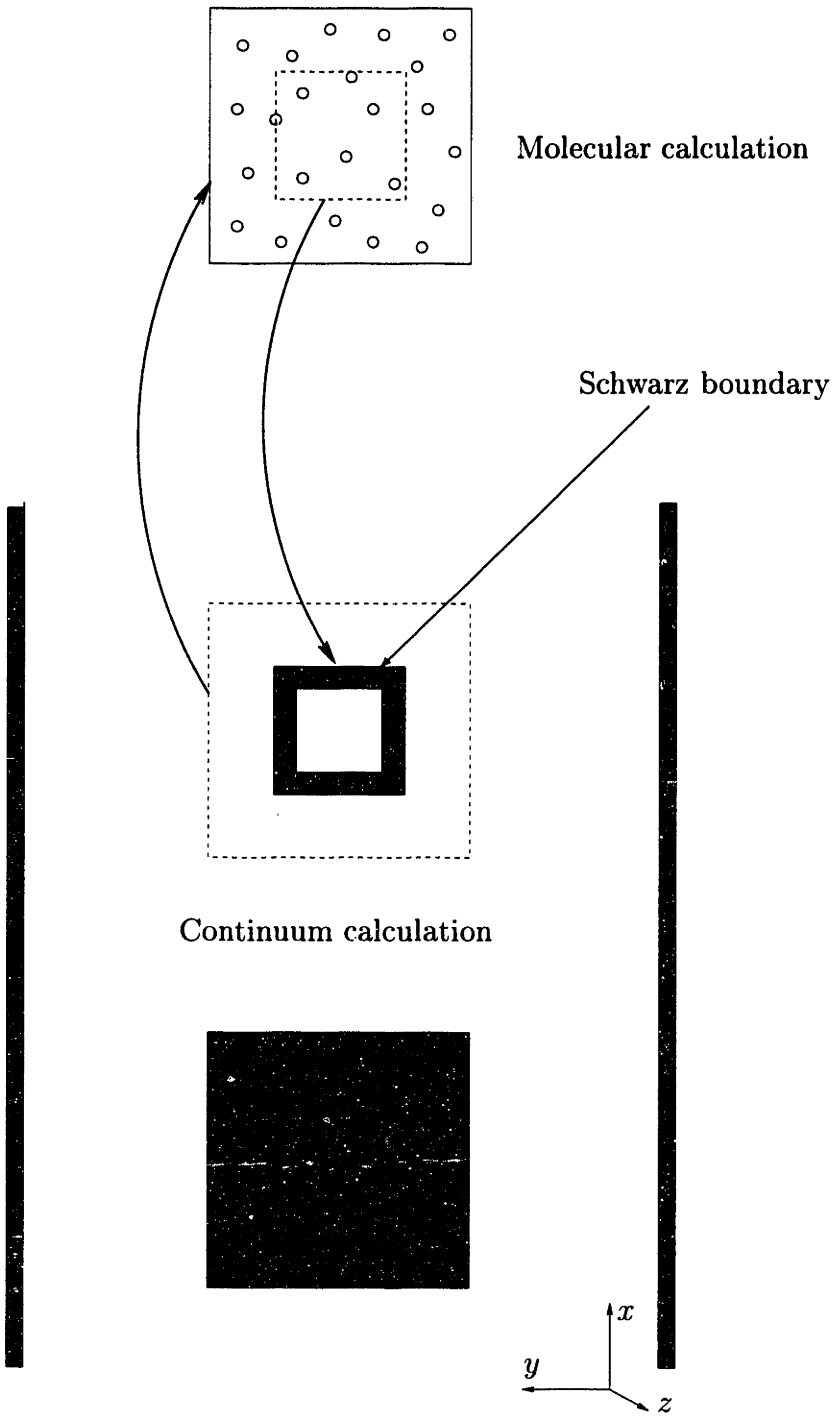

Figure 5-2: Schematic of the Schwarz iteration for the test problem of Fig. 4-2. The Dirichlet boundaries of the continuum calculation are shown in dark; the "internal Schwarz (Dirichlet) boundary" due to the Schwarz method is also indicated.

large, since the number of molecules increases rapidly; for the domain chosen here, there are 245 molecules in $\mathcal{M}$, 980 molecules in all of $\mathcal{D}$, and 3060 molecules in all of $\mathcal{C}$. In real applications, the MD-only region $\mathcal{M}$ will be selected first, with $\mathcal{D}$ (and hence the overlap region), $\mathcal{B}$, and $\mathcal{C}$ then determined by numerical considerations.

The Schwarz iteration is initiated by assuming a zero (mean velocity) solution in $\mathcal{D}$, and hence zero velocity boundary conditions on Γ. Each full iteration requires, on an HP 735 workstation, 5 minutes for the 3500 degree-of-freedom steady spectral element solution and 18 hours for the 3060-atom MD simulation. (For this "experimental study," we choose the interaction potential cut-off, overlap region, particle reservoir $\mathcal{C}$, and number of timesteps very conservatively; more practical choices for these parameters would reduce the MD simulation time to roughly 10 hours/iteration.) Note, however, that one timestep of the 180000-timestep MD simulation requires only 0.5 seconds, and thus a technique that demanded continuum evaluation on the MD-time-scale would be enormously expensive – a 10–year computation. (For such a small imposed timestep, we could consider a less expensive fully explicit compressible continuum simulation, however the computational cost would still be formidable.) Needless to say, even our approach is not yet particularly efficient given the intrinsic profligacy of the MD computations.

Iterative convergence is obtained in approximately 15 iterations (see Fig. 5-5). The accuracy achieved, although acceptable, is reduced with respect to that obtained in section 4.2.3 (see Fig. 4-4, 4-5); we attribute this degradation to the response (amplification in this case) of the Schwarz method to the MD statistical fluctuations, the difference in transport coefficients in the two models, and the error introduced by the MD boundary condition imposition. We do not yet have a complete understanding of this amplification. Further work is clearly required in that direction. Nevertheless, the results indicate that our approach to hybrid representations can, indeed, capture the dynamics of "complex" multidimensional flows, and at a cost which scales as the cost (or $O(10)$ the cost) of the constituent MD computation.

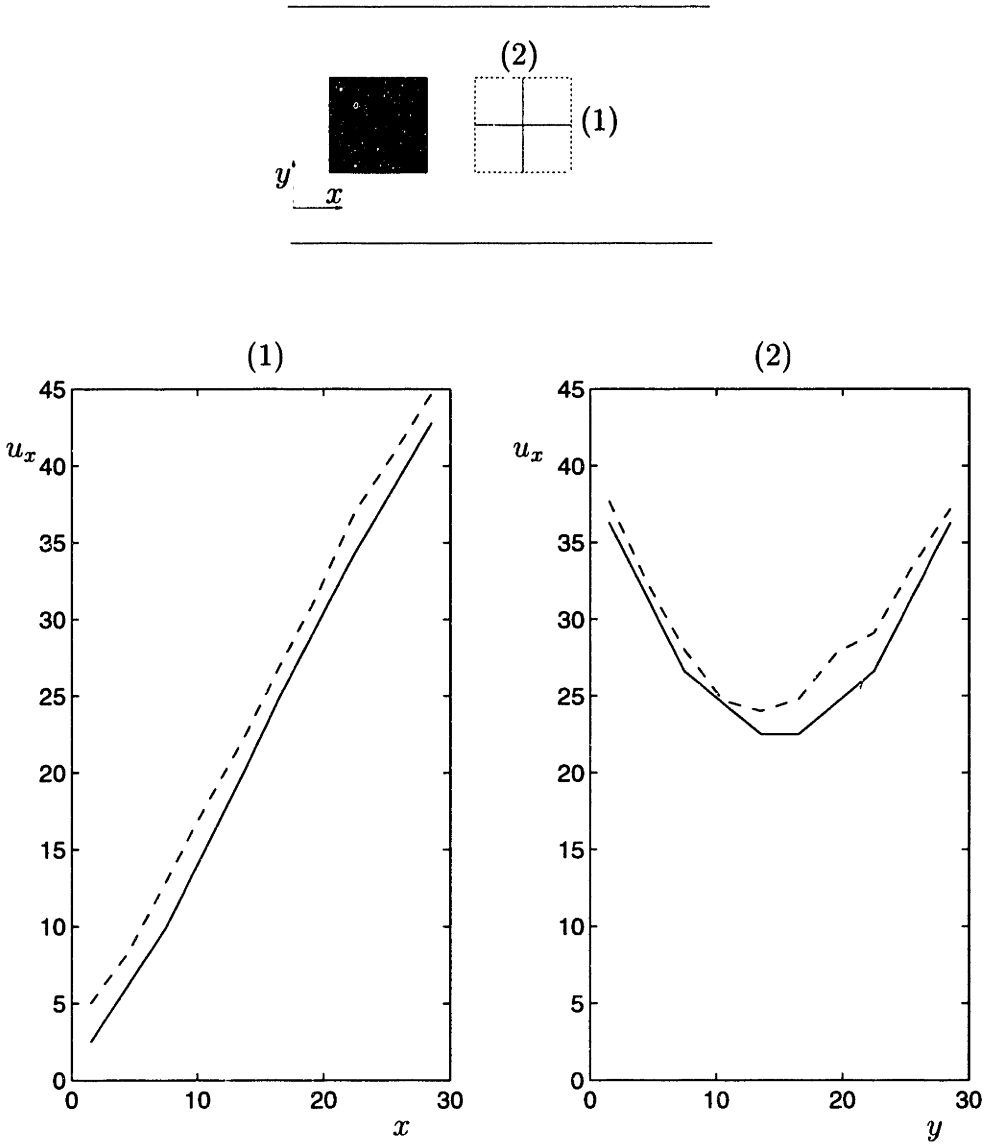

Figure 5-3: Comparison between fully continuum (solid) and hybrid (dashed) Schwarz solutions in the interior of $\mathcal{D}$. The velocities are in m/s and the lengths x, y in Å. The graphs correspond to the constant-y (1) and constant-x (2) slices indicated above.

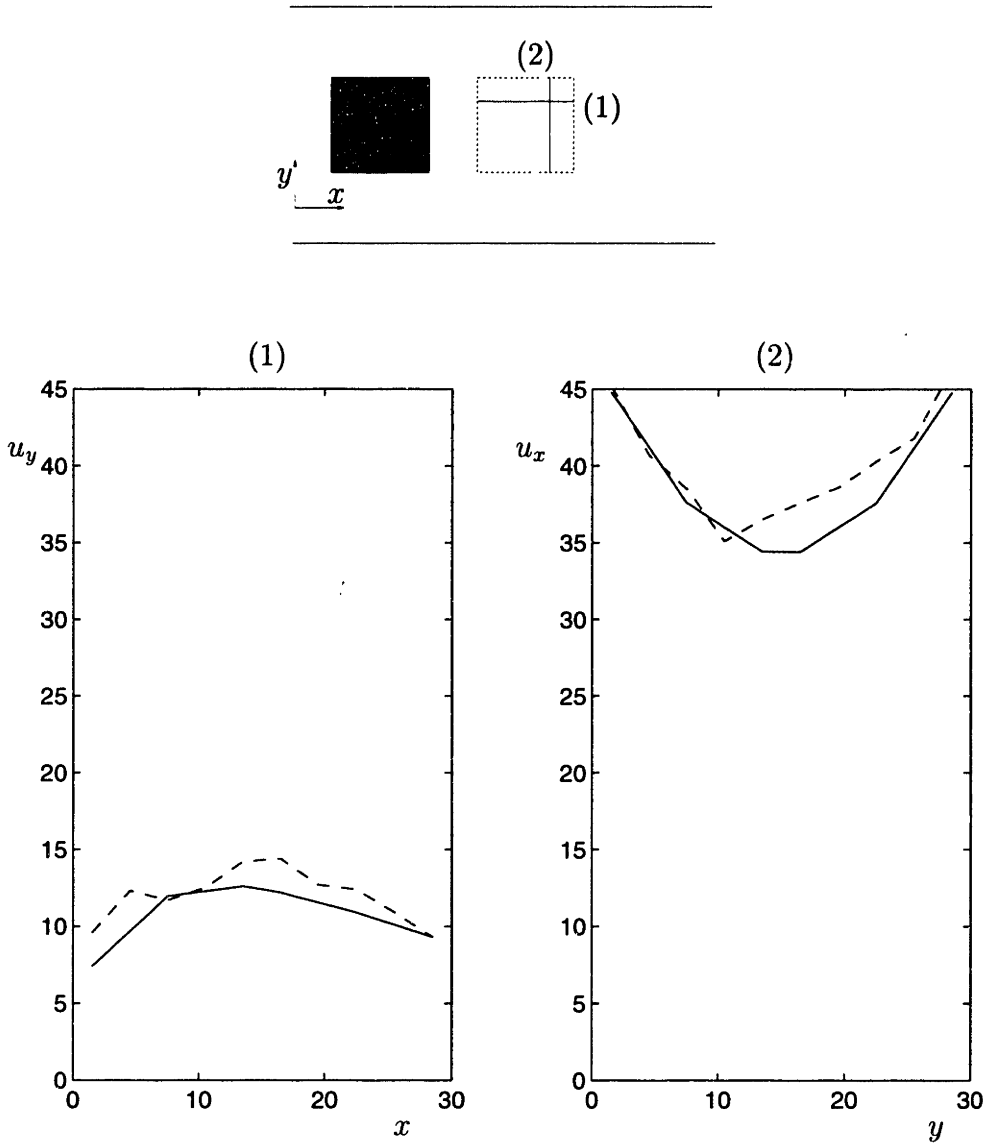

Figure 5-4: Comparison between fully continuum (solid) and hybrid (dashed) Schwarz solutions in the interior of $\mathcal{D}$. The velocities are in m/s and the lengths x, y in Å. The graphs correspond to the constant-y (1) and constant-x (2) slices indicated above.

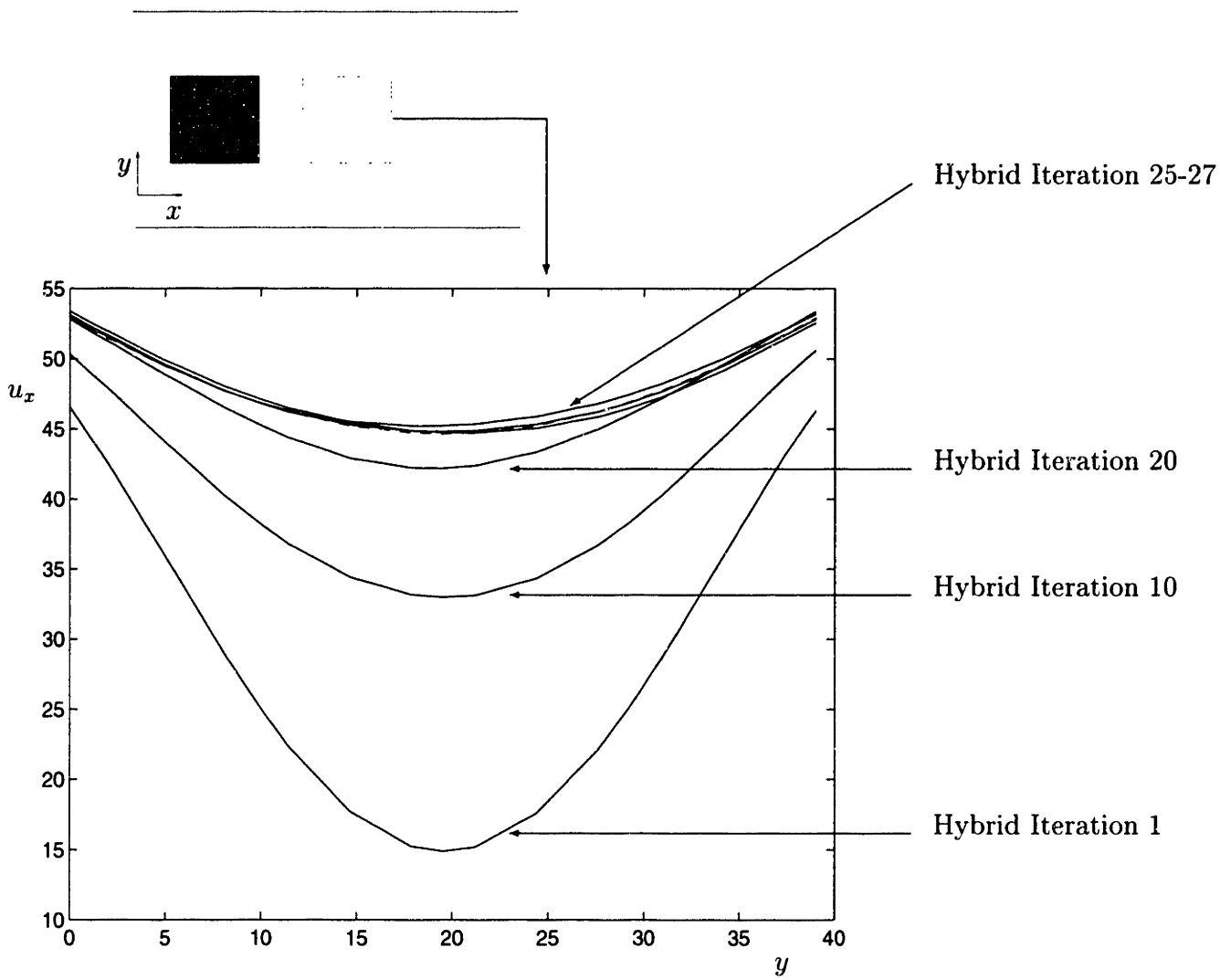

Figure 5-5: Convergence history for the test problem of Fig. 4-2. The exact (continuum) solution is shown dashed.

5.3 Noise Considerations

We have shown that the hybrid framework proposed in chapters 3-5 can successfully be applied to fluid mechanical problems of interest. The test problem we have chosen is sufficiently complex and general to guarantee that the technique is broadly applicable. The only drawback associated with this test problem is the fact that the physical domain is small enough that a fully molecular solution would be computationally manageable or in some cases even preferable. Indeed, for this problem the computational gain was only of the order of 30%; although the ratio of $\mathcal{D}$ to Ω is 1/50, the computational work associated with the MD scales as the size of the full MD simulation ($\mathcal{C}$), which is 2.5 times larger than $\mathcal{D}$, multiplied by the number of iterations (~ 15). Note that the maximum number of iterations in Fig. 5-5 is not the representative number for convergence, since the iteration was frequently perturbed away from its converging path in that particular numerical experiment.

Although hybrid techniques can produce considerable savings in computational cost with respect to fully molecular solutions, the applicability of hybrid techniques is ultimately limited by statistical noise considerations, in a similar fashion to the fully molecular techniques. Because of the relatively small number of sampling timesteps that can be taken in the course of an MD simulation, the noise associated with properties in the sampling bins is of macroscopic magnitude. Adequate resolution requires that the difference between the properties in two adjoining bins be greater than this noise, which effectively requires macroscopic changes over distances of the order of σ and thus huge gradients (see chapter 2). If such gradients prevail in the computational domain, as the latter becomes of macroscopic dimensions the simulated systems soon become unrealistic. For example, if the above test problem was extended to macroscopic size by a 10,000-fold increase in linear dimensions while keeping the same gradients in the flow and hence the same resolution, the Reynolds number would increase by $10,000^3 = 10^{12}$ and the Mach number would have increased by $10,000^2$ (the centerline velocity in Poiseuille flow scales as the square of the channel width); the nature of the problem would be completely changed unless improved resolution

could be afforded. Needless to say that if similarity is not exploited, but rather, direct animation of the system of interest is sought, only very highly non-equilibrium situations correspond to the gradients encountered in a typical MD simulation.

The moving contact line problem is particularly suited to a hybrid solution framework because it is characterized by large gradients which, however, remain localized to the vicinity of the contact point, and hence extension of the far field computational domain to macroscopic dimensions does not generate the problems described above. This problem will be the subject of the remaining chapters of the present thesis.

Chapter 6

A Variationally Consistent Finite Element Approach to the Two-Fluid Internal Contact Line Problem

In chapters 3 to 5 we have developed a general hybrid atomistic-continuum numerical solution technique; the technique has been validated for the case of a single-fluid flow in a two-dimensional channel. The ultimate goal of this work is the treatment of complex thermo-fluid phenomena that require modeling on the microscale. One example is the moving contact line problem; a formidable undertaking both for the numerical modeling but also the theoretical modeling challenges it presents.

In this chapter we present the development of continuum simulation tools for the treatment of the moving contact line problem. In the next chapter we concentrate on the theoretical modeling issues and the treatment of the same problem by molecular techniques that provide valuable insight towards the understanding of contact line behavior in macroscopic terms. Chapters 6 and 7 present the development of tools for the hybrid treatment of the moving contact line problem that is the subject of chapter 8.

6.1 Introduction

Although finite element solutions of steady moving contact line problems first appeared many years ago [29], the complex problem of steady-state interface shape determination is not yet entirely resolved. The source of the numerical difficulties is primarily the nonlinearity of the problem, which arises (even for Stokes flow) due to the coupling between the two-fluid interface geometry and the two-dimensional flowfield.

A common approach to obtaining consistent solutions for both the flowfield and the two-fluid interface is to apply a "segregated" iterative technique: each iteration consists of a flowfield solution for a fixed two-fluid interface, followed by a two-fluid interface adjustment. These techniques take advantage of the fact that, in the steady state, the two-fluid interface obeys both (i) the two-fluid stress continuity condition, and (ii) the kinematic condition, which requires the normal fluid velocity at the interface to vanish. A solution can thus be obtained by relaxing one of these two conditions, and then exploiting the residual of this relaxed condition as the driving force for an improved two-fluid interface geometry.

The exact time-dependent evolution of the two-fluid interface from an arbitrary initial geometry to the steady state is an example of such a procedure. In this case the kinematic condition is relaxed, and the resulting (non-zero) normal velocities on the two-fluid interface then serve to integrate the interface position forward in time. This technique is computationally very inefficient: the timestep must be prohibitively small [19, 5] due to the very small elements required in the vicinity of the contact line.

If the dynamics of equilibration are of no interest, and only the steady state solution is required, much faster iterative techniques can be devised [29, 19]. In particular, in the work of Lowndes [29], flowfield solutions are obtained by relaxing not the kinematic condition, but rather the stress continuity condition; extension of this work to two-fluid systems is reported in [30]. The Lowndes approach, however, is based upon the strong form of the stress continuity equation, and does not, therefore,

constitute a fully consistent finite element treatment of the problem. The latter is not only of interest from a theoretical point of view: variationally consistent schemes are often more accurate, and ultimate extension to three space dimensions is arguably simpler.

Consistency is obtained in Ho & Ronquist [19] by application of the appropriate variational form for the traction boundary condition; the latter is first derived in [36] for the two dimensional case, and subsequently extended in [18] to three dimensions. The residual normal traction supplies the driving force for the motion of the two-fluid interface, just as in [29], but now the variational form of the stress continuity condition is satisfied at equilibrium. The issue of internal contact lines and the resulting pressure indeterminacy is not addressed in [19], however, since the work focuses on free surface flows with no moving contact lines.

The technique presented here may be viewed as a synthesis of the techniques proposed in [29] and [19]: the appropriate surface tension variational form and associated normal traction residual is inspired by [19]; the determination of the pressure drop across the interface is addressed through application of a global force balance equation, as first introduced in [29]. In particular, our focus is on the solvability condition that arises as a result of the internal contact line.

6.2 Physical Problem

We describe here the physical problem of interest, with particular attention to the conditions associated with the two-fluid interface. The full mathematical description is then given in the next section.

We first consider two static immiscible fluids in a two-dimensional channel: the meniscus that separates the two fluids will adopt a shape that balances the capillary stresses with the pressure difference between the two fluids, subject to the contact-angle boundary condition. We next permit the two fluids to move. In particular, we consider the problem in which one fluid displaces the other fluid at a constant interface (average fluid displacement) speed U. The meniscus shape will now further

distort due to the stresses created by the flowing fluid; the interface shape is an unknown, and must be determined with the flowfield by solution of a nonlinear set of coupled partial differential equations. The problems of interest here are limited to the case of small Reynolds number, $Re \equiv \rho U H/\mu \ll 1$, and small Capillary number, $Ca \equiv \mu U/\gamma < 0.1$; here ρ is the density, H is the channel half-width, μ is the dynamic viscosity, and γ is the assumed-constant surface tension coefficient between the two fluids.

Finally, we move to the reference frame of the moving interface, as shown in Fig. 6-1: the interface is now stationary and the walls of the channel move in the $\hat{\mathbf{x}}_2$-direction with velocity $-U$. We can further take advantage of the symmetry of the problem and consider only the domain Ω, which extends from the wall to the centerline of the channel. Assuming that the channel is sufficiently long [5], the inflow and outflow velocity profiles will be fully developed and hence parabolic. In particular, since in the reference frame of the moving contact line the interface does not move, there can be no net fluid displacement; the velocity profiles on Γ_{BC} and Γ_{AD} are thus zero-mass-flux parabolic profiles that satisfy no-slip ($u_2 = -U$) at the moving wall.

As already indicated, the normal velocity on the two-fluid interface Γ_f must be zero in the steady state. Since the velocity component normal to the wall is necessarily zero, the velocity of the fluid on Γ_f is zero in *both* components at the wall (point H). This, however, is in conflict with the usual no-slip boundary condition at the wall, which would require that fluid particles adjacent to the wall move with velocity $-U$ in the $\hat{\mathbf{x}}_2$-direction. This discrepancy is, of course, the source of the intransigence of the moving contact line problem. In order to relieve this boundary condition incompatibility, and the resulting shear-stress singularity, a slip boundary condition is employed: the fluid velocity at the wall is zero at the contact point (full slip), and smoothly relaxes to $-U$ away from the contact point. The characteristic distance for the decay, l, will be denoted the slip length.

In our simulations we permit slip through two different approaches. In the first

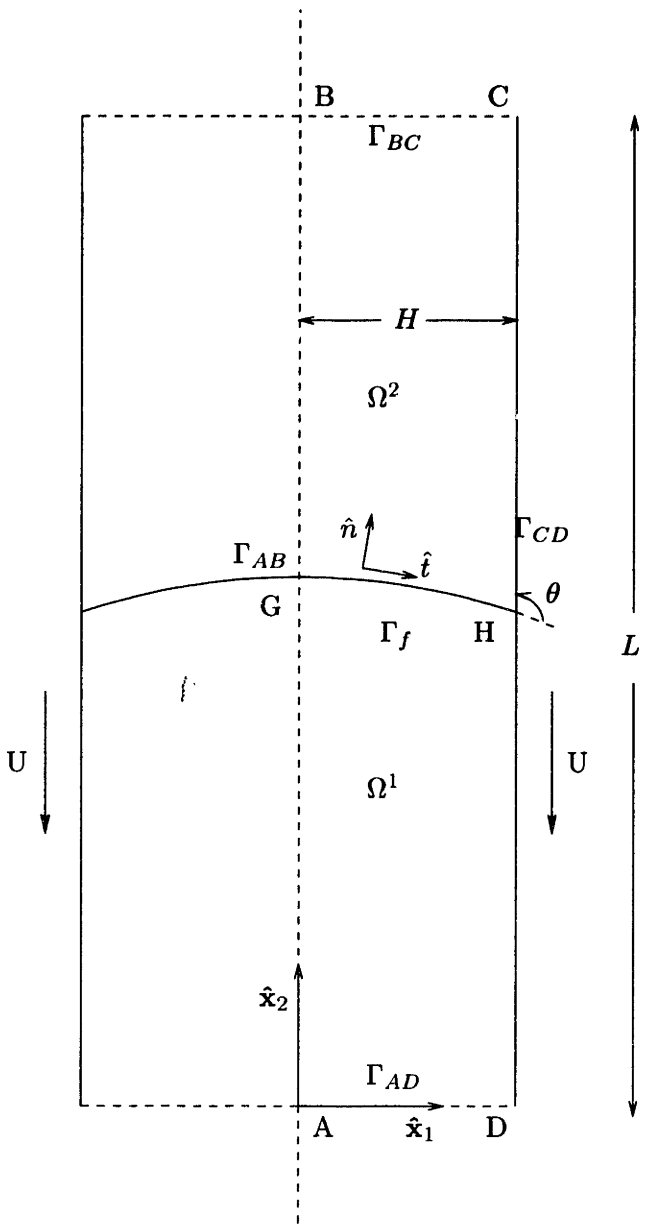

Figure 6-1: Problem geometry: the domain of interest is $\Omega = \Omega^1 \bigcup \Omega^2$.

approach, we apply the well-known (but admittedly *ad hoc*) Navier condition

$$\sigma_{21} = -\frac{\mu}{l}(U + u_2) \text{ on } \Gamma_{CD} \tag{6.1}$$

where $u = (u_1, u_2)$ is the fluid velocity and σ_{ij} is the stress tensor. In the second approach, we specify the slip profile, $u_2(x_1 = H, x_2) = \mathcal{U}(x_2)$, as dictated (say) by an MD calculation [15]. In most of this presentation we shall focus on the Navier condition; at the conclusion we indicate the necessary changes for the specified-velocity approach.

Finally, the contact angle must be specified. The contact angle, θ, is defined as the angle between the bounding wall, Γ_{CD}, and the tangent of Γ_f at the wall, as shown in Fig. 6-1. (The symmetry plane introduces another "artificial" contact angle (at G) which must be 90^o.) Note that the dynamic contact angle θ is not a thermodynamic property, and its specification can, thus, be problematic.

6.3 Variational Formulation

We first give the strong form of the equations. The equations governing the fluid flow are the steady incompressible Stokes equations,

$$\frac{\partial \sigma_{ij}}{\partial x_j} = 0 \text{ in } \Omega, \tag{6.2}$$

$$\frac{\partial u_i}{\partial x_i} = 0 \text{ in } \Omega, \tag{6.3}$$

where

$$\sigma_{ij} = \mu(\frac{\partial u_i}{\partial x_j} + \frac{\partial u_j}{\partial x_i}) - p\delta_{ij} \tag{6.4}$$

is the stress tensor. Here p is the pressure, and δ_{ij} is the Kronecker-delta symbol. We adopt the Einstein summation convention, and further assume that all unrepeated indices range from 1 to 2. We neglect gravity forces, though these can, of course, be readily included.

The boundary conditions are then given by

$$\hat{n}_i(\sigma_{ij}|_{\Gamma_f^2} - \sigma_{ij}|_{\Gamma_f^1})\hat{n}_j = \gamma\kappa \text{ on } \Gamma_f, \tag{6.5}$$

$$\hat{t}_i(\sigma_{ij}|_{\Gamma_f^2} - \sigma_{ij}|_{\Gamma_f^1})\hat{n}_j = 0 \text{ on } \Gamma_f, \tag{6.6}$$

$$\frac{dy_s(0)}{ds} = 0, \tag{6.7}$$

$$\frac{dy_s(H)}{ds} = cos\theta, \tag{6.8}$$

and

$$u_1 = 0 \text{ on } \Gamma, \tag{6.9}$$

$$u_2 = Ug, \text{ on } \Gamma_{AD}, \Gamma_{BC}, \tag{6.10}$$

and

$$\sigma_{21} = 0 \text{ on } \Gamma_{AB}, \tag{6.11}$$

$$\sigma_{21} = -\frac{\mu}{l}(U + u_2) \text{ on } \Gamma_{CD}. \tag{6.12}$$

Here $\hat{n}$ and $\hat{t}$ are the right-handed outward unit normal and tangent on Γ_f; Γ_f^2 and Γ_f^1 refer to the limits as we approach Γ_f from Ω^2 and Ω^1, respectively; κ is the curvature; s is the arc length coordinate along Γ_f such that $s = 0$ and $s = S$ correspond to points G and H on Γ_f, respectively; Γ is the union of $\Gamma_{AB}, \Gamma_{BC}, \Gamma_{CD}$, and Γ_{DA}; $y_s(x_1)$ is the two-fluid interface position as a function of x_1; and g is the parabolic zero-mass-flux profile, $g(\frac{x_1}{H}) = \frac{1}{2} - \frac{3}{2}(\frac{x_1}{H})^2$. In what follows, we shall refer only to the non-dimensional form of the governing equations, in which we identify $H = 1$, $U = 1$, $\mu = 1$, $\gamma = Ca^{-1}$, and $l = \varepsilon$.

We now turn to the variational formulation. First, it is convenient to introduce the function spaces $L^2(\Omega), \mathcal{H}^1(\Omega), L_0^2(\Omega), \mathcal{H}_D^1(\Omega), \mathcal{H}_0^1(\Omega)$, $\mathcal{H}_{\Gamma_f}^1(\Omega)$, and $\mathcal{H}_{\Gamma_f 0}^1(\Omega)$. As usual [2], $L^2(\Omega)$ is the space of functions which are square integrable over Ω, and $\mathcal{H}^1$ is the space of functions v such that $v \in L^2(\Omega)$ and $\frac{\partial v}{\partial x_i} \in L^2(\Omega)$. Then

$$L_0^2(\Omega) = \{q \in L^2(\Omega) | \int_{\Omega^1} q dA = 0, \int_{\Omega^2} q dA = 0\}, \tag{6.13}$$

$$\mathcal{H}_D^1(\Omega) = \{v_i \in \mathcal{H}^1(\Omega), i = 1, 2 \mid v|_{\Gamma_{AD}} = v|_{\Gamma_{BC}} = (0, g),$$

$$v_1|_{\Gamma_{AB}} = v_1|_{\Gamma_{CD}} = 0\}, \tag{6.14}$$

$$\begin{aligned}\mathcal{H}_0^1(\Omega) &= \{v_i \in \mathcal{H}^1(\Omega), i = 1,2 \mid v|_{\Gamma_{AD}} = v|_{\Gamma_{BC}} = 0, \\ &\qquad v_1|_{\Gamma_{AB}} = v_1|_{\Gamma_{CD}} = 0\},\end{aligned} \tag{6.15}$$

$$\begin{aligned}\hat{\mathcal{H}}_{\Gamma_f}^1(\Omega) &= \{v_i \in \mathcal{H}^1(\Omega), i = 1,2 \mid v|_{\Gamma_{AD}} = v|_{\Gamma_{BC}} = (0,g), \\ &\qquad v_i\hat{n}_i|_{\Gamma_f} = 0, v_1|_{\Gamma_{AB}} = v_1|_{\Gamma_{CD}} = 0\},\end{aligned} \tag{6.16}$$

$$\begin{aligned}\hat{\mathcal{H}}_{\Gamma_f 0}^1(\Omega) &= \{v_i \in \mathcal{H}^1(\Omega), i = 1,2 \mid v|_{\Gamma_{AD}} = v|_{\Gamma_{BC}} = 0, \\ &\qquad v_i\hat{n}_i|_{\Gamma_f} = 0, v_1|_{\Gamma_{AB}} = v_1|_{\Gamma_{CD}} = 0\}.\end{aligned} \tag{6.17}$$

Note that $\mathcal{H}_D^1, \mathcal{H}_0^1, \hat{\mathcal{H}}_{\Gamma_f}^1, \hat{\mathcal{H}}_{\Gamma_f 0}^1$ are all product spaces; note also that in $\hat{\mathcal{H}}_{\Gamma_f}^1$ and $\hat{\mathcal{H}}_{\Gamma_f 0}^1$ the tangential component of v is free to vary on Γ_f. Finally, $\mathcal{H}^1(\Gamma_f)$ is the space of scalar functions y for which y and $\frac{dy}{ds}$ are square integrable over Γ_f.

We next introduce the bilinear forms

$$a(v,w) = \int_\Omega \frac{\partial v_i}{\partial x_j}(\frac{\partial w_i}{\partial x_j} + \frac{\partial w_j}{\partial x_i})dA + \frac{1}{\varepsilon}\int_{\Gamma_{CD}} v_2 w_2 ds, \tag{6.18}$$

$$b(v,q) = -\int_\Omega \frac{\partial v_i}{\partial x_i} q dA, \tag{6.19}$$

and

$$b_2(v,q) = -\int_{\Omega^2} \frac{\partial v_i}{\partial x_i} q dA \ . \tag{6.20}$$

Here $a(\cdot,\cdot)$ is defined and continuous over $\mathcal{H}_D^1, \mathcal{H}_0^1, \hat{\mathcal{H}}_{\Gamma_f}^1$, and $\hat{\mathcal{H}}_{\Gamma_f 0}^1$; similarly, $b(\cdot,\cdot)$ is defined and continuous over $X \times L^2(\Omega)$, for $X = \mathcal{H}_D^1, \mathcal{H}_0^1, \hat{\mathcal{H}}_{\Gamma_f}^1$, and $\hat{\mathcal{H}}_{\Gamma_f 0}^1$. Note that $b(v,q) = 0, \forall v \in \hat{\mathcal{H}}_{\Gamma_f 0}^1$, for q constant in Ω^1 and zero in Ω^2 *and* q constant in Ω^2 and zero in Ω^1; there are two spurious modes when the normal velocity on Γ_f is required to vanish.

We shall also need several linear forms. First,

$$\ell^U(v) = -\frac{1}{\varepsilon}\int_{\Gamma_{CD}} v_2 ds, \tag{6.21}$$

is required for the Navier condition. Second, and more importantly,

$$\ell^\Gamma(v; y_s) = -Ca^{-1}\int_{\Gamma_f} \frac{dv_2}{ds}\frac{dy_s}{ds}\, ds + Ca^{-1} v_2(1) cos\theta \tag{6.22}$$

shall represent the surface tension terms. More properly we should replace the integral in (6.22) with a duality pairing; also, y may need to be slightly more regular than $\mathcal{H}^1(\Gamma_f)$ for the problem to be well posed.

We now look for a velocity u in $\mathcal{H}^1_D(\Omega)$, and a pressure $p = \tilde{p} + \pi, \tilde{p}$ in $L^2_0(\Omega), \pi$ in $\mathbf{R}$, where the latter decomposition permits a pressure level difference between the two fluids. The interface shape y_s is sought in $\mathcal{H}^1(\Gamma_f)$. These unknowns must satisfy

$$a(u, v) + b(v, \tilde{p}) + b_2(v, \pi) = \ell^\Gamma(v; y_s) + \ell^U(v), \quad \forall v \in \mathcal{H}^1_0(\Omega), \tag{6.23}$$

$$b(u, q) = 0, \quad \forall q \in L^2_0(\Omega), \tag{6.24}$$

and

$$u_i \hat{n}_i = 0 \ \text{ on } \ \Gamma_f. \tag{6.25}$$

We can see that equations (6.2) and (6.3) follow from (6.23) and (6.24) by taking v to be nonzero in Ω, while equations (6.11), (6.12) follow by taking v_2 nonzero on Γ_{AB} and Γ_{CD}. The tangential stress continuity equation (6.6) is enforced by variations in the $\hat{t}$-direction on Γ_f; although $u_i \hat{n}_i = 0$ from (6.25), $v_i \hat{n}_i = 0$ is not constrained in (6.23), and hence the normal stress continuity equation (6.5) is also naturally imposed.

Alternatively, we can introduce the following formulation, which makes some of the solvability issues more transparent, and will also be the starting point for the derivation of our two-fluid interface iterative procedure. In this case we look for:

$(u, \tilde{p}, \pi, y_s)$ in $(\mathcal{H}^1_{\Gamma_f}(\Omega) \times L^2_0(\Omega_1) \times \mathbf{R} \times \mathcal{H}^1(\Gamma_f))$ such that

$$a(u,v) + b(v,\tilde{p}) + b_2(v,\pi) = \ell^U(v), \quad \forall v \in \hat{\mathcal{H}}^1_{\Gamma_f 0}(\Omega) \tag{6.26}$$

$$b(u,q) = 0, \quad \forall q \in L^2_0(\Omega) \tag{6.27}$$

and

$$\ell^\gamma(v; y_s) = a(u,v) + b(v,\tilde{p}) + b_2(v,\pi) - \ell^U(v), \quad \forall v \in \mathcal{H}^1_0(\Omega). \tag{6.28}$$

In this formulation, $u_i \hat{n}_i = 0$ of equation (6.25) is actually imposed by the appropriate choice of space, $\hat{\mathcal{H}}^1_{\Gamma_f}(\Omega)$. However, since $v_i \hat{n}_i = 0$ for v in $\hat{\mathcal{H}}^1_{\Gamma_f 0}(\Omega)$, (6.26) only imposes the tangential stress condition, not the normal stress continuity equation (6.5); the latter condition is now enforced by (6.28).

Equations (6.22) and (6.23) involve the x_2 component of the normal stress continuity equation (6.5). It can be shown that, if this condition is satisfied, then the complete variational-weak formulation of (6.5) is also satisfied,

$$a(u,v) + b(v,\tilde{p}) + b_2(v,\pi) - \ell^U(v) = \Lambda^\gamma(v; x_s) \ \ \forall v \in \mathcal{H}^1_0(\Omega), \tag{6.29}$$

where

$$\Lambda^\gamma(v; x_s) = -Ca^{-1} \int_{\Gamma_f} \frac{dv_i}{ds} \frac{dx_{si}}{ds} \, ds + Ca^{-1} v_2(1) cos\theta, \tag{6.30}$$

and $x_s = (x_{s1}, x_{s2}) = (x_{s1}, y_s)$ are the coordinates of the two-fluid interface Γ_f [36]. To show this, we first note that we can express any v as $v_1 \hat{\mathbf{x}}_1 + v_2 \hat{\mathbf{x}}_2$, and that, thanks to (6.28), the $v_2 \hat{\mathbf{x}}_2$ contribution to (6.29) clearly vanishes. We next note that if $\hat{t}_1$ is always non-zero, then $v_1 \hat{\mathbf{x}}_1$ may be expressed as $\Psi + \Phi$, where $\Psi|_{\Gamma_f} = v_1 \hat{t}/\hat{t}_1$ and $\Phi|_{\Gamma_f} = -v_1 \hat{t}_2/\hat{t}_1 \hat{\mathbf{x}}_2$. These contributions to (6.29) also vanish – the former due to (6.26) and the latter due to (6.28) – and the result is thus proven. Cases in which $\hat{t}_1$ may vanish, for example fully wetting configurations, are beyond the scope of the current investigation.

We know, on physical grounds, that the pressure level is indeterminate. However,

as already discussed, $b(v,q)$ has *two* spurious modes for $v \in \hat{\mathcal{H}}^1_{\Gamma_f 0}(\Omega)$, and hence to render $\tilde{p}$ unique in (6.26) $L^2_0(\Omega)$ requires zero average in both domains, which is clearly overconstrained. To rectify the situation we have introduced the scalar π, which must be determined by a global force balance. In fact, this global force balance represents the (left nullspace) solvability condition associated with the indeterminacy (right nullspace) of the (say) average position of the free surface.

In particular, it is clear from (6.28) and (6.22) that the solution is translationally invariant: we may add any constant to y_s with impunity. From the "left" side we notice that the surface Laplacian is annihilated by any function in $\mathcal{H}^1_0(\Omega)$ such that $v_2 = 1$ on Γ_f. The associated solvability condition – our equation for π – is given by

$$Ca^{-1}cos\theta = \{a(u,v) + b(v,\tilde{p}) + b_2(v,\pi) - \ell^U(v)\}, \quad \forall v \in \{\mathcal{H}^1_0(\Omega) |\ v_2|_{\Gamma_f} = 1\}, \quad (6.31)$$

which is just the variational form of the normal force balance on Γ_f,

$$Ca^{-1}cos\theta = \int_0^S (\sigma_{2j}|_{\Gamma_f^2} - \sigma_{2j}|_{\Gamma_f^1})\hat{n}_j ds = (\int_0^1 \hat{n}_i(\sigma_{ij}|_{\Gamma_f^2} - \sigma_{ij}|_{\Gamma_f^1})\hat{n}_j dx_1), \quad (6.32)$$

as derived in [1]. Recall that θ is the imposed dynamic contact angle. Note that, because u is in equilibrium from (6.26), π is insensitive to the particular lifting of v chosen in (6.31); numerical convenience will suggest an obvious candidate, as we discuss in section 6.5.

6.4 Discrete Equations

We first introduce the finite element approximation (u_{hi}, p_h) to (u_i, p) over a suitable triangulation $\mathcal{T}_h$ of Ω such that

$$\overline{\Omega} = \bigcup_k \overline{T}^k_h,$$

where the T^k_h are the triangular elements. The variable geometry requirements neccesitates the application of an isoparametric formulation in which the midpoints of the sides of elements for which the endpoints lie on Γ are displaced so as to also lie

on Γ. The resulting isoparametric mapping F^k from the reference element $\hat{T}$ to T_h^k, depicted in Fig. 6-2, takes the form

$$(x_1(\boldsymbol{\xi}), x_2(\boldsymbol{\xi})) = \sum_{i=1}^{6} (x_1, x_2)_i \, h_i(\boldsymbol{\xi}), \tag{6.33}$$

where the h_i are the usual quadratic reference-element shape functions, $(x_1, x_2)_i$ are the coordinates of the six elemental boundary nodes, and $\boldsymbol{\xi}$ is the vector of reference element (barycentric) co-ordinates $(\xi_1, \xi_2, 1 - \xi_1 - \xi_2)$. The Jacobian of the transformation is a quadratic function of $\boldsymbol{\xi}$.

In order to simplify our task, we shall require that nodes on Γ_f are equispaced in the $\hat{\mathbf{x}}_1$-direction, and that the x_1 location of these nodes is fixed during the iterative process to be discussed in section 6.5. This implies that x_1 on Γ_f in element $\overline{T}_h^k$ is a linear function of (say) ξ_1, $F_{x_1}^k(\xi_1)$, and hence the inverse edge mapping $\xi_1 = G^k(x_1)$ exists and is also linear. We deduce that

$$y_s = F_{x_2}^k(\xi_1) = F_{x_2}^k \circ G^k(x_1) \tag{6.34}$$

is piecewise quadratic in x_1, and thus $y_s \in Y_s \equiv \{y|_{\mathcal{D}_k} \in \mathbf{P}_2(\mathcal{D}^k), \forall \mathcal{D}^k \in \Gamma_{\mathcal{D}}\} \bigcap \mathcal{H}^1(\Gamma_f)$, where $\mathcal{D}^k$ is the projection of T_h^k onto the x_1 axis, $\mathbf{P}_q(\mathcal{D}^k)$ is the space of q^{th} order polynomials over $\mathcal{D}^k$, and $\overline{\Gamma}_{\mathcal{D}} = \bigcup_k \overline{\mathcal{D}}^k$.

The complete statement of the discrete problem is then: find $(u_h, \tilde{p}_h, \pi_h, y_{sh}) \in (X_h, Y_h, \mathbf{R}, Y_s)$ such that

$$a_h(u_h, v) + b_h(v, \tilde{p}_h) + b_{2h}(v, \pi_h) = \ell^U(v), \quad \forall v \in W_{h\,\Gamma_f 0}(\Omega), \tag{6.35}$$

$$b_h(u_h, q) = 0, \quad \forall q \in Y_h, \tag{6.36}$$

and

$$\ell^\Gamma(v; y_{sh}) = a_h(u_h, v) + b_h(v, \tilde{p}_h) + b_{2h}(v, \pi_h) - \ell^U(v), \quad \forall v \in W_{h0}, \tag{6.37}$$

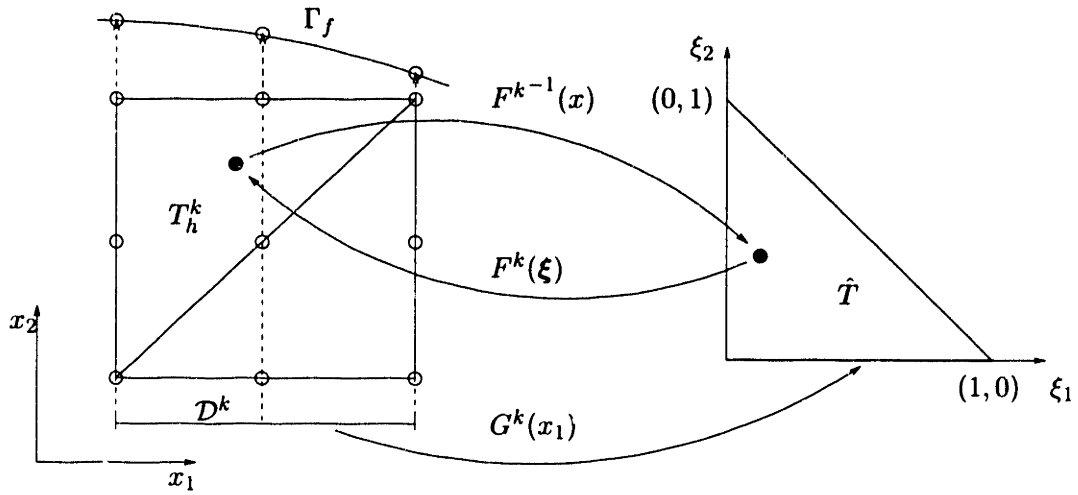

Figure 6-2: Elemental mappings.

where

$$X_h = \{v|_{T_h} = v \circ F^{k-1}, v \in \mathbf{P}_2^+(\hat{T}), \forall T_h \in \mathcal{T}_h\} \bigcap \mathcal{H}^1_{\Gamma_f}(\Omega), \tag{6.38}$$

$$Y_h = \{q|_{T_h} = q \circ F^{k-1}, q \in \mathbf{P}_1(\hat{T}), \forall T_h \in \mathcal{T}_h\} \bigcap L^2_0(\Omega)\}, \tag{6.39}$$

$$W_{h\,\Gamma_f 0} = \{v|_{T_h} = v \circ F^{k-1}, v \in \mathbf{P}_2^+(\hat{T}), \forall T_h \in \mathcal{T}_h\} \bigcap \mathcal{H}^1_{\Gamma_f 0}(\Omega), \tag{6.40}$$

$$W_{h0} = \{v|_{T_h} = v \circ F^{k-1}, v \in \mathbf{P}_2^+(\hat{T}), \forall T_h \in \mathcal{T}_h\} \bigcap \mathcal{H}^1_0(\Omega), \tag{6.41}$$

and

$$\mathbf{P}_2^+(\hat{T}) = \{\mathbf{P}_2(\hat{T}) + \alpha_{T_h}\xi_1\xi_2\xi_3, \alpha_{T_h} \in \mathbf{R}\} \tag{6.42}$$

is the space of quadratic polynomials enhanced by a cubic bubble function. (Note that the π_h term in (6.35) does not in fact contribute.)

This particular choice of the Crouzeix-Raviart element [33] is very well suited for two-fluid interface problems: pressure continuity is not enforced across elemental boundaries, thus enabling the solution to correctly capture the surface-tension-induced pressure discontinuity across the two-fluid interface. (We recall the cubic

bubble function is added to sufficiently enrich the velocity degrees-of-freedom so that these elements, which have substantially more pressure degrees-of-freedom than the continuous pressure Taylor-Hood elements, still satisfy the *inf sup* condition [33].) The subscript h on the linear and bilinear forms indicates the approximation introduced by the isoparametric representation of the problem geometry, and the resulting application of quadrature rules [24] for the evaluation of the elemental integrals. In this work, a seven-point quadrature rule is used.

6.5 Iterative Interface Procedure

Equation (6.37) is the point of departure for the derivation of the variational form for the iterative interface procedure. We exploit the fact that the two sides of equation (6.37) will not balance unless the steady-state solution has been achieved; we can thus use the residual of (6.37) as a force to drive the interface shape towards the steady-state solution. More specifically, we write $y_s = y_s + \Delta y$, and thereby obtain a Laplacian operator for the "correction" displacement Δy

$$-\int_0^S \frac{\partial v_2}{\partial s}\frac{\partial \Delta y_{sh}}{\partial s}ds = \int_0^S \frac{\partial v_2}{\partial s}\frac{\partial y_{sh}}{\partial s}ds - v_2(1)\,cos\theta - Ca(a_h(u_h,v) + b_h(v,\tilde{p}_h) + b_{2h}(v,\pi_h) - \ell^U(v)),\quad \forall v \in W_{h0}(\Omega). \tag{6.43}$$

When the iteration has converged, $\Delta y = 0$, and the above equation reduces to equation (6.37) which must be satisfied in the steady state.

Note that although two Neumann boundary conditions – two angles, one the contact angle, the other the symmetry condition – can be specified for this problem, this would result in an ill-posed problem, since the absolute level of y_s would be allowed to "float"; this reflects the invariance of equation (6.37) under an arbitrary displacement in the $\hat{\mathbf{x}}_2$-direction as discussed in section 6.3. To ensure uniqueness only the symmetry Neumann condition is used along with a *Dirichlet* boundary condition of zero displacement at some other location (in particular, the wall), which thus specifies the two-fluid interface displacement level. Solvability is ensured by correct

choice of π per equation (6.31).

The complete solution algorithm then consists of the following steps:

1. Solve the discrete Stokes equations (6.35), (6.36) for $u_h, \tilde{p}_h$ for some given initial geometry y_s^0.

2. Solve

$$b_{2h}(v, \pi_h) = Ca^{-1} cos\theta - \{a_h(u_h, v) + b_h(v, \tilde{p}_h) - \ell^U(v)\} \tag{6.44}$$

to find π_h. The numerical value of $\{a_h(u_h, v) + b_h(v, \tilde{p}_h)\}$ is simply the sum of the stress "residuals" on Γ_f, that is, the sum of the entries corresponding to the $\hat{\mathbf{x}}_2$-direction velocity nodes lying on Γ_f of the vector that results from multiplying the stiffness matrix with the solution obtained in step (1). The set of coefficients $b_{2h}(v, \pi_h)$ can be easily obtained by multiplying the stiffness matrix by a vector whose non-zero entries are unity at all pressure nodes on *one* side of Γ_f. Note that these evaluations correspond to the choice $v \in \{W_{h0}(\Omega) | \, v_2|_{\Gamma_f} = 1\}$ in which $v_1 = 0$ and v_2 is the sum of all the nodal basis functions associated with Γ_f.

3. Apply

$$-\int_0^S \frac{\partial v_2}{\partial s} \frac{\partial \Delta y_{sh}}{\partial s} ds = \int_0^S \frac{\partial v_2}{\partial s} \frac{\partial y_{sh}}{\partial s} ds - v_2(1)\, cos\theta - Ca(a_h(u_h, v) + b_h(v, \tilde{p}_h) + b_{2h}(v, \pi_h) - \ell^U(v)), \quad \forall v \in W_{h0}(\Omega) \tag{6.45}$$

to calculate the "corrected" interface shape.

4. Repeat the procedure to convergence.

For low Ca the method converges quite rapidly, as we discuss below.

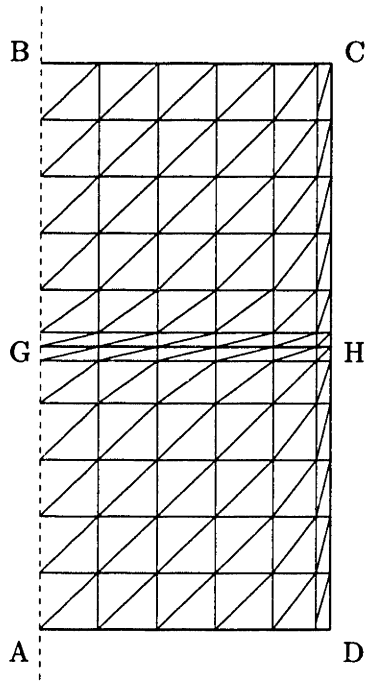

Figure 6-3: A 6×12 finite element grid.

6.6 Numerical Results

6.6.1 Triangulations

We next describe the meshes that we shall use in the examples, although our scheme is in no way limited to any particular triangulation strategy. For simplicity, we shall consider structured meshes, in particular structured meshes in which the degrees-of-freedom are concentrated near the contact line. These resulting meshes do not satisfy the shape regularity condition as $h \to 0$ [34], however for the h studied here we do not believe that the error is adversely affected by this transgression. In particular, we obtain similar results for (much more expensive) uniform and regular structured meshes. Future work will also consider unstructured meshes, which are clearly the best choice, and will permit us to perform more conclusive spatial convergence studies; our focus here, however, is on the finite element formulation.

It has been suggested [29] that, for the complete resolution of the slip phenomenon, the element size close to the contact line must be much smaller than l, the slip length,

due to the weak (logarithmic) singularity in the velocity gradient and pressure as the contact line is approached. We satisfy this requirement with a mesh that is fairly coarse away from the interface and wall, but rather fine in the vicinity of Γ_f and Γ_{CD}. More specifically, we begin with a "background" grid of 5×10 element pairs in the $\hat{\mathbf{x}}_1$ and $\hat{\mathbf{x}}_2$ direction, respectively. Further refinement in the $\hat{\mathbf{x}}_1$-direction is subsequently achieved by splitting the last element (close to the wall) in a 3:1 ratio. The refinement in the $\hat{\mathbf{x}}_2$-direction is obtained by applying an analogous procedure to the layer of two elements enclosing the two-fluid interface. For example, a 8×18 mesh specification implies that the element closest to the wall in the $\hat{\mathbf{x}}_1$-direction has been successively divided in a 3:1 ratio 3 times, yielding a smallest element (the elements closest to the wall) with an edge size of $0.2 \cdot (0.25)^3 = 3.125 \times 10^{-3}$; similarly the smallest element edge size in the $\hat{\mathbf{x}}_2$-direction (the elements closest to Γ_f) is $0.5 \cdot 0.2 \cdot (0.25)^4 = 3.906 \times 10^{-4}$.

Fig. 6-3 demonstrates the "background" grid and the first level of refinement, a 6×12 grid; in the case illustrated in Fig. 6-3 Γ_f is flat. When Γ_f is curved, a linear stretching in $\hat{\mathbf{x}}_2$ is applied as a function of the element distance from Γ_f, with the dilation reducing to zero on Γ_{AD} and Γ_{BC}; this ensures compatibility between the problem geometry and the finite element mesh. The advantage of this mesh is that very fine elements are produced near the contact line H, with a relatively small total number of elements. The main disadvantage, as already indicated, is that the angles in elements close to G, C, and D are not bounded away from zero as we increase the number of elements indefinitely [34].

6.6.2 Numerical Examples

The length of the channel is chosen to extend 3 channel heights in each direction ($L = 6$) so that the assumption of fully developed flow at inflow and outflow is justified [5]. In all cases presented here we set $\varepsilon = 0.01$, $\theta = 100^o$, and consider a 10×24 mesh; only Ca is varied. Fig. 6-4 shows the converged solution for $Ca = 0.02$. To our knowledge, this is the first study of the dynamics of contact line motion in a two-dimensional channel, and thus no numerical or experimental results are available for

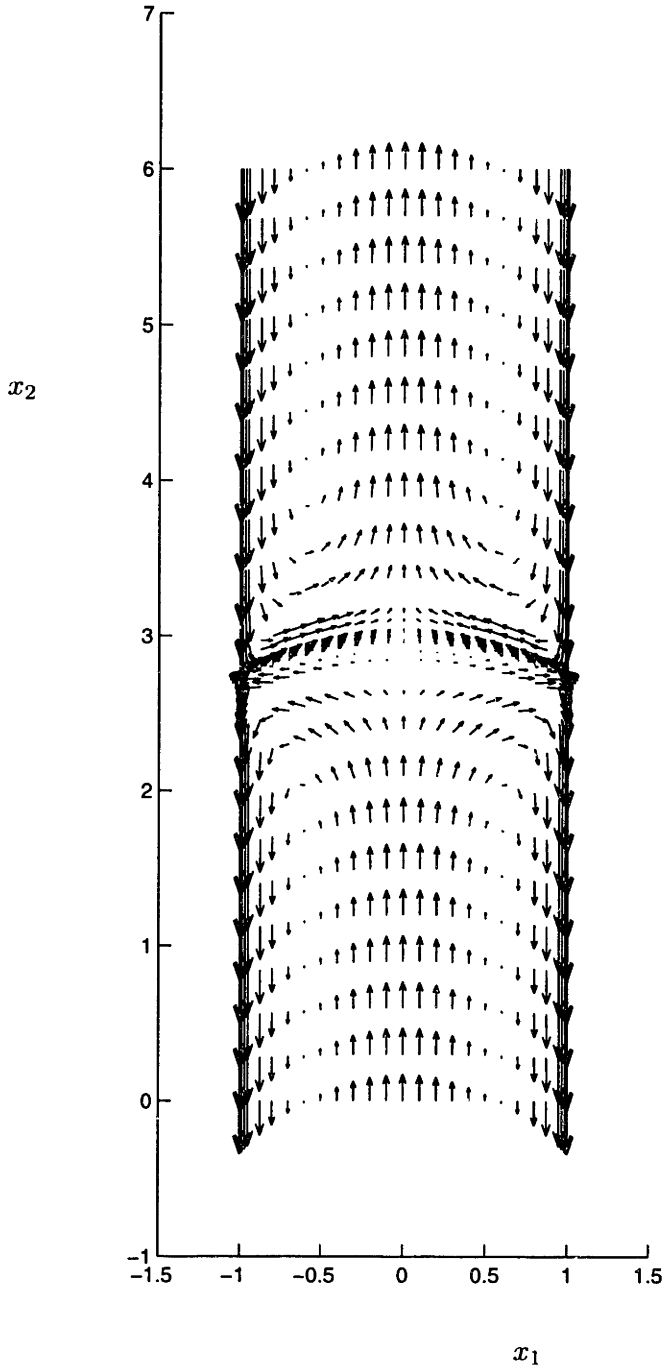

Figure 6-4: Velocity solution for $Ca = 0.02$.

direct comparison. Our results for interface shapes as a function of Ca are, however, in qualitative agreement with the axisymmetric results of [37], which considers the contact line involving two fluids of the same viscosity in a tube.

The existence of secondary recirculation regions in the advancing fluid (here Ω^1) is reported in [30, 37]. Mavridis et. al. [30], using a velocity profile along the slip wall rather than a Navier condition, found that the recirculation region occurs in the less viscous fluid. Similar results for fluids of the same viscosity are presented in [37]. We confirm the existence of secondary recirculation regions close to points G and H, in qualitative agreement with the results of [37] for the same choice of parameters ($Ca = 0.001, \theta = 40^o, \varepsilon = 0.006$). (Note, however, that our slip model and that of [37] are not the same.)

The iterative procedure exhibits fast convergence characteristics. Fig. 6-5 shows the intermediate two-fluid interface geometries obtained en route to convergence starting from a horizontal flat interface. In this example ($Ca = 0.02$) the maximum Δy change is less than 10^{-4} after 4 iterations. Note that the convergence is slower as Ca increases, since the importance of capillary forces diminishes [19]. The convergence rate is also sensitive to the slip length: for $\varepsilon \sim O(10^{-2})$ underelaxation – only a fraction (typically not smaller than 1/5) of the computed "correction displacement" Δy is used to obtain the next interface geometry – is required for $Ca > 0.05$, whereas for $\varepsilon \sim O(1)$ underelaxation is required only for $Ca > 0.1$. Fig. 6-6 shows the convergence process for π as a function of the iteration number for $Ca = 0.02$. We notice that π takes somewhat longer to fully converge than the two-fluid interface shape, which is a manifestation of the fact that it is fairly sensitive to small changes to the shape of Γ_f.

Our *spatial* convergence studies include the comparison of interface shapes for $Ca = 0.02$ as a function of the mesh size. Various mesh resolutions are used between 8×20 (the coarsest) and 12×28 (the finest). The two-fluid interface shapes obtained with the two most refined meshes (11×26 and 12×28) exhibit a maximum Δy deviation of less than 10^{-4}, suggesting that spatial convergence has, indeed, been obtained. The sensitivity of π to the exact shape of Γ_f is again obvious in these tests:

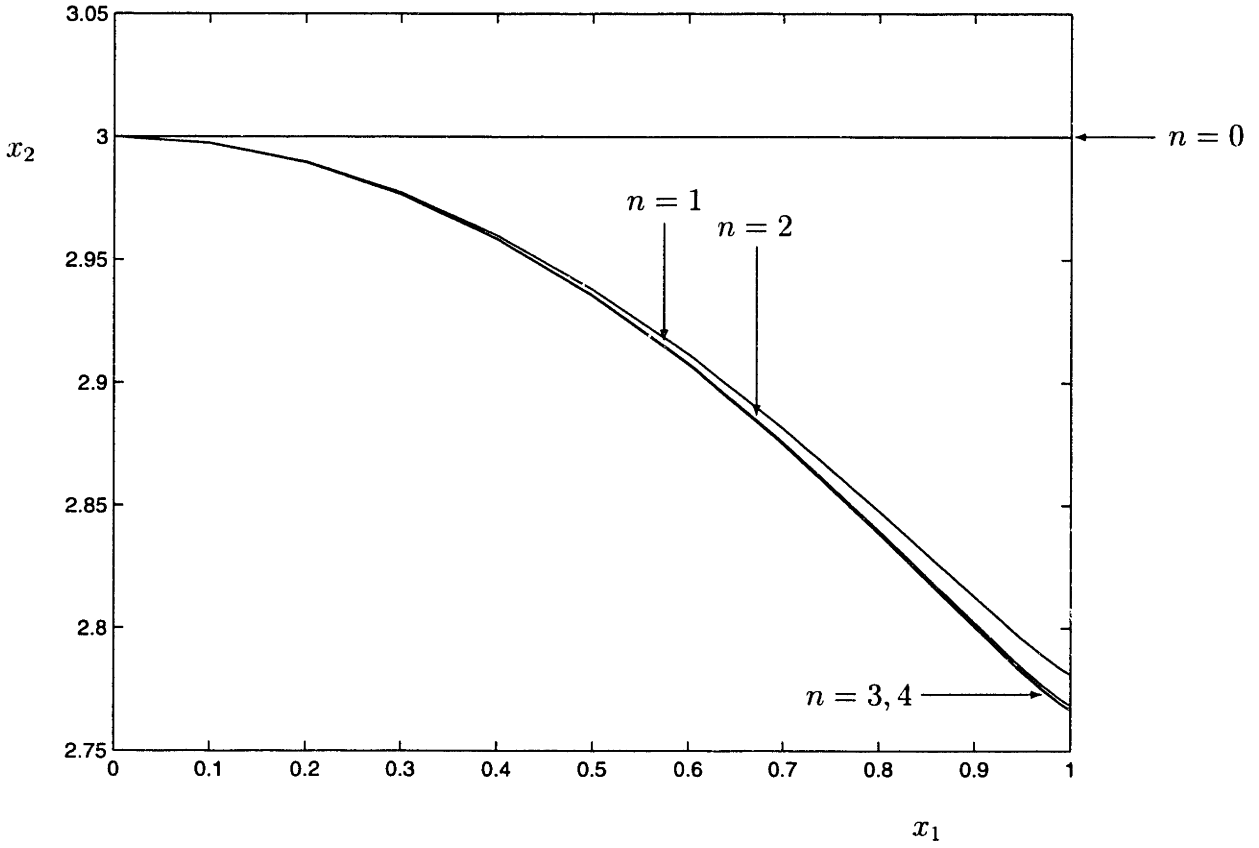

Figure 6-5: Two-fluid interface geometry convergence history for $Ca = 0.02$ (n = iteration number). Note that the axes are not drawn to scale to emphasize the differences between the various iterates.

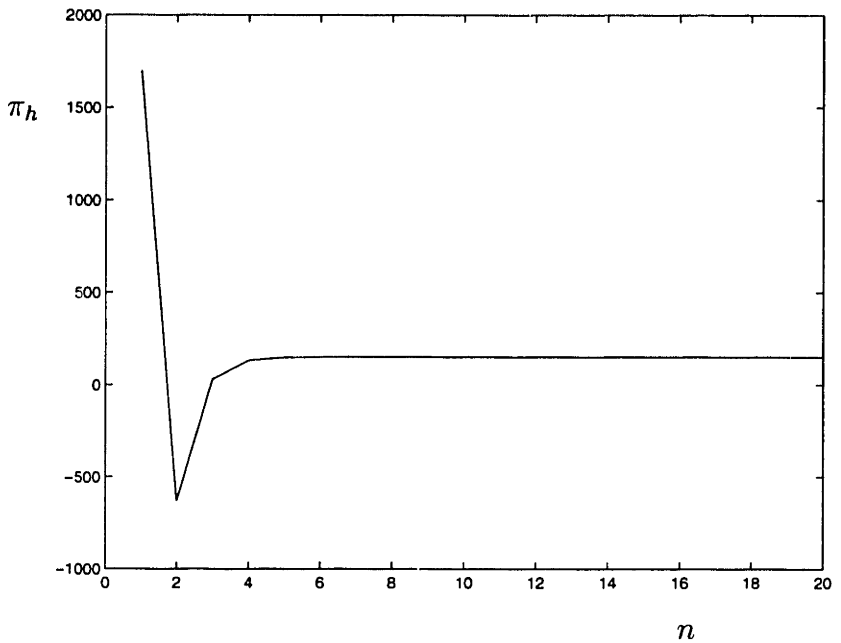

Figure 6-6: π_h convergence history for $Ca = 0.02$ (n = iteration number).

π still changes by 0.3% in proceeding from a mesh of 11×26 to a mesh of 12×28.

We also investigated the case of a specified slip profile along Γ_{CD}, $u_2(x_1 = H, x_2) = \mathcal{U}(x_2)$. The only change necessary to the formulation presented up to this point is the replacement of the natural boundary condition along Γ_{CD} with an essential boundary condition. We remark that the velocity degrees-of-freedom on the slipping wall are now excluded from the solution space of (6.35), and thus π (equation (6.44)) is "contaminated" by the residual of the equations involving those degrees-of-freedom. To illustrate this further, if we take v in (6.44) to be $v_1 = 0$ in Ω_h (the discretized domain) and $v_2|_{\Gamma_f} = 1$ and $v_2 = 0$ on all nodes not lying on Γ_f, we see that there exists an additional contribution from the part of v_2 untested in equation (6.35). This single-element contribution, however, is expected to vanish as $h \to 0$, and thus should not influence the results of our simulation when h is small.

We have verified the above assertion using the following method. We first compute the slip profile along Γ_{CD} for the baseline example presented above using the

Navier slip condition with $\varepsilon = 0.01, Ca = 0.02$, a 10×24 mesh, and a convergence criterion that the maximum Δy is less than 10^{-6}. We then use this slip profile as a Dirichlet boundary condition in a new specified-slip simulation with a similarly tight convergence criterion. We find that the difference between the converged interface shapes predicted by the two simulations is less than 10^{-6}.

6.7 Conclusions

In this chapter we have presented a new variationally consistent numerical solution technique for problems involving internal contact lines. The pressure indeterminacy is successfully removed by a force balance compatibility condition. The associated interface iterative method displays fast convergence characteristics for $Ca < 0.1$. Both Dirichlet and Neumann boundary conditions on the bounding walls have been investigated.

Our results show qualitative agreement with previous related work; it is, however, clear that although various assumptions can be made that lead to well posed mathematical problems, further modeling or physical input is required to elevate these "mathematical choices" from the ad hoc level to a more physically realistic level. The following chapters address the above issues through the use of molecular modeling techniques.

Chapter 7

Combining Molecular and Continuum Contact Line Simulations

This chapter develops the molecular modeling tools required to treat the moving contact line. As discussed in chapter 1 and the following section, the physical characterization of the moving contact line problem is seriously lacking and the use of molecular techniques can be very beneficial towards its final resolution. The molecular solutions presented in this chapter will serve as sources of modeling information for "molecularly derived continuum models" but also for comparison with the hybrid solution of the next chapter. As a result, the molecular model presented in section 7.2 has been "constructed" such that it can easily correspond to the continuum model of the previous chapter.

7.1 Introduction

The main reason for the intractability of the moving contact line problem lies in the multi-scale nature of the problem itself. The complete solution to the problem requires a fluid mechanical model at the macroscopic level, but also modeling at the molecular level if the correct contact line dynamics are to be recovered. Another

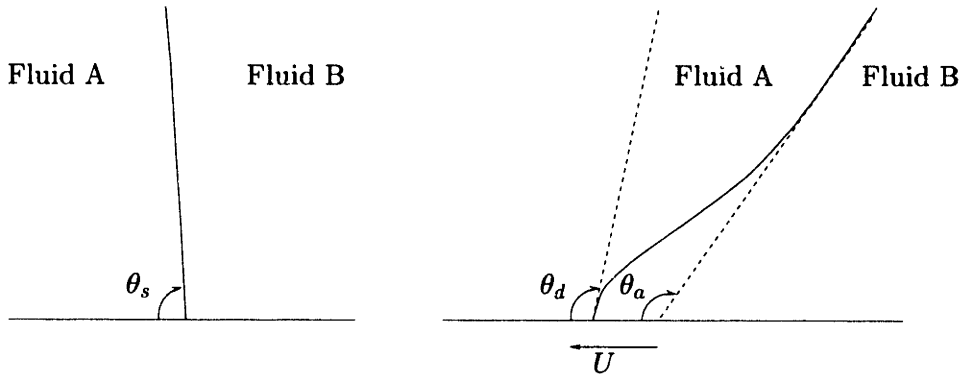

Figure 7-1: Definition of the static (θ_s), dynamic (θ_d), and apparent (θ_a) contact angles between fluids A and B.

reason is the lack of experimental evidence characterizing the molecular processes involved in the contact line dynamics. Experimental data are limited by resolution to the determination of an apparent contact angle θ_a which is the macroscopically "perceived" (coarse grained) angle between the two-fluid interface and the solid wall (Fig. 7-1 from [41]). Due to the significant curvature of the interface at molecular distances from the wall, the apparent and dynamic contact angles can be appreciably different.

Analytical [8, 9] or numerical [29] solutions of the moving contact line problem have been obtained by taking advantage of the relative insensitivity of the far-field solution to the exact contact line dynamics. The use of approximate models for the physics in the vicinity of the contact line with adjustable parameters results in solutions that can claim agreement with experimental macroscopic results. In particular, the logarithmic (with distance from the contact line) singularity present in the Navier-Stokes model of the contact line problem is relieved by relaxing the no-slip boundary condition close to the contact line. Various slip models are introduced, the most popular of which is the Navier condition, albeit for purely historical reasons.

Additional assumptions are required for the dynamic contact angle θ_d which enters as a boundary condition in the dynamical equations of motion. The usual assumption used in this case is that the dynamic angle has the same value as the static contact angle. Although there is no physical justification for this assumption, in this work we show that the dynamic contact angle can be taken to be independent of the Capillary number, $Ca = \mu U/\gamma$, and equal to the static contact angle. Here μ is the viscosity of one of the fluids, γ is the surface tension coefficient between the two fluids, and U is the characteristic velocity of the moving interface.

Molecular dynamics simulations have recently been used to treat the moving contact line problem [41] and [27]. Those simulations are, however, limited to very small systems ($\sim$ 5000 molecules) and cannot by themselves be used to treat macroscale problems. They can be used, however, as a means for developing physical models of the contact line behavior for use in macroscale (continuum) descriptions, or for the calibration of already existing molecular-kinetic models [38].

The present chapter reports results of this type: MD simulations have been used to extract information at the molecular level which serves as input for finite element simulations. In the only previous similar attempt to further develop the understanding of the physical processes occurring at the contact line [41] in terms of appropriate continuum boundary condition choice, the continuum model was not correct: the interface was treated as a rigid flat wall. In the above formulation the interface shape and the dynamic contact angle were not allowed to vary, and the capillary forces were not included; the simulation was, effectively, a Couette flow in a semi-infinite channel blocked at one end. In our study we utilize a full moving geometry finite element simulation of Stokes equations, with the appropriate variational treatment for the surface tension interaction between the two fluids developed in the previous chapter.

7.2 Molecular Dynamics Model

Our molecular dynamics simulations were focused on the immiscible fluid displacement problem; one fluid displaces a second fluid in a two-dimensional channel of

length $L' = 2L$ and width $2H$ (Fig. 7-2). The width of the channel is determined by the average location of the first layer of wall molecules (Fig. 7-2). It is convenient to study this problem in the reference frame of the moving interface: in this reference frame the interface does not move, and the walls of the channel move with speed $-U$ (where U is the speed with which the interface advances in the laboratory frame) in the $x-$direction. We also present some results for a Couette flow configuration (the two walls move in opposite directions) for comparison purposes with the work presented in [41].

As described in chapter 2, unless otherwise stated, all quantities will be expressed in reduced units using $\sigma = \sigma_{Ar} = 3.4$ Å for length, $m_{Ar} = 40$ amu for mass, $\varepsilon_{Ar}/k_b = 119.8^o K$ for temperature, and $\tau = (m_{Ar}\sigma_{Ar}^2/48\varepsilon_{Ar})^{1/2} = 3.112 \times 10^{-13} s$ for time. Here σ_{Ar} and ε_{Ar} are the parameters of the Lennard-Jones (LJ) potential for Argon [4], m_{Ar} is the mass of the Argon atom, and τ is the characteristic time for Argon. The interaction potential was truncated at the rather conservative cut-off length $r_c = 3\sigma$. The simulation box is a fully periodic MD domain of size $(L' \times D \times W) = (57.05\sigma \times 5.56\sigma \times 15.29\sigma)$ in the x, y and z directions respectively. Note that $2H \simeq 10\sigma < W$ as shown in Fig. 7-2 and discussed later.

The simulated fluid was chosen to be Argon for comparison purposes with other similar studies [41]. The Argon molecules are divided into two subspecies: subspecies A and B. These two subspecies (1280 molecules each) are completely identical because they have the same self interactions (V_{AA}, V_{BB}) and interactions with the walls of the system; they are, however, immiscible because the potential interaction between them (V_{AB}) is repulsive. More specifically, the potential used in this study

$$V(r) = 4\varepsilon[(\sigma/r)^{12} - \delta(\sigma/r)^6],$$

where r is the separation of the two interacting molecules, is a modified [41] form of the well known Lennard-Jones potential ($\delta = 1$). For the interaction between subspecies A and B, $\delta = -1$; for all other pairs of interactions $\delta = 1$. Hence for both

Argon A and B

$$V(r) = 4\varepsilon_{Ar}[(\sigma_{Ar}/r)^{12} - (\sigma_{Ar}/r)^{6}],$$

whereas

$$V_{AB}(r) = 4\varepsilon_{Ar}[(\sigma_{Ar}/r)^{12} + (\sigma_{Ar}/r)^{6}].$$

The above fluid characteristics were "constructed" for reasons of computational simplicity but also ease of matching of the molecular system properties with the continuum system properties. In continuum terms the behavior of the above molecular system is equivalent to two fluids with the same density and viscosity (equal to bulk values for liquid Argon); the fluids, however, are immiscible with a surface tension coefficient γ which can be calculated from molecular techniques [41]. More importantly, the two fluids interact with the two bounding walls in exactly the same way, and therefore, the static contact angle, by symmetry arguments, has to equal 90^o. Although this is not relevant to the molecular simulations it will be important when a connection is established (in the continuum context) between the static and dynamic contact angle in section 7.4.

Note that the interaction between Argon A and B is somewhat artificial because it is purely repulsive and of appreciable magnitude. This was preferred for reasons of computational simplicity: as we will see later, the two fluids are perfectly immiscible and the interface between them can be sharply defined. Fluids with a more "physical" potential interaction between them (a liquid with its vapor for example) produce very diffuse interfaces which require modeling assumptions before they can be defined in continuum terms that are compatible with our continuum simulations. Additionally, such fluids are unlikely to satisfy the requirements of equal density and viscosity.

Each of the two parallel, isothermal walls bounding the fluids is modeled by 600 wall molecules arranged in an fcc two-layer structure in the $x - y$ plane. The wall density, ρ_w, is equal to the fluid density, ρ. The outer of the two layers is constrained to move with velocity $-U$ in the $x-$direction and the molecules comprising it do not have thermal velocity. The inner layer obeys the usual Newtonian equations of motion but its temperature is rescaled in order to act as an energy sink and allow the simulation

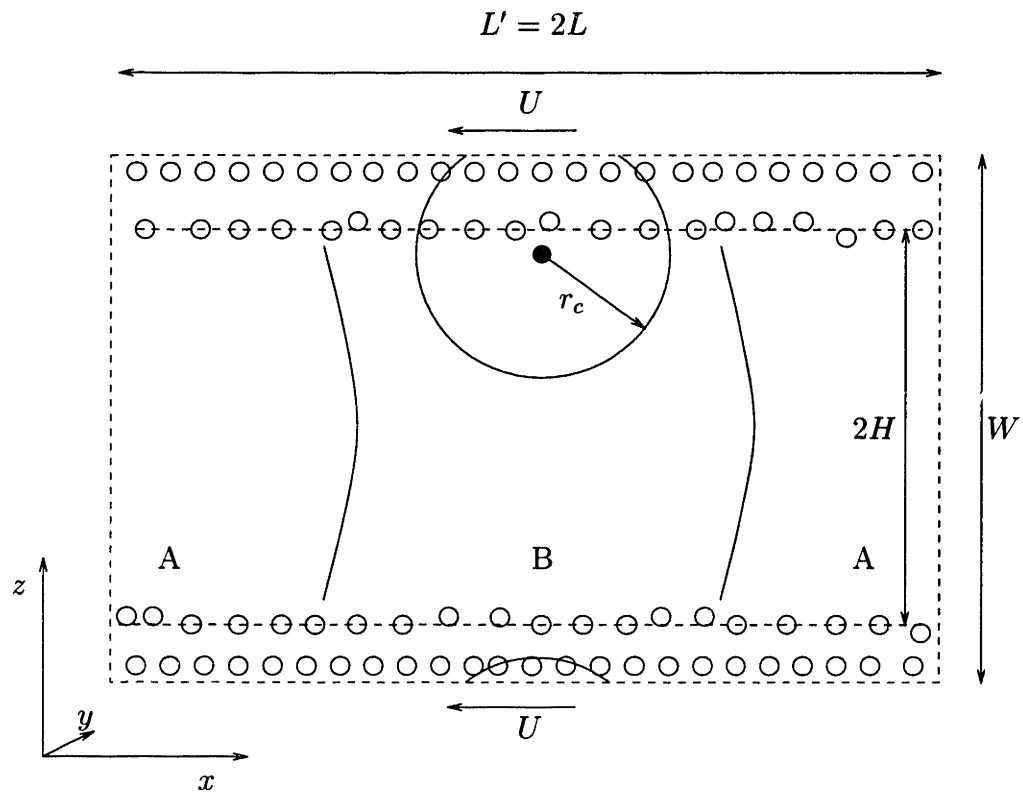

Figure 7-2: Sketch of problem geometry. r_c denotes the cutoff length for the intermolecular interaction. Wall molecules are denoted by open circles, and only one fluid molecule (dark circle) is shown for clarity.

to reach a steady non-equilibrium state by effectively imposing temperature boundary conditions on the fluid Argon. Similar models have been shown [27] to adequately capture the dynamics of wall-fluid interactions. The combined thickness (along the $z-$direction) of the two walls is greater than the interaction potential cutoff (r_c) such that

$$W - 2H > r_c \,, \tag{7.1}$$

and thus the fluid molecules do not see their images across the walls. The wall and wall-fluid potential parameters are: $m_W = 2m_{Ar}$, $\varepsilon_W = 5\varepsilon_{Ar}$, $\sigma_W = \sigma_{Ar}$, $\varepsilon_{WF} = 1.03\varepsilon_{Ar}$, $\sigma_{WF} = 1.03\sigma_{Ar}$. They do not represent any known solid material. They were chosen as a good compromise between the requirements of minimum number of wall molecules, a melting point that exceeds the highest temperature encountered during the simulation, minimum layering of the Argon molecules close to the walls, and minimum slip length. Modeling real materials by MD is a considerable challenge in itself; the potentials required are very complex but also very computationally inefficient. Although significant progress has been made in the development of accurate potentials for a variety of materials of interest, interactions between different materials (fluid-wall interactions for example) are not, in general, well understood to date. The modeling of real world materials was out of the scope of this thesis which focuses on numerical techniques.

The simulation box was periodic in all space dimensions. In the case of Poiseuille flow the method of "reservoirs" (chapter 4) was used to generate the flowfield: the fluid was given a parabolic (Poiseuille) velocity profile in the middle of each fluid bulk ("reservoir" locations RA and RB in Fig. 7-3) where the flow is expected to be fully Poiseuille by virtue of the fact that the distance to the two-fluid interface is longer than the molecular slip region. The velocity profile was imposed at "reservoirs" A and B (thickness $\Delta = 0.4\sigma$) by giving velocities to the molecules in RA and RB (for the whole duration of their residence in RA and RB), at each timestep, drawn from a Maxwellian distribution with a mean and variance consistent with the desired velocity and temperature of the fluid. This technique has been verified to reproduce

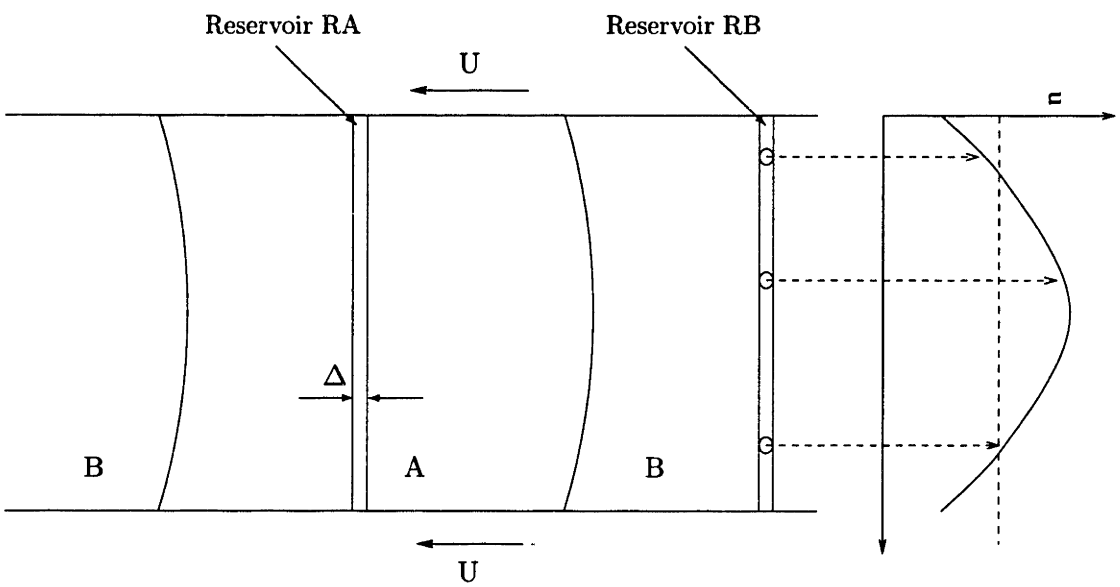

Figure 7-3: Flowfield imposition method.

the required flowfield with any adverse effects localized to the vicinity of the reservoirs ($\pm 0.5\sigma$) (chapter 4, [15]).

The simulations were conducted at the same average fluid density ($\rho = 0.81\sigma^{-3}$) and temperature ($T = 1.4$) as in [40] to facilitate comparison of the results, and use of the already calculated values of the viscosity $\mu = 2.0(\varepsilon m)^{1/2}/\sigma^2$, and surface tension $\gamma = 3.9 \pm 0.2\varepsilon/\sigma^2$ ($\delta = -1$).

The simulation was initialized and equilibrated for 960τ and then samples were taken for a further 2400τ. The flowfield was recovered by averaging the instantaneous molecular velocities in rectangular bins spanning the $x-z$ plane. The size of the bins was 1.43σ along the $x-$direction and 1.53σ along the $z-$direction. The resulting statistical errors for the velocity are expected to be less than $0.002\sigma/\tau$.

The Capillary number ($Ca = \mu U/\gamma$) was based on the wall velocity (U). Note that we need to differentiate between U and U_f (the fluid velocity in the bins adjacent to the wall at distances from the contact line greater than the slip length) because of the finite ratio (7%) of σ to the channel transverse (z) dimension; there are two contributions to the discrepancy between the two values: (i) the channel width is defined by the mean (during the course of the simulation) space occupied by the fluid molecules and does not include the void volume between the fluid and the walls that is a result of the repulsive core of the interaction potential (see, Fig. 7-2), and (ii) the velocity data closest to the wall are centered half bin thickness into the fluid in the $z-$direction. This means that for flows with high velocity gradients close to the wall, such as Poiseuille flow, the difference between the fluid velocity in the bin closest to the wall and the wall velocity is more than 10% even if no velocity slip is present at the wall. Note also that U_f is the fluid velocity far away from the contact line where slip is negligible; in other words it is the velocity recovered in the bins closest to the walls for a Poiseuille profile. The actual fluid velocity in the bins closest to the walls will be denoted u_f. We will denote the thickness of the "fluid region", that is the channel width excluding the void between the walls and the fluid, by $2B$.

We have ensured that the method of imposing the flowfield is consistent with previous reports of similar work by comparing the results of the former method for

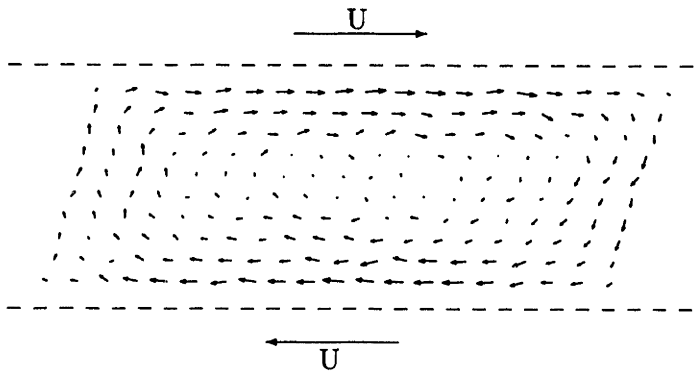

Figure 7-4: Flowfield for Couette configuration (only one fluid is shown). The walls are denoted by the dashed lines and move with velocity $U = \pm 0.018\sigma/\tau$.

$Ca = 0.059$ with results obtained by using gravity as the driving force for the fluid motion [27]. An acceleration due to gravity of $g = 0.00057\sigma/\tau^2$ in the streamwise direction was required in the latter case to generate a flow with the same Ca. The results of the two simulation methods were indistinguishable within the statistical accuracy of the simulations.

7.3 Molecular Dynamics Results

Fig. 7-4 shows the interface shapes for a Couette flow configuration. In this case the walls move in opposite directions ($U = \pm 0.018\sigma/\tau$) and effectively shear the fluid. This simulation was performed in order to assess qualitative agreement with the work of Thompson and Robbins [41, 40]. It was concluded in [41] and [40] that the dynamic value of the contact angle is the same as the static value (90^o). Although the contact angle is difficult to measure, in part because its definition is unclear at the molecular scale, we will show that in continuum terms the above assumption is correct.

Fig. 7-5 displays the flowfield obtained from the simulation of the immiscible fluid

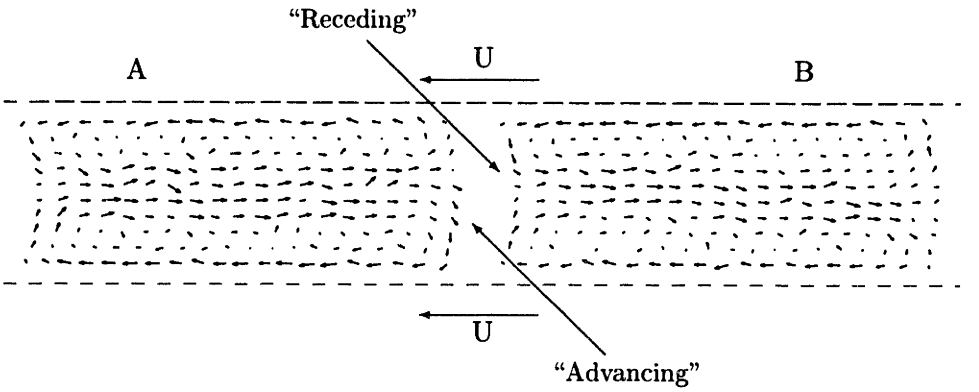

Figure 7-5: Flowfield for Poiseuille configuration. Both walls move with velocity $-U = -0.012\sigma/\tau$. Note the "mismatch" in curvatures of the two interfaces.

displacement problem. The walls move in the $x-$direction with $-U = -0.012\sigma/\tau$ and the Capillary number based on the wall velocity is $Ca = 0.059$. Both fluids are shown although the distance between them is not the same as in the actual simulation. The fluids are graphically displayed further apart in an attempt to illustrate a new *molecular* phenomenon: the interface shapes calculated by averaging the instantaneous positions of each fluid separately do not match exactly but actually show that the gap between the two fluids becomes larger close to the wall (see also Fig. 7-6; note that the profiles have again been shifted along the x-direction to facilitate comparison – unshifted interface shapes are shown in a later Figure). This effect reflects the change in molecular structure of the two fluids close to the walls in an attempt to accommodate the effects of shearing from a third substance (the wall). This effect is not observable on the macroscopic scale explaining why it has not been reported to date, although we have to add that the rather pronounced gap between the two fluids is an artifact of their very repulsive potential interaction.

We thus conclude that the two-fluid interface is not a mathematical two-dimensional surface but has three-dimensional structure (thickness $\sim 1\sigma$); its complete structure

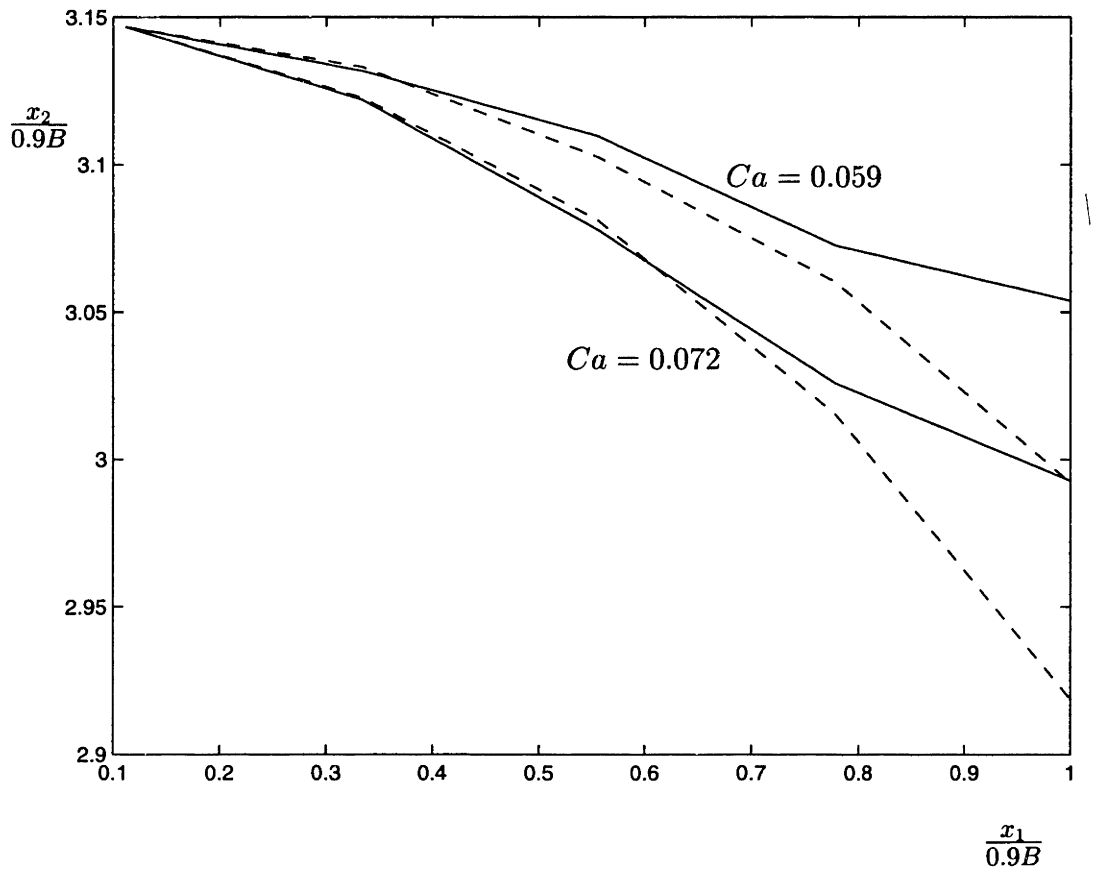

Figure 7-6: The two-fluid interface shapes for varying Ca. Advancing fluid fronts are shown in solid and receding ones in dashed. The channel centerline is at $x = 0$.

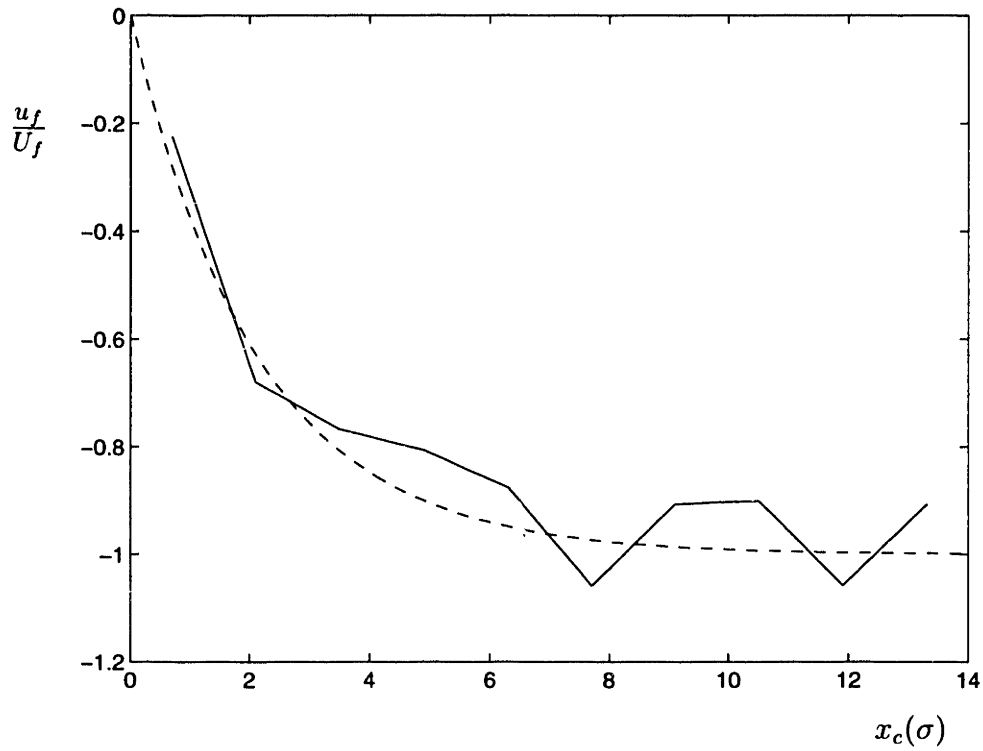

Figure 7-7: Slip model (dashed line) defined by equation (7.2) and a typical (slip) velocity profile obtained from simulations (solid line).

can be recovered from the averaged (in time) maximum excursions (as a function of z) of the fluid on each side. It is only a very good approximation to assume that the interface has zero thickness as the length-scales of the problem become macroscopic. We defined the two fluid fronts as "advancing" and "receding" as shown in Fig. 7-5. An advancing fluid front has an outward normal that is antiparallel to the wall velocity; conversely a receding front has an outward normal that is parallel to the wall velocity. Note that because of periodicity each fluid has one advancing and one receding front which are identical to the ones of the other fluid.

Molecular simulations also provide valuable information on the nature of the slipping mechanism between the wall and the fluid in the vicinity of the contact line. We have thus used our simulations to obtain a model of the slip along the wall close to the contact line. Fig. 7-7 shows the simulation results and a simple exponential fit of

the form

$$u_f = U_f(-1 + e^{(-0.47|x_c|)}) \tag{7.2}$$

to the slip profile along the wall, where u_f is the fluid velocity along the wall (following the definition of U_f and u_f discussed in the previous section), and x_c is the distance along the wall measured from the contact line. This molecular model was used in the finite element simulations of the fluid displacement problem which follow, in the form of velocity boundary condition along the slipping wall.

7.4 Finite Element Simulations

We have now developed both continuum (chapter 6) and molecular simulation techniques for the moving contact line problem. In the following section we attempt to combine the two in a serial, or molecular *then* continuum, approach. We would like to know whether the molecular information can in any way be used to provide continuum models for the dynamic contact angle and fluid slip behavior; these models can be very useful in fully continuum simulations.

7.4.1 Numerical Model

The continuum analog of the molecular model described in this chapter comprises of two immiscible fluids of the same density and viscosity in a two-dimensional channel. The aspect ratio of the channel $L/H = 5.7$ is preserved as, of course, all the governing non-dimensional groups; the Capillary number of the molecular simulations is matched by the appropriate choice of $\gamma = 1/Ca$ in the continuum simulations since we can assume that $\mu = \rho = 1$ in the latter. The problem geometry is thus the same as Fig. 6-1; the existence of two two-fluid interfaces in the molecular solution is an artifice of the periodic boundary conditions imposed on the molecular dynamics simulation.

In a continuum context, and in particular in this specific finite element model, the solution of this problem requires the determination of a flowfield $(u = (u_1, u_2), p)$ and

a consistent two-fluid interface (Γ_f) shape $y_s = y_s(x_1)$. Here u is the fluid velocity vector and p is the fluid pressure, and $y_s(x_1)$ is the two-fluid interface position as a function of x_1.

We seek the solution in the reference frame of the moving interface (Γ_f) because in this frame of reference the solution is steady and simplifies the solution procedure greatly. As discussed above, the flow is expected to be fully developed (parabolic velocity profile) far away from the contact line. Since the interface is not moving in the chosen reference frame, there is no net fluid displacement, and thus this fully developed profile has zero-net-mass flux. The Dirichlet zero-net-mass flux parabolic profile boundary conditions on Γ_{AD} and Γ_{BC} are preferable in the case of the finite element simulation (instead of the periodic boundary conditions used in the MD simulations) because, by again utilizing symmetry, they reduce the computational cost by a factor of two.

The equations governing the fluid flow are the steady incompressible Stokes equations given again here for completeness:

$$\frac{\partial \sigma_{ij}}{\partial x_j} = 0 \text{ in } \Omega, \tag{7.3}$$

$$\frac{\partial u_i}{\partial x_i} = 0 \text{ in } \Omega, \tag{7.4}$$

where

$$\sigma_{ij} = \mu\left(\frac{\partial u_i}{\partial x_j} + \frac{\partial u_j}{\partial x_i}\right) - p\delta_{ij} \tag{7.5}$$

is the stress tensor. Here δ_{ij} is the Kronecker-delta symbol. We adopt the Einstein summation convention, and further assume that all unrepeated indices range from 1 to 2. We neglect gravity forces, though these can, of course, be readily included. Note also that these equations correspond to the coordinate frame of Fig. 6-1.

The boundary conditions are then given by

$$\hat{n}_i(\sigma_{ij}|_{\Gamma_f^2} - \sigma_{ij}|_{\Gamma_f^1})\hat{n}_j = \gamma\kappa \text{ on } \Gamma_f, \tag{7.6}$$

$$\hat{t}_i(\sigma_{ij}|_{\Gamma_f^2} - \sigma_{ij}|_{\Gamma_f^1})\hat{n}_j = 0 \text{ on } \Gamma_f, \tag{7.7}$$

$$\frac{dy_s(0)}{ds} = 0, \tag{7.8}$$

$$\frac{dy_s(H)}{ds} = cos\theta, \tag{7.9}$$

and

$$u_1 = 0 \text{ on } \Gamma, \tag{7.10}$$

$$u_2 = U\,g, \text{ on } \Gamma_{AD}, \Gamma_{BC}, \tag{7.11}$$

$$u_2 = U\,q, \text{ on } \Gamma_{CD}, \tag{7.12}$$

and

$$\sigma_{21} = 0 \text{ on } \Gamma_{AB}. \tag{7.13}$$

Here $\hat{n}_i$ and $\hat{t}$ are the right-handed outward unit normal and tangent on Γ_f; Γ_f^2 and Γ_f^1 refer to the limits as we approach Γ_f from Ω^2 and Ω^1, respectively; κ is the curvature; s is the arc length coordinate along Γ_f such that $s = 0$ and $s = S$ correspond to points G and H on Γ_f, respectively; Γ is the union of $\Gamma_{AB}, \Gamma_{BC}, \Gamma_{CD}$, and Γ_{DA}; g is the parabolic zero-mass-flux profile, $g(\frac{x_1}{H}) = \frac{1}{2} - \frac{3}{2}(\frac{x_1}{H})^2$, and q is the slip profile from equation (7.2), $q = (-1 + e^{(-0.47|x_c|)})$.

The details of the derivation of the variational-weak form of equations (7.3)-(7.13) and a suitable triangulation of the solution domain Ω can be found in chapter 6. We will discuss the results in the following section.

7.4.2 Results

The results of the finite element simulations are shown in Fig. 7-8 and Fig. 7-9. Fig. 7-9 shows the two-fluid interface thickness correct to scale. The simulations utilize the molecular slip model (equation (7.2)) obtained in section 7.3. A further assumption was introduced (Fig. 7-8 and Fig. 7-9): the dynamic contact angle was taken to be equal to the static (90^o); our aim is to examine the validity of this assumption that is usually found in the literature [41]. The continuum simulation extends to $x_1 = 1.16B = 1H$; in other words, the continuum wall is identified with the first layer of wall molecules (see Fig. 7-2). On the other hand, the molecular interface shapes can

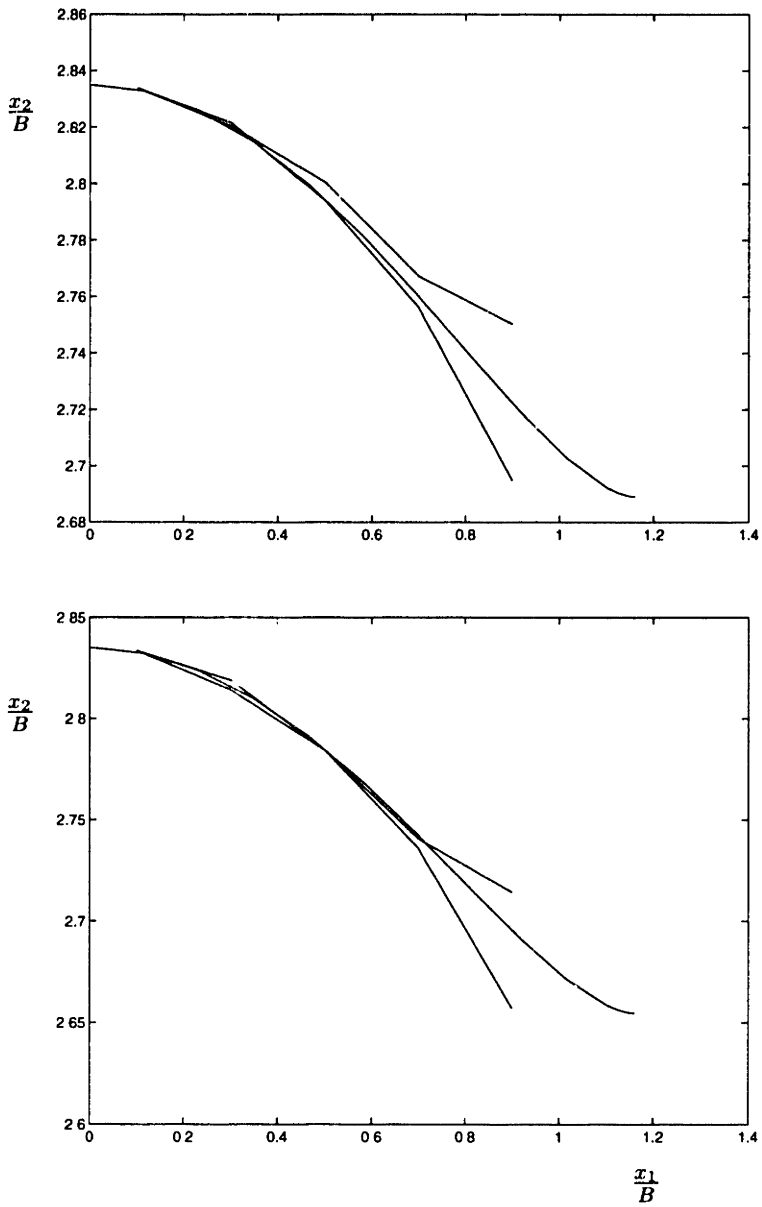

Figure 7-8: Comparison between molecular result and finite element simulation result (line that extends to $x_1/B = 1.16$) with dynamic contact angle equal to the static value (90^o) for $Ca = 0.059$ (top) and $Ca = 0.072$ (bottom).

only be defined for $0 \leq x_1 \leq 1B$ because they are limited to the volume occupied by the fluid only; furthermore the last data bin is centered on $x_1 = 0.9B$. We use B to normalize x_1 to emphasize this distinction. Although it may be argued that the gap between the wall and the fluid belongs to neither, this definition was preferred because of its ability to capture the fluid behavior in the best continuum-like way: if we neglect the effect of the thickness of the two-fluid interface which cannot be accounted for by the mathematical idealization used in the finite element method, the agreement is excellent in the region away from the walls were continuum fluid mechanics is adequate. Close to the walls purely molecular effects are present but the agreement is still very good. More importantly, we see that the dynamic contact angle *can* be taken to be equal to the static *in this approximation.*

We can, alternatively, repeat the continuum simulations by assuming that the fluid region is delimited by the extent to which fluid molecules can be found, that is, do not include the gap between the fluid and the wall in the simulation. Fig. 7-10 shows the results of such a comparison. The agreement is again very good, but now the angle has to be adjusted to a value different than 90^o for the profiles to agree. Although it can be argued that this in effect measures the contact angle at the edge of the fluid region, care must be taken because the simulations of Fig. 7-10 are not just the results of Fig. 7-8 shown only up to $x_1/B = 1$. In Fig. 7-8 the Dirichlet boundary conditions are applied at $x_1 = H = 1.16B$ whereas in Fig. 7-10 they are applied at $x_1 = 1B$. More importantly, the Capillary number (Ca') is now based on the fluid velocity at $x_1 = 1B$, and hence, in this new interpretation, has lower values ($Ca' = 0.045$ for $Ca = 0.059$, and $Ca' = 0.055$ for $Ca = 0.072$).

The dynamic contact angle may be expected to be a function of the relative strength of the interaction between the wall and the two fluids: the stronger the attraction between the fluid and the wall the larger the difference between the dynamic and static values of the contact angle. Since our system parameters did not correspond to any known fluid-wall system, we did not pursue the complete characterization of the relation $\theta_d = \theta_d(Ca, \{\varepsilon, \sigma\})$, where $\{\varepsilon, \sigma\}$ denotes the complete set of Lennard-Jones parameters for all the system constituents; this issue will be the subject of future

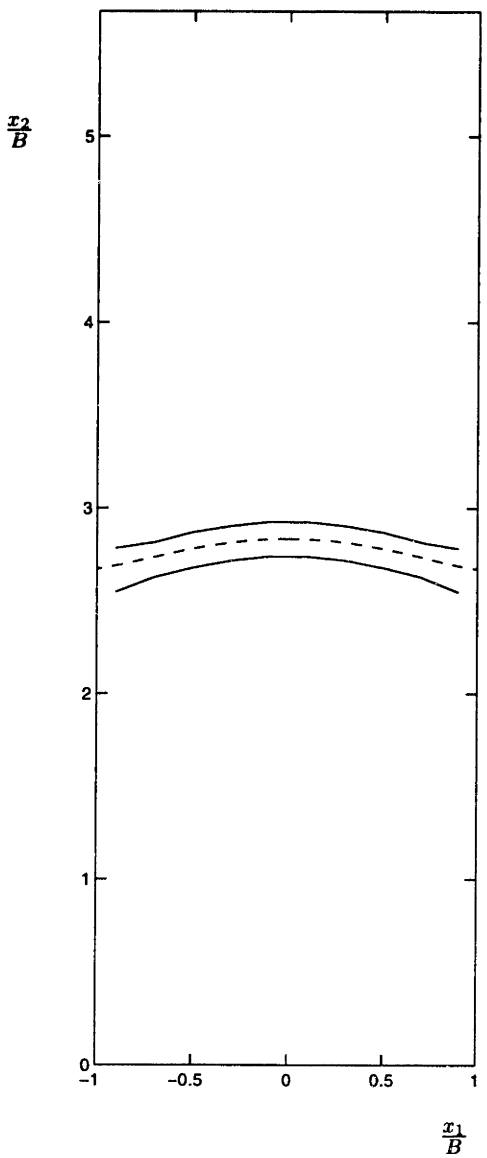

Figure 7-9: Comparison between molecular result and finite element simulation result (dashed line) with dynamic contact angle equal to the static value (90°) for $Ca = 0.059$.

work that will include the use of accurate interaction potentials for the simulation of realistic engineering materials. Additional further work will focus on situations where the static contact angle is different than 90^o, to which it is not yet clear that our conclusions could by extended. In particular, the limit $\theta_s \to 0$ is a more physically interesting case because of the more pronounced wedge flow that exists close to the contact point in that case. Additionally, most realistic contact angles have values closer to that limit rather than the opposite limit of $\theta_s \to 90^o$.

Despite the fact that the Navier condition

$$\sigma_{21} = -\frac{\mu}{\varepsilon}(U + u_2) \text{ on } \Gamma_{CD} \tag{7.14}$$

is the most popular of the slip models used, we found that in this case it could not be used with satisfactory results; this indicates that it indeed does not contain the correct physics involved in the vicinity of the contact line, but rather depends on the insensitivity of the far field solution to the exact slip model used. Its inadequacy stems from the fact that it introduces slip by setting a limit on the maximum allowable stress close to the wall. If the slip length is of the order of the channel width ($\varepsilon \sim H$), equation (7.11) implies that significant slip will be present for the whole length of the slipping wall, which is not true in our simulations.

7.5 Conclusion

This study has shown that, excluding purely molecular effects which are observable only at the microscopic level, continuum methods can reproduce moving contact line dynamics given correct "boundary conditions" (in our case molecularly derived) for the slip profile along the channel wall and the dynamic contact angle. For the set of fluid-wall interactions of our study, we find that the assumption that the dynamic contact angle is approximately equal to the static angle is reasonable. Although the technique used here is not entirely satisfactory, since a comparison with "exact" molecular results is always required, this method can lead to the development of

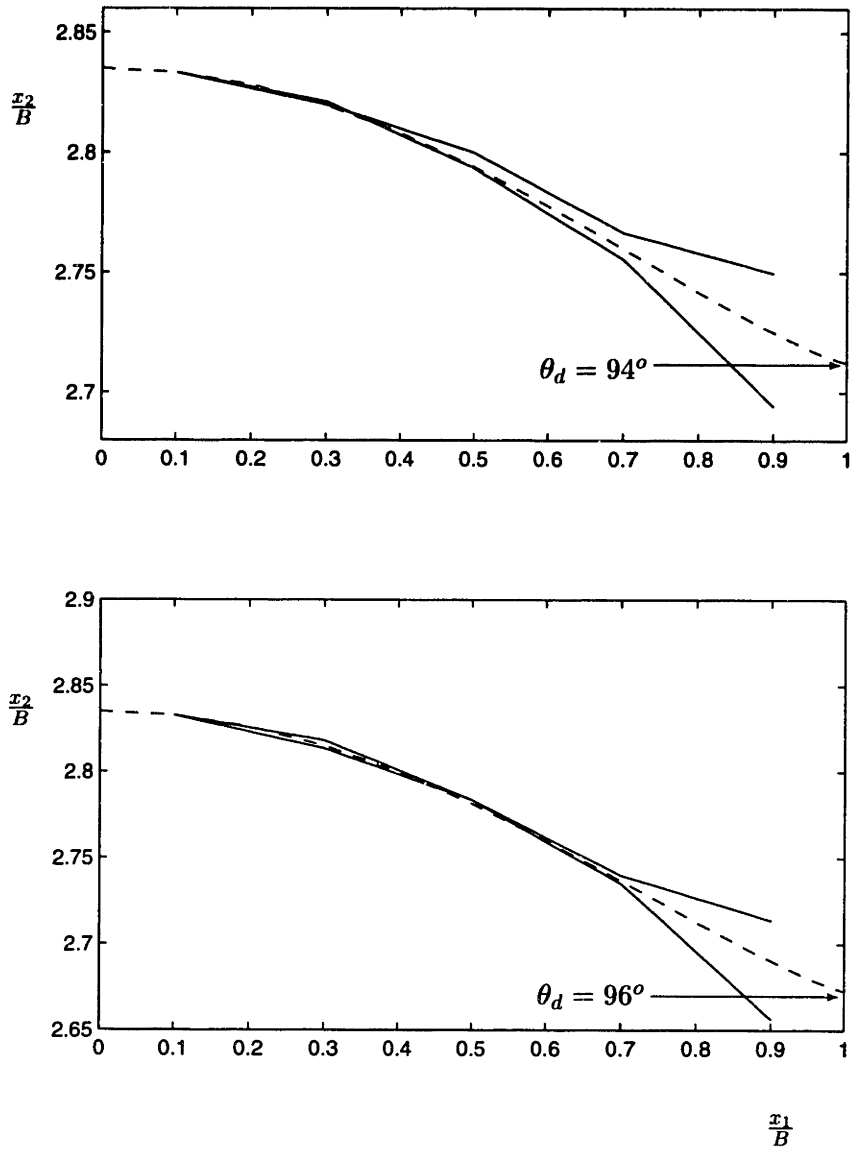

Figure 7-10: Comparison between molecular result and finite element simulation result (dashed line) with the wall at $x_1 = B$ and dynamic contact angle adjusted for agreement with the molecular results for $Ca' = 0.045$ (top) and $Ca' = 0.055$ (bottom).

constitutive models for the continuum description of moving contact lines.

Additionally, this work has shown that the molecular input required in a continuum simulation is localized to within one slip length from the contact line and suggests that hybrid algorithms which utilize MD in the vicinity of the contact angle and finite elements (FEM) for the far field solution are indeed feasible and would be of great value for this problem.

Chapter 8

Hybrid Atomistic-Continuum Solution of the Moving Contact Line Problem

We return to the hybrid solution framework developed in chapters 3-5. The moving contact line problem is ideally suited to our simulation technique; chapters 6 and 7 have shown that although empirical or semi-empirical continuum numerical approaches can be "guided" towards reasonable approximations, a hybrid technique can offer predictive power which is what empirical models presently lack.

Applications of the hybrid technique to the moving contact line problem are advantageous with respect to a fully molecular solution in cases where the extra cost associated with the iteration process is offset by the reduced cost of continuum solutions over the vast majority of the total simulation region. In fact, computational time savings of the order of 10^6 can be achieved. As we saw in the previous chapter the molecular treatment can be limited to regions of size 50Å enclosing the contact point; at greater distances from the contact point, continuum fluid mechanics has been shown to be equivalent to the molecular description. Hence for a two-dimensional flow in a Capillary of diameter of the order of $1\mu m$, the ratio of the molecular region to the total computational domain is $\sim (50\mathring{A})^2/(1\mu m)^2 = 2.5 \times 10^{-5}$ which translates to a gain of $4,000$ if we assume that the computational cost of the continuum solution is

negligible, and that the number of iterations required for convergence is of the order of 10. For three dimensional problems the gain scales as the third power of the linear dimension ratio between the molecular region and the whole simulation domain and therefore the potential savings are even greater. We have also taken a conservative estimate of the size of the macroscopic problems that can be treated because of noise issues discussed in chapter 5 that are expected to limit this maximum macroscopic size; if macroscopic problems of the order of $1mm$ are treated the above estimated gain is increased by a factor of 10^6 for two-dimensional problems.

In this thesis we present results obtained for the simulation geometry of chapters 6 and 7. Therefore there is no computational cost gain for this specific problem; in fact, the hybrid solution is more costly than the fully molecular solution. The objective, however, of this study is the validation of the hybrid technique on this very demanding problem. In particular, the existence of two fluids complicates the coupling technique and requires a more careful comparison of the hybrid results with already established correct solutions. In addition to the above, this comparison is an extra test for our hybrid technique in the sense of a comparison with a fully molecular solution; the comparisons of chapters 4 and 5 were made against continuum results.

The presence of two fluids and their associated interface requires changes to the Schwarz theory; the iteration procedure remains largely unchanged except for the inclusion of the two-fluid interface angle in the boundary data that are passed on from the molecular to the continuum iterate, but care must be taken in the handling of the two fluid domains and the placement of the overlap region such that mass continuity is preserved. The above issues will be discussed extensively in section 8.1.

8.1 Hybrid Solution Procedure

The hybrid solution geometry is the same as the one used for the fully continuum solutions of chapter 6 (Fig. 6-1), and the fully molecular solutions of chapter 7; note that the molecular simulation domain (as in chapter 7) has a length of $L' = 2L$ because the periodic boundary conditions used in the molecular dynamics simulation

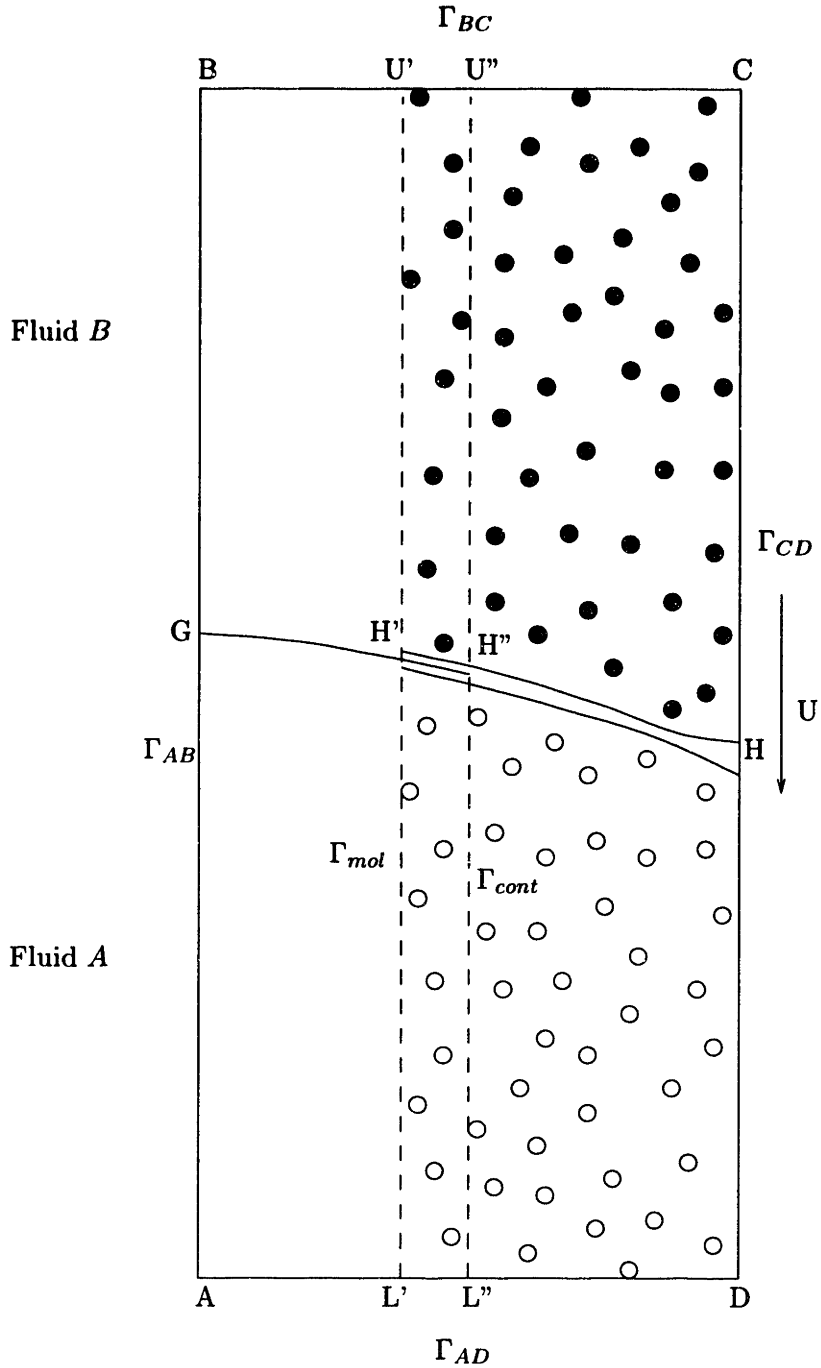

Figure 8-1: Hybrid formulation geometry.

which result in two two-fluid interfaces. Figure 8-1 shows the continuum, molecular, and overlap region of the hybrid solution. The region close to the wall is treated by molecular dynamics, whereas the region close to the centerline of the channel is treated by continuum fluid mechanics. It is effectively a "one dimensional Schwarz" with both subdomains extending to Γ_{BC} and Γ_{AD}. In particular, starting from the centerline of the channel (Γ_{AB}), the continuum region measures $0.5B$ (units introduced in chapter 7) to Γ_{cont} (U"L"), and the molecular region covers from Γ_{mol} (U'L') to the wall Γ_{CD}. The overlap region (between Γ_{cont} and Γ_{mol}) has a width of $0.2B$ and extends into the continuum region. In other words, the molecular only simulation covers, in addition to the wall, exactly $0.5B$ of fluid, whereas the continuum only region covers $0.3B$.

The physical problem dimensions favored the extension of the molecular region to the full channel length (up to Γ_{BC} and Γ_{AD}); slip was important in approximately 50% of the channel length and hence the inclusion of overlap regions in the streamwise direction was impractical. This, of course, will not be the case for macroscopic problems in which slip is limited to very small fractions of the channel length.

One of the most serious complications arising from the nature of the moving contact line problem was the treatment of the loss of material due to the deflection of the interface in the direction of motion of the walls. As the interface deflects downwards in the convention of Fig. 8-1, material A is replaced by material B. In continuum formulations this does not introduce any problems because there is no actual material exchange; material conservation is achieved if the integral of mass flux over the simulation boundary is balanced by the combined effect of any mass sources or sinks in the simulation domain. On the other hand, in molecular dynamics careful management of the material is required. In order to solve this problem we can take advantage of the fact the MD automatically honors the material conservation condition–even in compressible situations.

The circular arrow in Fig. 8-2 shows a sketch of the path characteristic of fluid B; the fluid recirculates in the volume that is accessible to itself without mixing with fluid A, honoring mass conservation while adjusting the interface shape to satisfy the requirements of the governing equations of motion. Note that although half of the

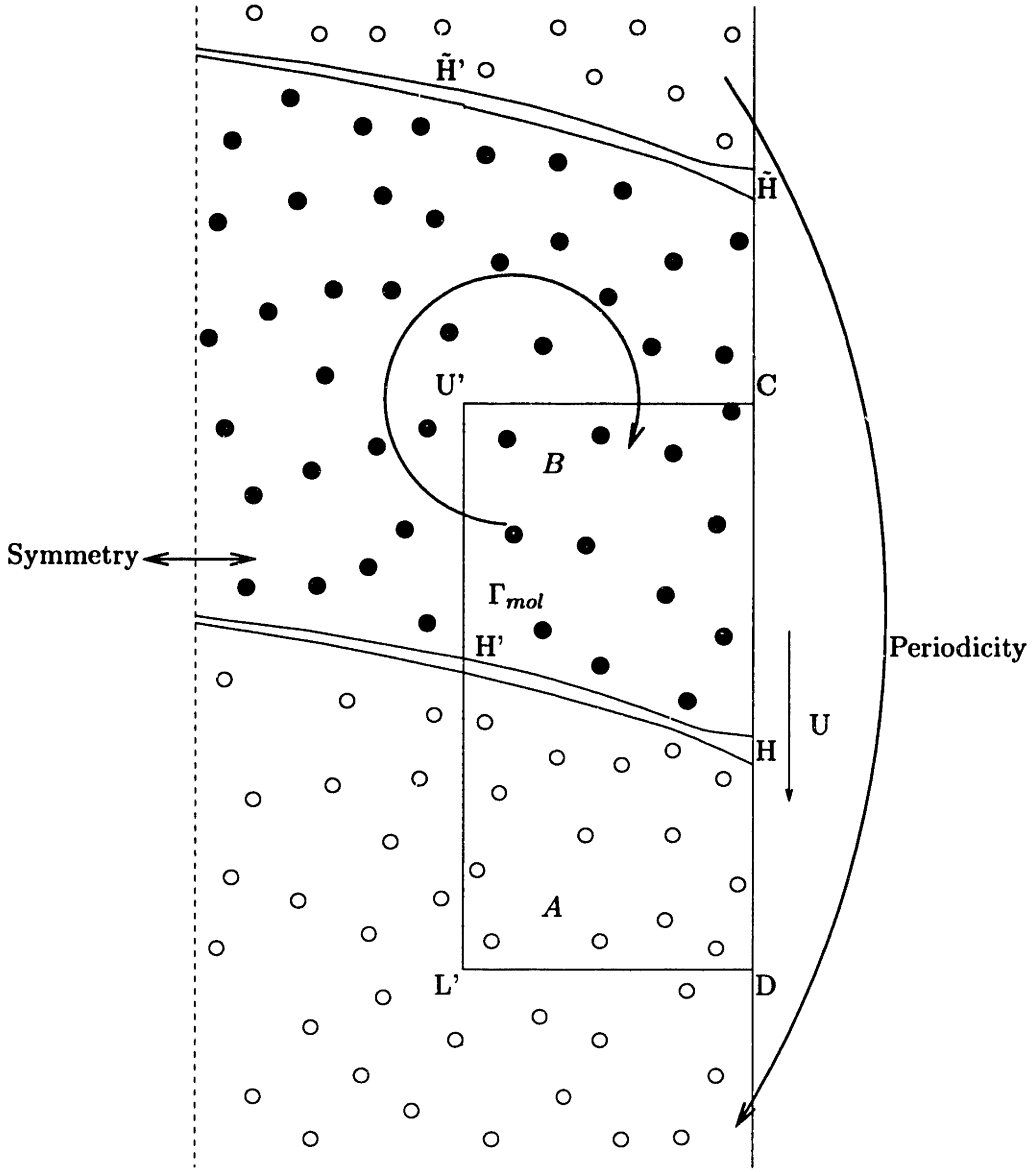

Figure 8-2: Material management in the molecular simulation. Only half of the channel is shown due to symmetry considerations. The box L'U'CD corresponds to the hybrid solution geometry of Fig. 8.1. Note the complementary region U'H̃'H̃C for fluid B that is equivalent to the primary region L'H'HD for fluid A, and conversely for L'DH̃H̃' for fluid A.

channel was omitted for clarity, the simulation was held over the full channel width for reasons of computational convenience. We can see that both fluids have advancing and receding fronts as remarked in chapter 7. Although for purposes of demonstration we focus on the advancing front of fluid A and the receding part of fluid B, which we will refer to as the primary regions, note that the complementary regions of each fluid are completely interchangeable with the primary region of the other fluid; in fact the statistics for fluid-front shapes and the flowfield are taken over both primary and complementary regions. Thus when material A is expelled from the primary simulation domain, through the face L'D say, due to the change of the interface shape from one iteration to the next (Fig. 8-2), this expelled material just enters the complementary region of material A that is the mirror image of the expanding primary region of material B; no action is required to convert that material into material of type B and return it to the simulation through face U'C. We have therefore succeeded in using the original simulation of chapter 7 for the hybrid formulation of this chapter by using the region of the channel not included in the hybrid formulation as our particle reservoir.

The deflection of the contact point H in the direction of the wall motion results in unequal subdomain boundary lengths (U'H'>L'H', U"H">L"H"). This poses additional problems in our matching algorithm as the molecular and continuum lengths of the above segments do not match after every iteration step. For example the length of H'U' in the continuum simulation will not be the same as in the molecular simulation that follows because the interface during the new molecular step will deflect unless convergence has obtained. We can overcome this problem by using points H' and H" as Lagrangian references. Coordinates along the above segments are defined starting from points H' and H" to facilitate the mappings from the molecular to the continuum spaces and vice versa. We then exploit the fact that the flowfield relaxes to the Poiseuille profile with no slip on the wall (see Figs. 7-5, 7-7) as we move away from the contact point. This flowfield property has been a requirement for the validity of the continuum solution (see chapter 6) and is a result of the fact that the slip length is smaller than $L/2$. The length changes of the domains are then assigned

at points B, C (fluid B), and A, D (fluid A), which are sufficiently far away from the contact point so that there is no important molecular information in the velocity profiles: the velocity profiles can then be freely truncated on segments H'L' and H"L" or extrapolated on segments H'U' and H"U", in order to compensate for the variable length of the corresponding boundary segment of the previous iterate.

8.1.1 Modified Schwarz Method

To our knowledge no previous work has been done on the coupling of two fluid-flows using the Schwarz method. Our approach for this problem is an extension of the Schwarz technique presented in chapter 3: during the course of a full iteration the continuum solution provides new boundary conditions for the molecular simulation on the boundary of the latter which lies well within (thickness of the overlap region= $0.2B$) the continuum domain; the molecular solution in turn provides a new set of boundary conditions for the continuum simulation on the boundary of the latter which again lies inside the molecular domain. Fig. 8-3 shows the continuum results on Γ_{mol} that serve as boundary data for the molecular simulation. Fig. 8-4 shows the reverse procedure that completes one full iteration cycle: molecular data on Γ_{cont} serve as boundary conditions for the continuum simulation. The continuum solution, however, requires an angle boundary condition for the contact point, or more strictly in this case, the point where the two fluid interface meets the boundary of the continuum simulation; it, of course, requires one at the centerline of the channel which is always 90^o by symmetry. The two boundaries, Γ_{cont} and Γ_{mol}, do not exist in reality–they are artifacts of the hybrid treatment; they do, however, represent a boundary for the continuum simulation. The angle boundary condition (at point H") is taken by averaging the shape of the interface in the molecular solution and extracting its slope at point H".

The dashed lines in Fig. 8-4 denote the smoothed molecular dynamics profiles. Similarly to the test problem of chapter 5, we have used third order polynomials to fit the noisy molecular dynamics velocity profiles before using them as boundary conditions for the continuum iterate. The normal velocity (u_1) profiles were also

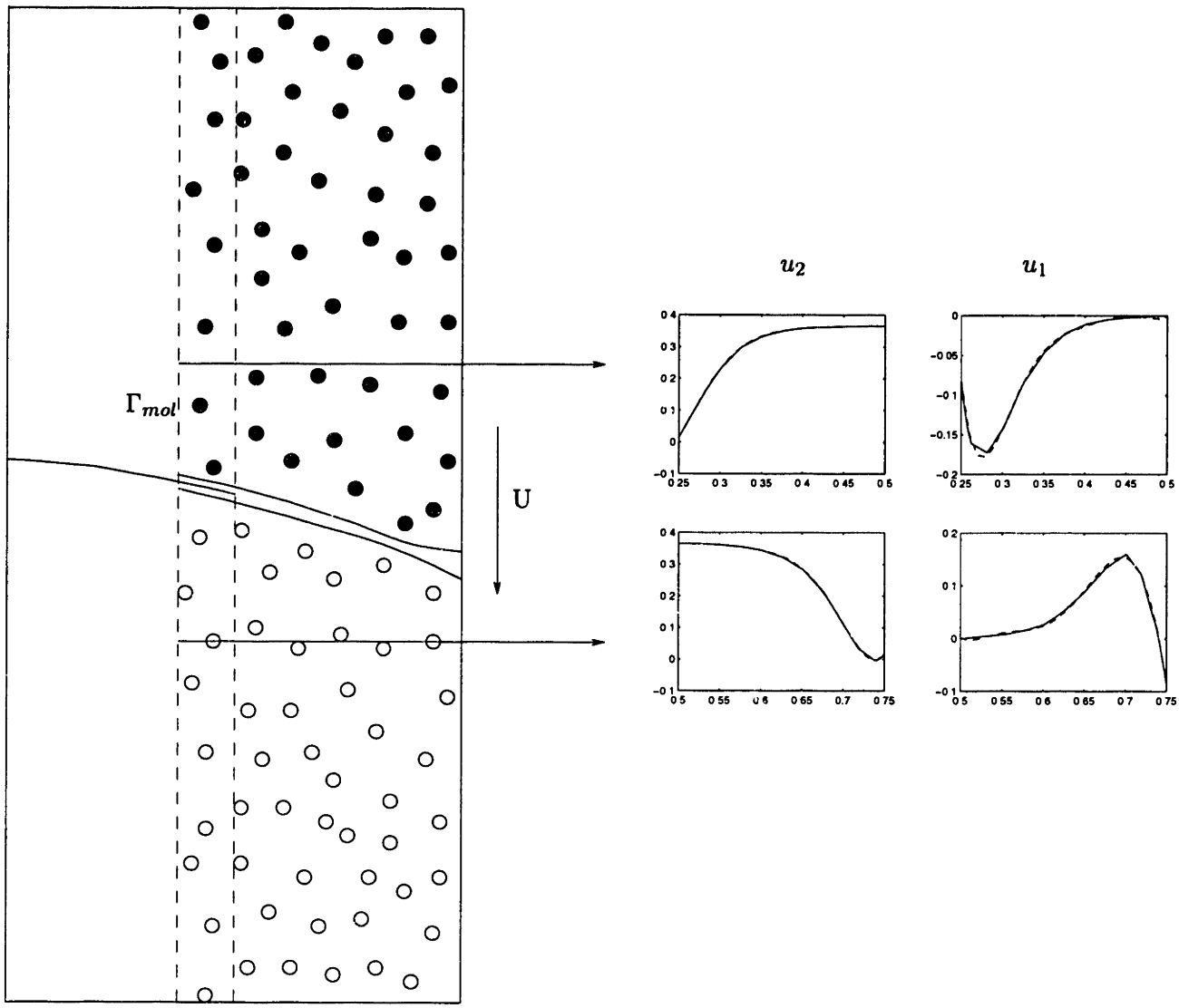

Figure 8-3: First part of one Schwarz iteration: continuum data on Γ_{mol} is used as boundary condition data on the molecular simulation. The solid line represents the actual data, and the dashed line the fit used to impose the data.

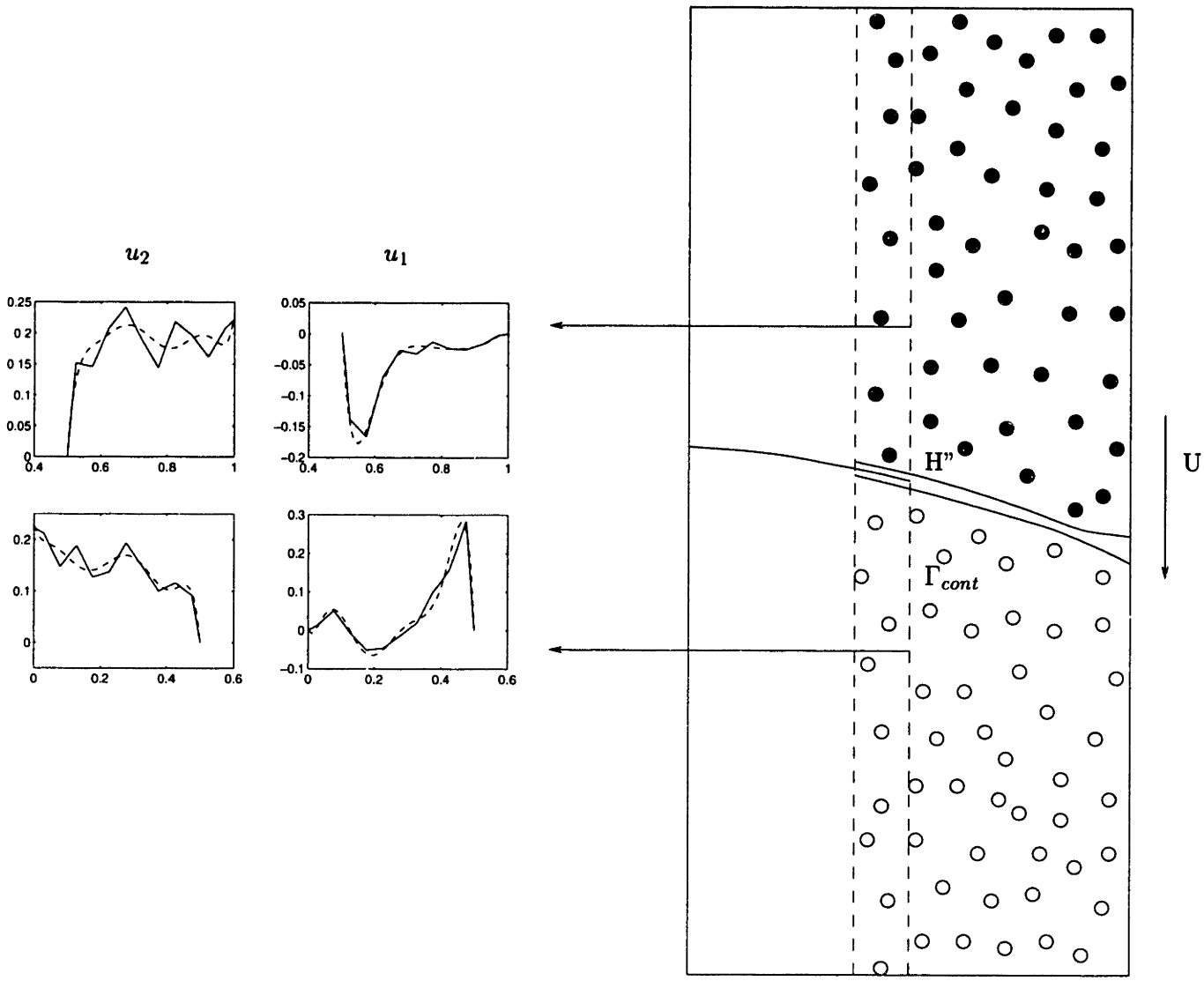

Figure 8-4: Second part of one Schwarz iteration: molecular data on Γ_{cont} is used as boundary condition data on the continuum simulation. The solid line represents the actual data, and the dashed line the fit used to impose the data. Angle information at point H" is also used.

corrected for mass continuity. The "residual" mass flow rate for fluid B

$$\int_{U''H''} u_{cont}^{U''H''}\, dl - \int_{BU''} u_{bc}\, dl, \tag{8.1}$$

and fluid A

$$\int_{L''H''} u_{cont}^{L''H''}\, dl - \int_{AL''} u_{bc}\, dl, \tag{8.2}$$

were accounted for by reducing the flux from Γ_{cont} by the appropriate amount

$$u_{cont}^{U''H''} = u_{cont}^{U''H''} - \frac{\int_{U''H''} u_{cont}^{U''H''}\, dl - \int_{BU''} u_{bc}\, dl}{\int_{BU''} dl} \tag{8.3}$$

for fluid B, and

$$u_{cont}^{L''H''} = u_{cont}^{L''H''} - \frac{\int_{L''H''} u_{cont}^{L''H''}\, dl - \int_{AL''} u_{bc}\, dl}{\int_{AL''} dl} \tag{8.4}$$

for fluid A. Here u_{cont} denotes the normal boundary data from the molecular dynamics simulation on the portion of Γ_{cont} indicated, and u_{bc} denotes the normal boundary data on Γ_{BC} and Γ_{AD}. This projection of the normal boundary data of the continuum calculation onto an incompressible space is essential. The continuum simulation iterative technique of chapter 6 diverges in an oscillatory manner if the boundary data to which it is subjected do not honor mass conservation.

8.1.2 Continuum Calculation

The foundations for the continuum calculation have been laid in chapter 6. The theory and the numerical techniques remain the same but the geometry is slightly changed: the continuum domain is physically less wide but most importantly does not encompass the solid wall. For reference purposes we include Fig. 8-5 from chapter 6 which demonstrates the following important note: Γ_{cont} no longer corresponds to the wall but is now the artificial boundary on which the continuum simulation terminates. There is a net mass flux of both fluids through Γ_{cont} and into the molecular region (note that symmetry considerations mean that the combined net mass flux of fluid

A and fluid B through the whole of Γ_{cont} is actually zero). These normal boundary conditions, as well as the tangential boundary conditions on Γ_{cont}, are of the Dirichlet type. This was actually the objective of the Schwarz method: the matching of fluxes through the use of Dirichlet boundary conditions.

Dirichlet boundary conditions have been examined in chapter 6. It was concluded that the iterative technique developed in chapter 6 is compatible with both Dirichlet and Neumann boundary conditions on the slipping wall. Although the normal fluid velocity on Γ_{CD} was always taken to be zero in chapter 6, this was still imposed through Dirichlet boundary conditions and therefore, there is no fundamental change in the formulation of the continuum problem. Note that the coordinate systems of chapter 6 and chapter 7 have been retained in the continuum and molecular subdomains respectively for reference reasons. Hence the two coordinate systems (Fig. 6-1 and Fig. 7-2 for example) are related by the following transformation $x_1 \Leftrightarrow -z$ and $x_2 \Leftrightarrow x$.

8.1.3 Molecular Calculation

The molecular simulations are conducted as described in chapter 7. For reasons of computational simplicity the same system (Fig. 7-2) was used despite the fact that the centerline region of the channel is not included in the hybrid description of the contact line problem. As we discuss in the previous section this region acts as a particle reservoir that is responsible for the correct feed of molecules to the boundary condition imposition faces Γ_{mol}, Γ_{BC}, and Γ_{AD}. Figure 8-6 shows the molecular system and the artificial boundary Γ_{mol} and the portions of Γ_{AD} and Γ_{BC}, L'D and U'C respectively, that impose the boundary data from the continuum iterate. Although the problem is symmetric about the channel centerline, treating only half of the channel requires the imposition of no mass-flux normal and zero-shear-stress tangential boundary conditions which has not been done in molecular dynamics to date. The treatment of the complete channel does not increase the computational cost of the solution because the extra cost is exactly balanced by the double number of statistical samples acquired. This, however, is only true if the molecular dynamics algorithm

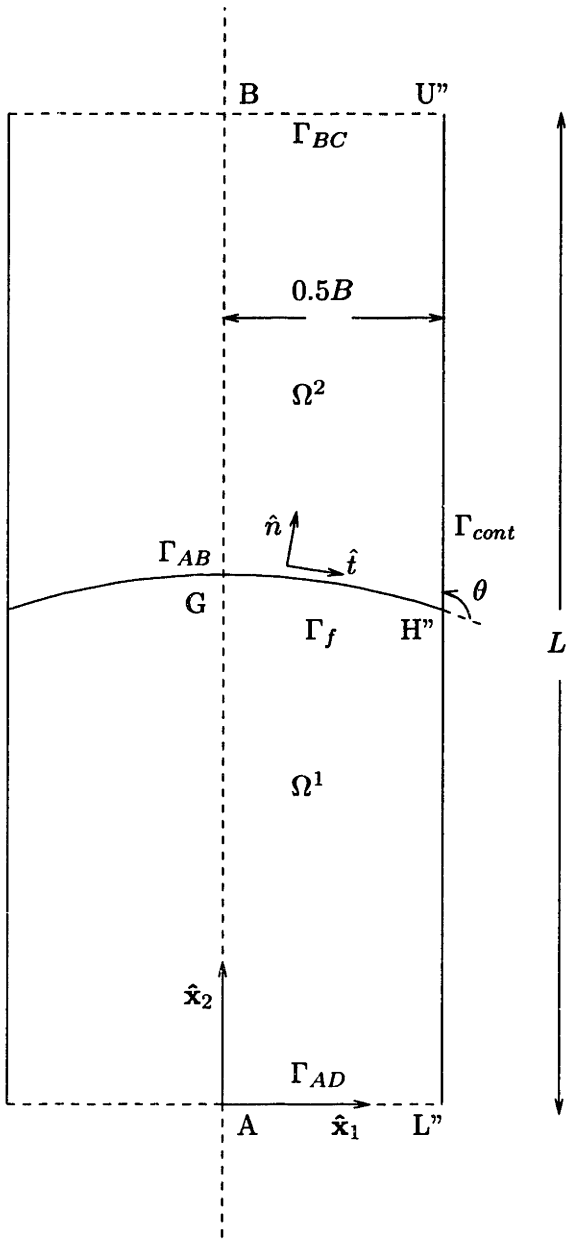

Figure 8-5: Problem geometry. The continuum simulation is terminated on Γ_{cont}.

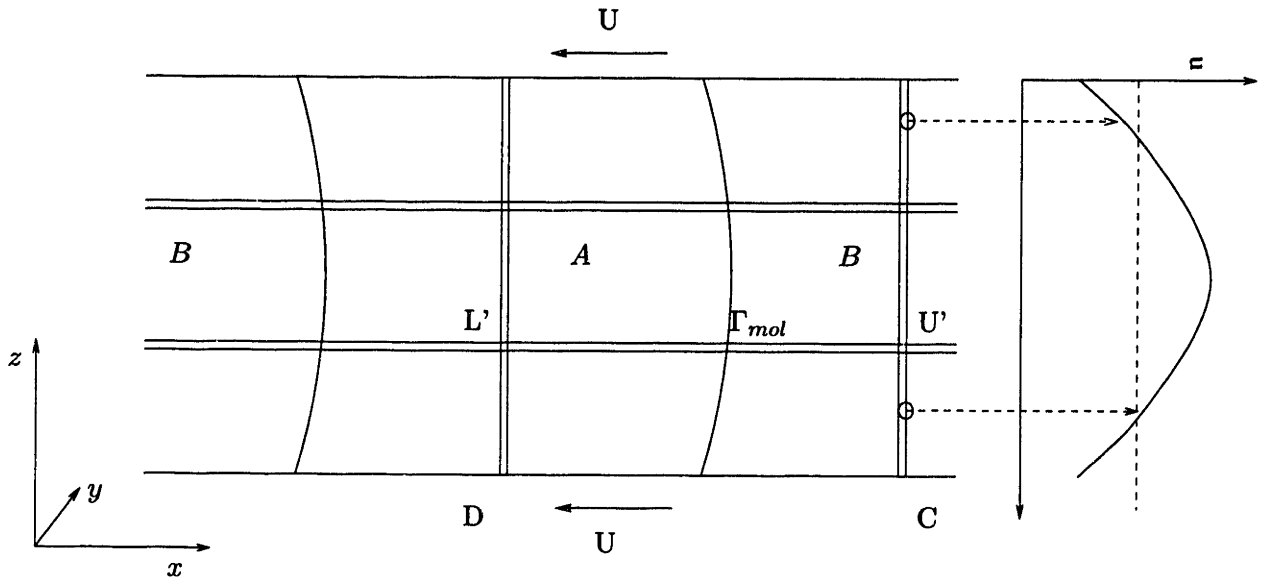

Figure 8-6: Boundary condition imposition reservoirs for the hybrid problem. The center region of the channel acts as the particle reservoir that ensures mass conservation. Symmetry considerations render either side of the channel with respect to the centerline sufficient; both sides were kept for reasons of computational convenience.

used is a true $O(N)$ algorithm, that is the cost scales linearly with the number of molecules N.

8.2 Results

In this section we present the results of the hybrid formulation and solution of the contact line problem of chapters 6 and 7 for a capillary number of $Ca = 0.059$. In this problem we have chosen the fully continuum solution for $Ca = 0.059$ presented in chapter 7 (Fig. 7-8) as the initial guess solution. This choice significantly reduces the computational effort required since the starting solution is close to the exact (fully molecular) solution and therefore, a few iterations will suffice until complete convergence is obtained. The issue of convergence of the modified Schwarz technique from initial guess solutions arbitrarily far from the exact solution is left as the subject of future work.

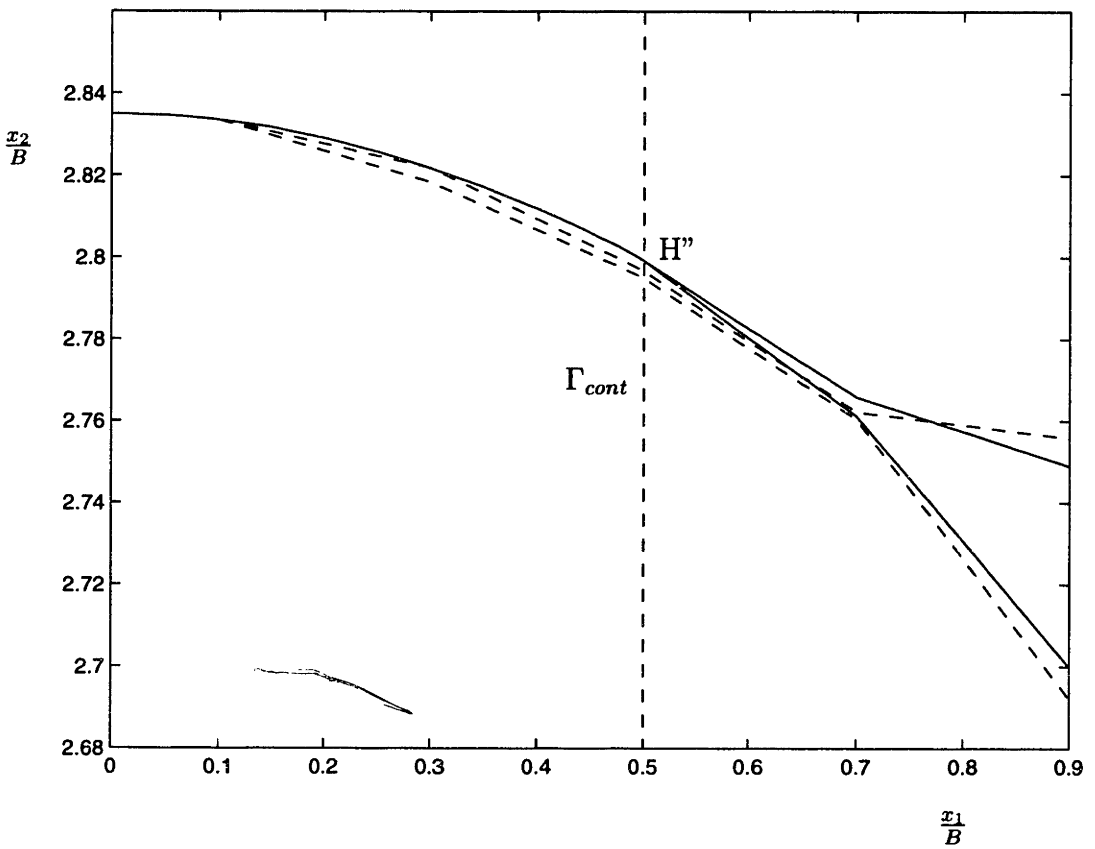

Figure 8-7: Comparison of the fully molecular (dashed) and hybrid (solid) interface shape. The continuum segment of the hybrid solution joins the molecular at H" where the gap between the receding and advancing parts was taken to be equal to zero.

Following the Schwarz procedure, the fully continuum solution from chapter 7 on Γ_{mol} is used as boundary condition on a molecular simulation, that in turn provides a set of boundary conditions (velocity on Γ_{cont} and angle on H") for the continuum solver. The continuum solution completes one iteration cycle. A second iteration gives the results of Fig. 8-7, Fig. 8-8. We can see that the results are in very good agreement with the corresponding fully molecular ones. Note that the hybrid interface shape consists of a single line in the continuum subdomain up to point H"and two lines–the advancing and receding parts (following the definition of chapter 7)–in the molecular domain. The gap between the advancing and receding parts is correct to scale in Fig. 8-8. Although the interface shape has changed from the fully continuum first guess configuration, this approximation is again well within the expected statistical error. We thus conclude that the hybrid technique we have developed can capture the dynamics of complex multi-fluid fluid mechanical phenomena.

Further simulations are required to establish the (expected) unconditional convergence of the iteration from arbitrary initial interface shapes. Our results indicate that the modified Schwarz method for two fluids converges from initial conditions close to the final result. Extension to macroscopic systems is also the subject of future work. As remarked in chapter 5 the size of the largest system simulated is limited by noise considerations which, however, do not present major obstacles in the case of the motion of contact lines.

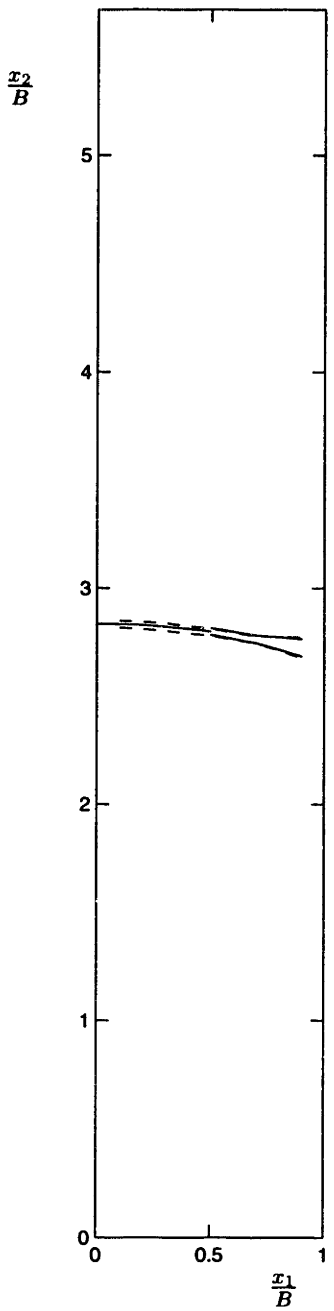

Figure 8-8: Comparison of the fully molecular (dashed) and hybrid (solid) interface shape to correct scale.

Chapter 9

Summary-Future Work

We have developed a new hybrid numerical simulation technique which successfully combines continuum and molecular descriptions in a single solution framework. Hybrid techniques are becoming increasingly important nowadays; the need for modeling on scales approaching the molecular scale or understanding highly non-equilibrium situations is driven by today's increasingly complex needs for materials processing. This thesis represents the first attempt to a completely general hybrid solution framework that involves multidimensional flow (including dense fluids) that has a non-zero component in the direction normal to the interface between the continuum and molecular subdomains. The matching between the subdomains is provided through the Schwarz alternating method, a domain decomposition technique.

The matching technique has been validated with the following test problem: flow in a two-dimensional obstructed channel. The results are in good agreement with the fully continuum solution, which for the purposes of this test was taken to be exact. There is, however, some additional error (in addition to the statistical error expected due to the molecular dynamics subdomain contribution) that is believed to originate in the dynamics of the Schwarz alternating procedure. Although the Schwarz method is fairly well known and analyzed for the case of continuum subdomains, its response to one or more molecular subdomains has not been investigated elsewhere, and therefore further work is required.

Statistical noise has a detrimental effect on the simulation capabilities of molecular

dynamics. In fact, statistical noise sets the limit on the size of the largest calculation than can be treated by either a fully molecular or a hybrid technique as discussed in chapter 5. Future work must concentrate in addressing the statistical noise problem and the more general issue of expanding the range of scales that can be treated by MD, and in effect, by hybrid techniques.

Problems such as the moving contact line are very well suited to treatment by hybrid techniques because they have large gradients that are localized to regions of size comparable to a few molecular diameters. On the contrary, systems that require molecular modeling on significantly larger regions cannot be treated by the method developed here; although the coupling technique is quite general, the molecular dynamics simulation will be prohibitively expensive. More efficient molecular simulation methods are thus needed to address this problem. Alternatively, numerical efficiency can be gained at the expense of a more coarse grained molecular description to the extent that the physics of interest allow.

The moving contact line represents a classical example of a phenomenon that requires modeling on the microscale. Our ultimate objective was to successfully capture the dynamics of a moving contact line through a hybrid technique. This was achieved in three steps.

A fully continuum finite element simulation technique has been developed that serves as the continuum subdomain of the hybrid calculation. None of the existing techniques satisfies the requirement of variational consistency; we have successfully implemented a variationally consistent simulation scheme that also benefits from great numerical efficiency.

We have been able to utilize the results from our molecular dynamics simulations of contact line motion to extract appropriate *continuum* boundary conditions. This molecular *then* continuum hybrid technique can prove to be very useful because the resulting fairly accurate fully continuum simulations are very inexpensive. We have additionally shown that the essential molecular information in contact line problems is localized to the vicinity of the contact point.

The development of the matching algorithm for two-fluid problems was the final

step in the development of the hybrid algorithm for the contact line problem. The hybrid solution has been compared to the fully molecular solutions which were taken as exact. The agreement between the two solutions is good. Future work is required for the investigation of the proposed Schwarz method for two-fluid flows: our results demonstrate convergence from initial conditions close to the final solution; arbitrary initial interface configurations have not been tested to date. Application of the algorithm to macroscopic problems is straightforward; hybrid solutions of macroscopic problems are now possible within the limitations imposed by noise considerations discussed in chapter 5.

Our ultimate objective is to enhance our simulation capabilities beyond the well established continuum approaches. This work represents a major step forward in this direction. The connection between molecular dynamics simulations and the macroscopic world, however, is far from complete. The simulation of realistic problems relies on the existence of interaction potentials that can adequately model various materials of interest. Although major developments have been made in this direction for materials such as water, copper, silicon, light hydrocarbons, and noble gases, in some cases the resulting potentials require computationally inefficient simulation algorithms and hence further work is required. Additionally, although our modeling capabilities of homogeneous systems are fairly advanced, the characterization of interactions between materials, which is of paramount importance in any practical situation, is poorly understood and also requires further work.

Bibliography

[1] Gas encyclopaedia, 1976.

[2] R. A. Adams. *Sobolev Spaces.* Academic Press, New York, 1975.

[3] F. A. Alexander, A. L. Garcia, and B. J. Alder. The consistent Boltzmann algorithm for the van der Waals equation of state. *Physica A*, 240:196–201, 1997.

[4] M. P. Allen and D. J. Tildesley. *Computer Simulation of Liquids.* Oxford University Press, 1987.

[5] I. B. Bazhlekov and A. K. Chesters. Numerical investigation of the dynamic influence of the contact line region on the macroscopic meniscus shape. *J. Fluid Mech.*, 329:137–146, 1996.

[6] T. D. Blake. Dynamic contact angles and wetting kinetics. In P. Schwitzer and S. Kistler, editors, *Liquid Film Coating: Scientific Principles and their Technological Implications.* 1994.

[7] J. F. Bourgat, P. Le Tallec, D. Tidriri, and Y. Qiu. Numerical coupling of nonconservative or kinetic models with the conservative compressible Navier-Stokes equations. In R. Glowinski, G. Meurant, B. Voigt, and O. Widlund, editors, *Fifth International Symposium on Domain Decomposition Methods for Partial Differential Equations*, pages 420–440. SIAM, 1991.

[8] R. G. Cox. The dynamics of the spreading of liquids on a solid surface. Part 1. Viscous flow. *J. Fluid Mech.*, 168:169–194, 1986.

[9] E. B. Dussan. On the spreading of liquids on solid surfaces: Static and dynamic contact angles. *Ann. Rev. Fluid Mech.*, 11:371–400, 1979.

[10] D. J. Evans and G. P. Morriss. *Statistical Mechanics of Nonequilibrium Liquids.* Academic Press, 1990.

[11] U. Frisch, B. Hasslacher, and Y. Pomeau. *Phys. Rev. Lett.*, 56:1505, 1986.

[12] P. Glansdorff and I. Prigogine. *Thermodynamic Theory of Structure, Stability and Fluctuations.* Wiley-Interscience, New York, 1971.

[13] F. Golse. Applications of the Boltzmann equation within the context of upper atmosphere vehicle aerodynamics. *Computer Methods in Applied Mechanics and Engineering*, 75:299–316, 1989.

[14] Y. Guissani and B. Guillot. A computer simulation study of the liquid-vapor coexistence curve of water. *J. Chem. Phys.*, 98:8221–8235, 1993.

[15] N. Hadjiconstantinou and A. T. Patera. Heterogeneous atomistic-continuum representations for dense fluid systems. *International Journal of Modern Physics C*, 8:967–976, 1997.

[16] D. B. Hash and H. A. Hassan. A hybrid DSMC / Navier-Stokes solver. *AIAA Paper 95-0410*, 1995.

[17] J. O. Hirschfelder, C. F. Curtis, and B. B. Bird. *Molecular Theory of Gases and Liquids.* Wiley, 1954.

[18] L. W. Ho and A. T. Patera. Variational formulation of three-dimensional viscous free-surface flows: Natural imposition of surface tension boundary conditions. *Int. J. Numer. Methods Eng.*, 13:691–698, 1991.

[19] L. W. Ho and E. M. Ronquist. Spectral element solution of steady incompressible viscous free-surface flows. *Finite Elements in Analysis and Design*, 16:207–227, 1994.

[20] R. L. Hoffman. A study of the advancing interface. *J. Colloid and Interface Sci.*, 50:228–241, 1975.

[21] W. G. Hoover, A. J. De Groot, and C. G. Hoover. Massively parallel computer simulation of plane-strain elastic-plastic flow via nonequilibrium molecular dynamics and Lagrangian continuum mechanics. *Computers in Physics*, 6:155–167, 1992.

[22] J. Ibsen, R. Soto, and P. Cordero. Free thermal convection driven by nonlocal effects. *Phys. Rev. E*, 52:4533–4536, 1995.

[23] J. H. Irving and J. G Kirkwood. The statistical mechanical theory of transport processes. IV. The equations of hydrodynamics. *J. Chem. Phys.*, 17:817–829, 1950.

[24] N. Kikuchi. *Finite Element Methods in Mechanics.* Cambridge University Press, Cambridge, 1986.

[25] S. Kohlhoff, P. Gumbsch, and H. F. Fischmeister. Crack propagation in b.c.c. crystals studied with a combined finite-element and atomistic model. *Philosophical Magazine A*, 64:851–878, 1991.

[26] J. Koplik and J. R. Banavar. Continuum deductions from molecular hydrodynamics. *Ann. Rev. Fluid Mech.*, 27:257–292, 1995.

[27] J. Koplik, J. R. Banavar, and J. F. Willemsen. Molecular dynamics of fluid flow at solid surfaces. *Phys. Fluids A*, 1:781–794, 1989.

[28] P. L. Lions. On the Schwarz alternating method. I. In R. Glowinski, G. Golub, G. Meurant, and J. Periaux, editors, *First International Symposium on Domain Decomposition Methods for Partial Differential Equations*, pages 1–42, Philadelphia, 1988. SIAM.

[29] J. Lowndes. The numerical simulation of the steady movement of a fluid meniscus in a capillary tube. *J. Fluid Mech.*, 101:631–646, 1980.

[30] H. Mavridis, A. N. Hrymak, and J. Vlachopoulos. Finite element simulation of stratified multiphase flows. *AIChE Journal*, 33:410–422, 1987.

[31] S. T. O'Connell and P. A. Thompson. Molecular dynamics-continuum hybrid computations: A tool for studying complex fluid flows. *Phys. Rev. E*, 52:R5792–R5795, 1995.

[32] M. Parinello and A. Rahman. Polymorphic transitions in single crystals: A new molecular dynamics method. *Journal of Applied Physics*, 52:7182–7190, 1981.

[33] A. T. Patera and E. M. Ronquist. *Introduction to Finite Element Methods. Application to Incompressible Fluid Flow and Heat Transfer.* In preparation.

[34] A. Quarteroni and A. Valli. *Numerical Approximation of Partial Differential Equations.* Springer-Verlag, 1994.

[35] K. Refson. Molecular dynamics simulation of n-butane. *Physica*, 131:256–266, 1985.

[36] K. J. Ruschak. A method for incorporating free boundaries with surface tension in finite element fluid-flow simulation. *Int. J. Numer. Methods Fluids*, 15:639–648, 1980.

[37] P. Sheng and M. Zhou. Immiscible-fluid dipslacement: Contact-line dynamics and the velocity-dependent capillary pressure. *Phys. Rev. A*, 45:5694–5708, 1992.

[38] A. A. Sonin. A synthesis of the kinetic and hydrodynamic theories of the dynamic contact angle. Department of Mechanical Engineering, M.I.T.

[39] A. Tenenbaum, G. Ciccotti, and R. Gallico. Stationary nonequilibrium states by Molecular Dynamics. Fourier's law. *Phys. Rev. A*, 25:2778–2787, 1982.

[40] P. A. Thompson, W. B. Brinckerhoff, and M. O. Robbins. Microscopic studies of static and dynamic contact angles. *J. Adhesion Sci. Technol.*, 7:535–554, 1993.

[41] P. A. Thompson and M. O. Robbins. Simulations of contact-line motion: Slip and the dynamic contact angle. *Phys. Rev. Lett.*, 63:766–769, 1989.

[42] C. Trozzi and G. Ciccotti. Stationary nonequilibrium states by molecular dynamics. II Newton's law. *Phys. Rev. A*, 29:916–925, 1984.

[43] O. V. Voinov. Hydrodynamics of wetting. *Izvestiya Akademii Nauk SSSR, Mekhanika Zhidkosti i Gaza*, 5:76–84, 1976.

[44] D. C. Wadsworth and D. A. Erwin. One-dimensional hybrid continuum / particle simulation approach for rarefied hypersonic flows. *AIAA Paper 90-1690*, 1990.

THESIS PROCESSING SLIP

FIXED FIELD: ill. _____ name _____

index _____ biblio _____

▶ COPIES: Archives Aero Dewey Eng Hum

Lindgren Music Rotch Science

TITLE VARIES: ▶ ☐ _____

NAME VARIES: ▶ ☑ George.

IMPRINT: (COPYRIGHT) _____

▶ COLLATION: 153 l

▶ ADD: DEGREE: _____ ▶ DEPT.: _____

SUPERVISORS: _____

NOTES:

cat'r: date: 5

page: 38 ~~1/0/0~~

▶ DEPT: M.E. Ph. D.

▶ YEAR: 1998 ▶ DEGREE: _____

▶ NAME: HADJICONSTANTINOU, Nicolas